

Studies on Bismuth-based Light Absorbers for Lead-free Perovskite Solar Cells

非鉛ペロブスカイト太陽電池における
ビスマス系光吸収材料に関する研究

Graduate School of Life Science
and System Engineering
Kyushu Institute of Technology

Dissertation for the Degree of Doctor of Philosophy

Author: ZHANG CHU

Supervisor: Professor Tingli Ma

Feb. 2019

Abstract

Lead-free bismuth perovskites have been considered as a promising substitute for the lead halide perovskites aiming at solving the instability and toxicity issues. However, lead-free perovskites still suffer from low efficiency problems due to their large bandgap and poor-quality film. In order to achieve high power conversion efficiency while maintaining the advantages of stability and non-toxicity, it is crucial to develop new lead-free perovskite materials. In this thesis, two kinds of new lead-free perovskites with small bandgap and excellent stability were synthesized via simple procedures. With various characteristic methods, the composition of these new perovskites was determined, and their optoelectronic properties were analyzed. Moreover, these materials were applied to the perovskite solar cells, and their performances as the light absorbers were evaluated. Based on these results, the potential routes for improving the performances of the lead perovskite photovoltaic devices were developed.

In chapter 1, the background of the photovoltaic technology and the current development of the lead-free perovskites were introduced. Furthermore, the recent challenges for the lead-free perovskites and the purpose of this thesis were described.

In chapter 2, the reagents and apparatus employed in this thesis were listed. Furthermore, general descriptions of the preparation methods and the device fabrication techniques were displayed. In addition, the basic principles of the physical and optoelectronic characterization methods were introduced.

In chapter 3, a mixed chalcogenide-halide lead-free perovskite MABiI_2S was successfully synthesized through a simple two-step solid-state process. With multiple testing methods, the composition of the MABiI_2S perovskite was confirmed. By measuring the UV-Vis absorption spectra, it is determined that the MABiI_2S perovskite has a bandgap of 1.52 eV, and it possesses a wide absorption range. The unique properties of the MABiI_2S perovskite meet the criteria of the light absorber for the perovskite solar cells. Furthermore, by employing an in-situ growth process, the difficulty that the spin coating technique cannot produce viable MABiI_2S films on the TiO_2 substrates was solved. The composition of the in-situ growth film was verified with layer-by-layer XRD pattern analysis. Photovoltaic devices were fabricated with the MABiI_2S perovskite, and the

device performances were evaluated. Although the PCE of the MABiI_2S solar cell was low, the factors that hindered the device performance were proposed and possible enhancement methods were performed.

In chapter 4, a novel high stability double perovskite $\text{Cs}_2\text{NaBiI}_6$ was successfully synthesized through a simple hydrothermal process. The bandgap of the $\text{Cs}_2\text{NaBiI}_6$ was determined to be 1.66 eV, and a wide absorption range of the $\text{Cs}_2\text{NaBiI}_6$ up to 650 nm was revealed. The $\text{Cs}_2\text{NaBiI}_6$ displayed outstanding stability showing negligible decomposition after a 5-month storage under >70% humidity. Perovskite solar cells fabricated with $\text{Cs}_2\text{NaBiI}_6$ exhibited comparable PCE to other bismuth perovskite solar cells. The devices stayed in ambient condition displayed a very small decrease in the photovoltaic performances, suggesting good device stability. The PCE distribution of the cells is narrow, suggesting that the devices displayed good reproducibility. Although the average PCE of the $\text{Cs}_2\text{NaBiI}_6$ solar cells so far is not high due to a low J_{SC} , we have revealed the main reason of the low J_{SC} , and suggested possible enhancement directions.

In chapter 5, 3D shuttle-like $\text{Cs}_2\text{NaBiI}_6$ micro single crystals were prepared by a simple one-step hydrothermal growth method. By observing the growth process, the growth mechanism of the micro single crystals were elucidated, and it was confirmed that the $\text{Cs}_2\text{NaBiI}_6$ prepared with the optimized conditions consists high ratio of well-defined shuttle-like micro single crystals. Moreover, by investigating multiple reaction parameters including hydroiodic acid concentration, Na cation ratio and hydrothermal synthesizing temperature, the optimized preparation condition of the micro single crystal growth was explored.

Finally, general conclusions of this thesis were summarized and future prospects were proposed. The development of lead-free perovskites and lead-free perovskites photovoltaic devices still face big challenges. The further studies include the development of new lead-free perovskites with high performance, enhancement of the film fabricating technique of the lead-free perovskite solar cell devices, and the exploration towards the single crystal lead-free perovskite photovoltaic devices.

Contents

Chapter 1. Introduction.....	1
1.1 History of the photovoltaic technology	1
1.2.1 Crystal structure and properties of the halide perovskites.	7
1.2.2 Perovskite solar cell architectures and fabrication techniques.....	8
1.3 Lead-free perovskites for solar cells.....	10
1.3.1 Issues of the lead halide perovskites.	10
1.3.2 Non-toxic elements to substitute lead in the perovskites	11
1.4 Lead-free double perovskites.....	13
1.4.1 Structure and properties of the double perovskites	13
1.4.2 Development of the lead-free halide double perovskites.	14
1.5 Single crystals	15
1.5.1 Single crystals and perovskite solar cells.....	16
1.5.2 Development of the perovskite single crystals.....	16
1.6 Challenges and Research topics.....	17
References.....	18
Chapter 2. Experimental section of the general methods and characterization techniques.....	26
2.1 Raw materials and apparatus	26
2.1.1 Raw materials.....	26
2.1.3 General methods of the hydrothermal synthesis method.	29
2.1.4 The preparation of the compact TiO ₂ layer and the mesoporous TiO ₂ layer precursor	30
2.2 Characterization methods	31
2.2.1 X-ray diffraction crystallography (XRD).....	31
2.2.2 Field emission scanning electron microscopy (FE-SEM).....	32

2.2.3 X-ray photoelectron spectroscopy (XPS).....	32
2.2.4 Ultraviolet photoelectron spectroscopy (UPS).....	33
2.2.5 Energy-dispersive X-ray spectroscopy (EDX).....	34
2.2.6 Ultraviolet-visible spectroscopy (UV-Vis)	35
2.2.7 Photovoltaic performance measurement	36
References.....	37
Chapter 3. Development of a Mixed Halide-chalcogenide Bismuth-based Perovskite MABiI ₂ S with Small Bandgap and Wide Absorption Range	38
3.1 Introduction.....	38
3.2 Experimental section.....	39
3.2.1 Synthesis of the MBIS perovskite powder sample	39
3.2.2 Physical and optical characterization of the as-prepared MBIS perovskite.....	40
3.2.3 Solar cell device fabrication and testing	41
3.3 Results and discussion	43
3.3.1 Tolerance factor assessment.....	43
3.3.2 SEM images of the as-prepared MBIS sample.	43
3.3.3 XRD analysis of the as-prepared sample	44
3.3.4 EDX profile and the elemental mapping.....	45
3.3.5 XPS analysis.....	47
3.3.6 UV-vis absorption spectrum and the Tauc' plot	47
3.3.7 Device fabrication and characterization.....	48
3.4 Conclusions.....	53
References.....	55
Chapter 4. Design of a Novel and Highly Stable Lead-Free Double Perovskite Cs ₂ NaBiI ₆ for Photovoltaic Application	58
4.1 Introduction.....	58

4.2 Experimental section.....	60
4.2.1 Synthesis of the target compound	60
4.2.2 Characterization of the CNBI.....	61
4.2.3 Fabrication and testing of the devices	61
4.3 Results and discussion	62
4.3.1 Tolerance factor calculation	62
4.3.2 XRD analysis	64
4.3.3 SEM images of the CNBI and the chemical process	65
4.3.4 XPS spectra analysis	66
4.3.5 UV-vis absorption spectra analysis and the optical bandgap calculation.	69
4.3.6 Stability assessment of the CNBI powder sample.	69
4.3.7 Device fabrication and characterization.....	71
4.3 Conclusions.....	75
References.....	76
Chapter 5. Preparation and optimization of the micro single crystals of the Cs ₂ NaBiI ₆ (CNBI) double perovskite	78
5.1 Introduction.....	78
5.2 Experimental section.....	79
5.2.1 Crystal growth process of the micro single crystals.....	79
5.2.2 Characterization methods	80
5.3 Results and discussion	80
5.3.1 The optimization of the CNBI micro single crystal growth method.....	80
5.3.2 The growth mechanism of the CNBI micro single crystals	85
5.4 Conclusions.....	87
References.....	88

6. General conclusions and future prospects	90
Achievements	92
Acknowledgements	94

Chapter 1. Introduction

1.1 History of the photovoltaic technology

The term photovoltaic refers to any device and system that can convert energy from light to electricity. Although discovered by A. E. Becquerel in 1839 [1], the photovoltaic effect was not successfully utilized until silicon solar cells were invented based on the P-N junction in the Bell Lab in 1954 [2]. The photovoltaic modules capable of producing energy at the magnitude of MW were developed in 1956, and the photovoltaic technology has been widely employed to generate clean energy that make less impact to the natural environment ever since. As of the year 2016, based on the fossil fuel consumption and the carbon dioxide emission, it is calculated that 2.5×10^4 GW of low carbon emission energy will be demanded by the year 2050 to counteract the global climate degradation [2]. To meet such urgent demand, the photovoltaics have experienced fast growth. For example, expected accumulative photovoltaic capacity planned by the International Energy Agency (IEA) as of the year 2020 was rapidly outstripped in the year 2014 [3-6]. It is worth noting that although by definition photovoltaics would enclose any means that convert energy from light to electricity; it is only meaningful when discussing converting solar energy rather than other light sources, since the solar energy is the most significant green and free energy source.

It is a stereotype for people to consider that photovoltaic devices are of high cost compared to traditional energy sources. While indeed the renewable energy sources all suffer from higher cost in a long time, photovoltaic technology recently has gain a great success to eventually become a net energy producer [7]. With the advance in technologies, the reduction of the payback time and the manufacturing cost has ensured the photovoltaics to be the most promising renewable energy in the future [8]. The developing trend of the photovoltaics highlighted the viability that the photovoltaic technology will take up a significant fraction of the global energy supply in the future, providing a unique contribution to the world's environmental sustainability and energy security challenge [9-10].

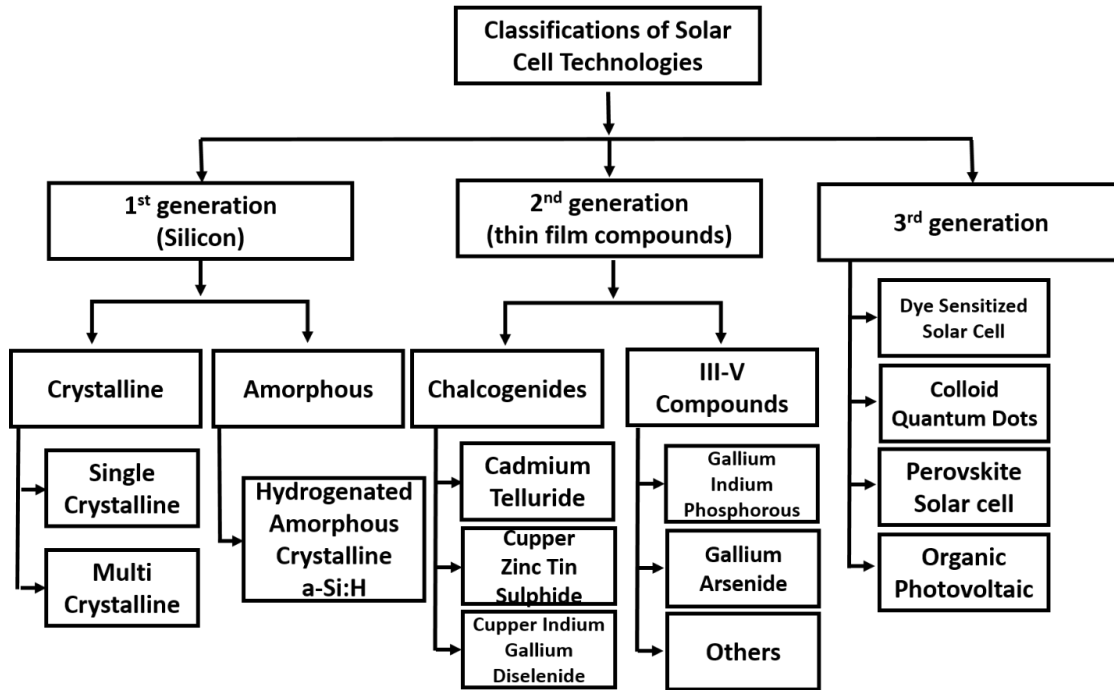


Fig.1 Classification of solar cell technologies by generations.

In the recent decades, photovoltaic technology has experienced a booming growth. Fig.1 illustrated that depending on the materials and manufacturing techniques, photovoltaic devices can be categorized into three generations. Their certified photovoltaic performances under the global AM1.5 spectrum (1000 W/m^2) at 25°C are summarized in Table 1.

The 1st generation photovoltaic devices are silicon solar cells, including polycrystalline silicon solar cells and monocrystalline silicon solar cells. Until today, the first generation photovoltaic cells have shown high power conversion efficiency up to 25% [11]. Mature fabrication and encapsulation techniques ensured the high stability of the 1st generation photovoltaic devices, and the silicon solar cell modules have long been applied to the real life scenarios. However, there are several major drawbacks of the first generation solar cells.

Typically, to fabricate a high quality silicon solar cell module, strict operation conditions are required including steady-state silicon single crystal growth environment, dust-free operating chamber, involvement of expensive automatic processing devices, high temperature and pressure,

etc. In addition, silicon is an indirect bandgap semiconductor with a low absorption coefficient of 10^4 cm^{-1} magnitude [12]. As a result, the theoretical thickness of the silicon films should be higher than $100 \text{ }\mu\text{m}$ for an effective absorption in silicon solar cells [13]. In combination with the high price of the high-purity silicon raw material, the silicon solar modules was always at a high price. Although the price has been reduced dramatically with the efforts of many research entities across the world [14-16], the cost is still an important factor that hinders the massive development of the silicon solar cells. As of the amorphous silicon solar cells, this type of silicon solar cell has significantly lower cost than the polycrystalline or monocrystalline silicon solar cells. Yet their power conversion efficiency is limited by the optoelectronic maximum. It is estimated that both the cost-per-watt value and the expected lifetime are poorer than that of other silicon solar cells [17], thus their performances are not comparable to the 1st generation silicon solar cells.

The 2nd generation photovoltaics usually refer to the thin film semiconductor solar cells. One significant difference between the 1st and 2nd generation solar cells is that the semiconductor materials of the 2nd generation solar cells generally show direct bandgaps, which would allow a much thinner film to realize higher light absorption rate [18]. Common 2nd generation photovoltaics include copper indium gallium selenide (CIGS) solar cells, copper zinc tin sulfide (CZTS) solar cells, gallium arsenide (GaAs) solar cells, etc. The GaAs solar cells have the best performance, achieving PCEs of 29% and 40% in single and tandem devices, respectively [19]. This is comparable to the silicon solar cells. However, the resources of raw materials, gallium, is not abundant, especially when considering large-scale industrial production and deposition. To make things worse, arsenide compound is toxic. The toxicity further constrained the application of the GaAs solar cells. The CIGS solar cells can reach 20% PCE [19]. However, they require more rare earth elements, thus have even higher cost. As the substitute, the CZTS solar cells assessed the issue of the expensive raw material, and the PCE is quickly catching up with the CIGS [20].

The 3rd generation solar cells include organic photovoltaics, dye-sensitized solar cells (DSSC), quantum dot solar cells (QD), and perovskite solar cells (PSC). The DSSC entered the scene in 1991 [21]. This is a low cost photovoltaic device family, which typically employ cheap raw materials and are easy to fabricate. One huge advantage is that the DSSC can employ roll-printing technique, which is significantly easier than other fabrication techniques. The DSSC can also be flexible and/or transparent, thus has potential for specified situations. However, the PCE

of these solar cells are usually low due to the narrow absorption region of the dyes, as well as their lower stability [22]. Although the DSSC has experienced some progresses, pushing its PCE over 10% [23-24], the device performances were still not fulfilling, and the stability of such devices still heavily rely on encapsulation.

The polymer solar cells can be of very low cost due to cheap materials. Employing special bulk heterojunction structure, the fabrication process of the organic photovoltaics is relatively simple [25]. It is also promising when consider flexible devices. However, their PCE are still quite low per today.

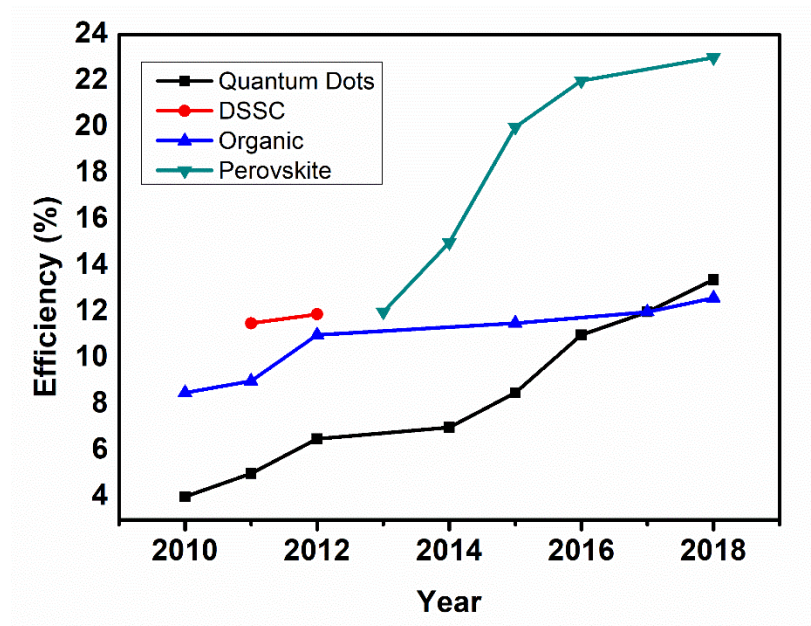


Fig.2 PCE development trends of the 3rd generation photovoltaics [26].

Among all the 3rd generation photovoltaics, the perovskite solar cell rose sharply. As shown in Fig.2, it achieved the highest PCE of all the 3rd generation photovoltaics in a mere eight years. The perovskite solar cells are easy to fabricate as well as employing cheap materials. Considering their great potential, the perovskite solar cells have been expected to bring great breakthrough for the next generation solar cells. We will discuss some general concepts about the perovskite solar cells in next part.

Table.1 Confirmed PCE of the terrestrial cells and submodules(Measured under the AM1.5 spectrum (1000 W/m²) at 25 °C [19])

Classification	efficiency (%)	area (cm²)	Voc (V)	Jsc (mA/cm²)	fill factor (%)
Silicon solar cells					
Crystalline devices	26.7 ± 0.5	79.0	0.738	42.65	84.9
Multicrystalline devices	22.3 ± 0.4	3.923	0.6742	41.08	80.5
Thin transfer submodules	21.2 ± 0.4	239.7	0.687	38.50	80.3
Thin film minimodules	10.5 ± 0.3	94.0	0.492	29.7	72.1
III-V cells					
GaAs thin film devices	28.8 ± 0.9	0.9927	1.122	29.68	86.5
GaAs multicrystalline devices	18.4 ± 0.5	4.011	0.994	23.2	79.7
InP crystalline devices	24.2 ± 0.5	1.008	0.939	31.15	82.6
Thin film chalcogenide cells					
CIGS	22.9 ± 0.5	1.041	0.744	38.77	79.5
CdTe	21.0 ± 0.4	1.0623	0.8759	30.25	79.4
CZTS	10.0 ± 0.2	1.113	0.7083	21.77	65.1
Amorphous/microcrystalline Si solar cells					
Amorphous Si	10.2 ± 0.3	1.001	0.896	16.36	69.8

Microcrystalline Si	11.9 ± 0.3	1.044	0.550	29.72	75.0
Perovskite solar cells					
Lab scale devices	20.9 ± 0.7	0.991	1.125	24.92	74.5
Mini modules	17.25 ± 0.6	277	1.070	20.66	78.1
Submodules	11.7 ± 0.4	703	1.073	14.36	75.8
Dye sensitized solar cell					
Lab scale devices	11.9 ± 0.4	1.005	0.744	22.47	71.2
Mini modules	10.7 ± 0.4	26.55	0.754	20.19	69.9
Submodules	8.8 ± 0.3	398.8	0.697	18.42	68.7
Organic solar cells					
Lab scale devices	11.2 ± 0.3	0.992	0.780	19.30	74.2
Mini modules	9.7 ± 0.3	26.14	0.806	16.47	73.2

1.2 Halide perovskites for photovoltaic devices

Originally, the term perovskite referred to a mineral, CaTiO_3 , discovered by Gustav Rose in 1839 and named after Russian mineralogist Lev Perovski [27]. The concept of a perovskite structure then extended to any material that assume the general formula of ABX_3 , where A and B represent cations while X represent an anion. Typically A and B are metallic elements, while X is either O, C, N or a halogen. [28] It is quite interesting that silicate perovskite is the most abundant mineral in the lower mantle, but the unique structure of the perovskites was not emphasized until Goldschmidt published his work on tolerance factors [29]. Many different cations, inorganic or organic, can be embedded into the perovskite structure, providing enormous amount of viable analogous perovskite materials [30]. While perovskites with different elemental composition surely possess different properties, the most intriguing type of the perovskites is the halide perovskite, or to be more specific, the lead halide perovskite. Showing many excellent physical and optical properties, the lead halide perovskite was considered the most promising light absorber for the next generation solar cells as soon as it was employed in 2009, although it only reached

3.8% PCE at that moment [31]. With a surprisingly fast increase to 23.3% in 2018 [32], the lead halide perovskite has become the most studied perovskite material in the field of photovoltaics.

1.2.1 Crystal structure and properties of the halide perovskites.

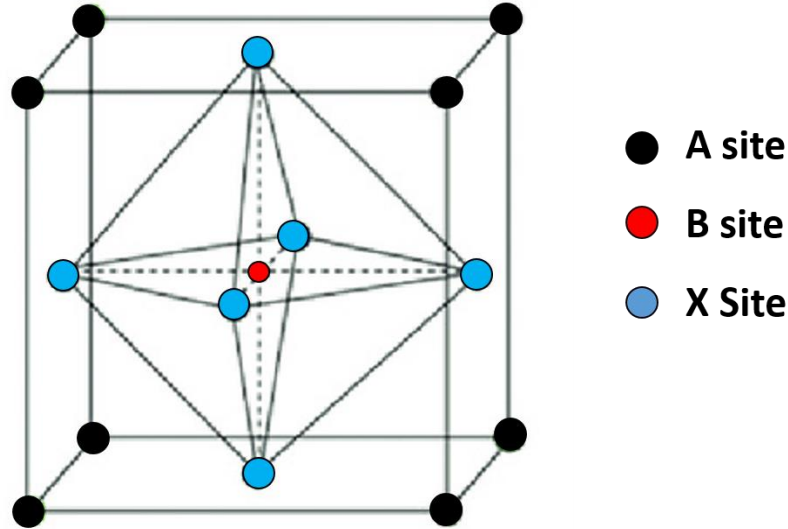


Fig.3 A typical lattice structure of a perovskite

Structure of a typical perovskite is shown in Fig.3. Put a lattice of a perovskite material assuming formula of ABX₃ into a 3D Cartesian coordinate system, we can see that the A site cations locate at the corner of the cubic lattice described as (0, 0, 0), the B site cations locate at the center of the lattice described as (1/2, 1/2, 1/2), and the X site anions locate at the face-center of the lattice described as (1/2, 1/2, 0). We can also inspect the lattice structure of the perovskite from another point of view. Fig.4 showed the crystal structure of MAPbI₃, a lead halide perovskite. We can clearly see the corner sharing octahedral lattice connecting to one another in three dimensions, while the A site cation locates in the cavity among 8 cubic units. This special structure causes that the size of A, B and X site ions would significantly affect the lattice stability of the halide perovskite. In order to describe the magnitude of stability of a perovskite, Goldschmidt [29] introduced tolerance factor (t). To be specific, by collecting data of the effective radii of each ions, the tolerance factor (t) and the octahedral factor (μ) can be calculated, and through these factors we can roughly have a concept about whether a perovskite is stable assuming cubic crystal lattice, and how is the distorting tendency of it [33]. Besides of the 3D perovskite, many 2D perovskites

were also developed, such as the Ruddleson-Popper phase perovskite [34], the Aurivillius phase perovskite [35], and the Dion-Jacobson phase perovskite [36]. These 2D perovskites can also have various applications, but we will not discuss them in details in this thesis, as they are usually not related to the photovoltaics.

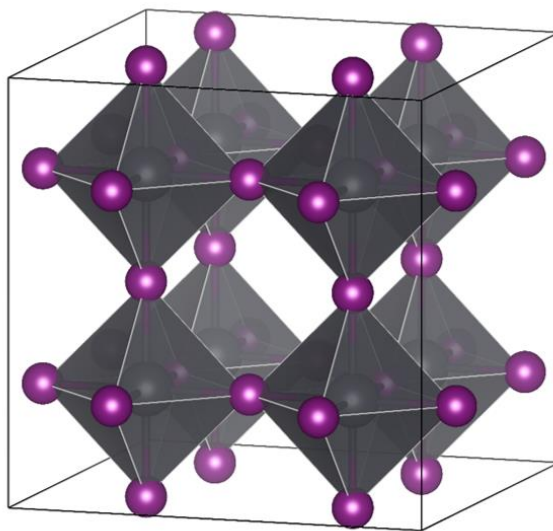


Fig.4 Scheme of the structure of a typical MAPbI_3 perovskite.

One amazing property of the lead halide perovskites is that they have direct bandgap. As we have discussed above in section 1.1, a direct bandgap means the material can provide high absorption with a thin film. This is especially important when considering commercial photovoltaic applications. Another important property of the lead halide perovskites is that their optoelectronic characters are highly tunable, with both the composition adjustments [37] and the lattice doping [38]. This property allows the halide perovskite to be applied to many optoelectronic devices, not only solar cells but also photodetectors, photocatalytic system, etc. The lead halide perovskite can also provide long carrier transport length and fine defect tolerance comparing to other crystalline photovoltaic materials [39].

1.2.2 Perovskite solar cell architectures and fabrication techniques.

Different from its oxide analogues, the halide perovskites allow simple solution process, since they have fine solubility in aprotic polar solutions at low temperature. Depending on the different fabrication processes to assemble a perovskite solar cell, different solvents such as γ -butyrolactone (GBL), dimethylformamide (DMF), dimethyl sulfoxide (DMSO), or their

mixture are used. Another important property of the halide perovskite is the inversed solubility, or the “retrograde solubility” in the aprotic polar solvents [40]. The solubility of a halide perovskite would decrease by about 20% when the solution is heated from 60°C to 90°C, and decrease by about 50% when heated to 120°C. This will cause the halide perovskite to rapidly precipitate when the solution is heated, and the retrograde crystallization method is widely used in preparing single crystals of the halide perovskite [41-42].

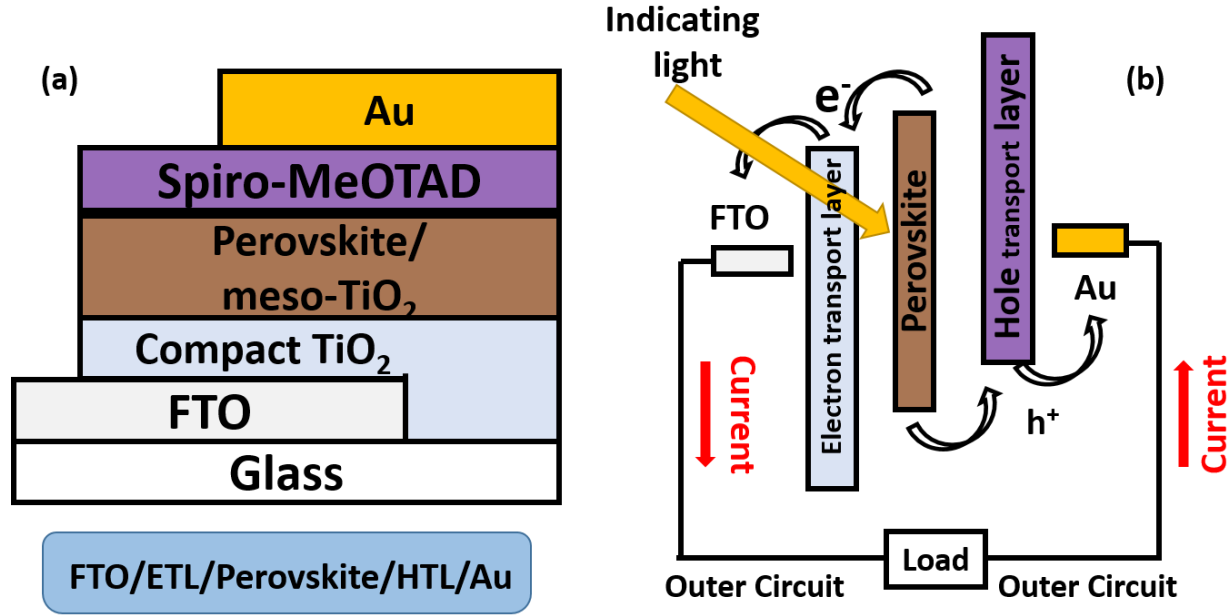


Fig.5 Sketch of (a) device architecture of a typical perovskite solar cell and (b) energy diagram of the perovskite solar cell showing the carrier cascade.

Fig.5 demonstrated the structure of a typical perovskite solar cell, and its energy diagram. To fabricate a well-defined perovskite solar cell device, it is necessary to choose an electron transport material (ETM) and a hole transport material (HTM) so as to extract and collect the electrons and holes generated by the excitation from the incident photon. Although devices without ETM and/or HTM are also viable, their performances are typically not as good as those with ETM and HTM [43-44]. Most widely used ETM are oxide semiconductors with large bandgap and good transparency, such as TiO₂, Al₂O₃, SnO₂, etc. [45-47]. Most widely used HTM is an organic conductive compound Spiro-OMeTAD. By arranging the conductive band minimum (CBM) of the ETM and the valance band maximum (VBM) of the HTM and let them align with the

perovskite, a cascade of the carriers can be formed and thus consists the core working principle of the perovskite solar cell.

Despite of the architecture, the fabrication routes of the perovskite solar cells can be divided into two main types, the spin coating fabrication and the chemical bath deposition fabrication. The chemical bath deposition is a relative “old” fabrication method, which includes dipping the substrate in the perovskite solution, let the perovskite crystals sediment, and form a dense film. This method is simple, and yields fine compact film, but requires a long deposition time, during which the system is easily disturbed and can be of poor reproducibility [48]. The chemical bath deposition usually requires a large amount of solution, but utilizing only a small portion of the raw material to form the film, thus resulting in great waste of reagents [49]. On the other hand, the spin coating method, where a small amount (typically micro liter magnitude) of precursor is dropped on a flat substrate and form the film with the centrifuge force by spinning the substrate at a steady rotating speed, usually take only tens of seconds to cast a film and the process is highly repeatable [50]. Nowadays the spin coating technique is the fundamental skill for perovskite solar cell fabrication, but it also has become one of the obstructions that prevents the perovskite solar cell from industry-scale fabrication, because the large scale spin coating is not viable, and other fabrication techniques cannot yield solar cells as good as those fabricated with spin coating. Surely many alternative fabrication techniques were developed, such as the low temperature pressing fabrication [51], roll-to-roll printing technique [52], etc., the solar cell fabrication techniques are still far from satisfying. We can anticipate that the improvement of the device fabrication technique will always be a key research topic in the near future.

1.3 Lead-free perovskites for solar cells

1.3.1 Issues of the lead halide perovskites.

In the previous section, we have discussed the development of the lead-based perovskite solar cells. Despite the exciting advantages and progress mentioned above, the lead-based solar cells still have several major problems. One main problem is the toxicity of the Pb^{2+} cation and the pollution caused by the loss of lead mass from the perovskite solar cell module. Study showed that Pb^{2+} cation affects the human nervous system as well as the reproductive system [53]. Due to the

easy decomposition of the perovskite materials in a humid environment or under strong UV radiation, decomposed lead perovskites would generate high concentration of Pb^{2+} cations. To make things worse, the decomposition of the lead perovskites can be significantly accelerated when considering real life scenarios. The mass loss of lead perovskites can result in pollution in large area of soil, water and atmosphere [54].

While the lead loss can be contained at a mild magnitude with careful encapsulation, another issue is that the degradation of the lead perovskite is generally irreversible. Moisture and high temperature are the most hazardous factors to the perovskite photovoltaics. Study showed that hybrid lead perovskite materials would exhibit rapid degradation under the conditions of either high moisture or high temperature (over 140°C), and these decomposition processes often happened at the defect sites located at the interfaces [55]. While in oxygen-rich environment, UV light can significantly promote the inducement of oxygen molecule diffusion through the perovskite layer. When the oxygen molecules reach the oxide semiconductor ETM, intrinsic photocatalytic reaction would take place and form peroxide or superoxide compounds [56]. This is one of the important degradation mechanisms of the perovskite layer. Another important mechanism of the perovskite degradation is that UV illumination can promote the generation of halogen radicals at local defect sites. Possessing high free energy, these halogen radicals would act as activated decomposing center [6]. The degradation of the perovskite layer can cause severe efficiency drop or even device failure in a short period, thus is crucial if we want to obtain stable perovskite solar cell modules.

1.3.2 Non-toxic elements to substitute lead in the perovskites

Many studies have been carried out in order to solve these key issues mentioned above. Generally, good encapsulation and careful fabricating techniques can mitigate the decomposition. However, the problems cannot be solved completely. A most plausible solution is to develop viable lead-free perovskites so that we can completely remove the lead element from the halide perovskites. Of course in certain circumstance the complete removal of the lead element is not quite realistic, then partial replacement can also be an option.

Until today, many substitute elements have been studied. If we look at the periodic table, tin (Sn) is the most similar element to lead. They both can form +2 valence compounds and the crystal structure of the halide perovskites based on Sn is similar to that of the lead perovskites. Sn-based

perovskites were predicted to maintain most of the optoelectronic properties of the lead perovskites due to similar lattice structure and bandgaps [57]. Partial substitution of lead by tin entered the scene at very early stage of the perovskite solar cell research. Initially the mixed lead-tin perovskite showed competitive PCE to the pure lead perovskite, and even suggested better potential showing a wide absorption range up to 1060 nm [58]. Very soon, solar cells based on pure tin perovskites were developed showing promising photovoltaic performance [59]. With the development of material modification methods and film fabrication techniques, the PCE of the partial substituted tin perovskite has reached over 12% [60] and fully substituted tin perovskite has reached over 9% [61].

However, tin-based perovskites were revealed to have certain shortcomings as well. Study showed that Sn^{2+} cations suffer from instability issue. When exposed to moisture or oxidation agent of any source, Sn^{2+} will rapidly oxidize into Sn^{4+} , thus causing the 3D perovskite to reduce to 2D or even succumb to decomposition [62]. In addition, study showed that tin perovskite would release I^- or HI during its decomposing process, causing acidification of the water system if released to the natural environment. This indicated that tin perovskite would also suffer from toxicity and pollution issues [63].

Another potential substitute is germanium. Located in the same family with lead, germanium can also form +2 valence compounds. Germanium has been used in thin film transistor and the 2nd generation solar cells for a long time before researches show germanium perovskites could have similar physical properties and band structures to the Pb and Sn perovskites [64-65]. The properties and applications of the oxide germanium perovskites were previously studied [66-67]. However, studies of the germanium halide perovskites as a light absorber in the photovoltaic field are limited. Computational studies and practical researches indicated that the germanium perovskites are capable of forming 3D cubic crystal structure, but possess significantly larger bandgap than their lead counterparts [68-69]. In recent years study on germanium perovskites diminished. Unable to solve the problem of the high price of the germanium and the large bandgap of the germanium perovskites, this material has not displayed superior potential for solar cell applications yet. Other elements that were predicted to form +2 valence perovskite structure include alkaline metal elements such as Sr and Ba [70-71], and transition metals such as Cu [72]. The alkaline metal perovskites would have very large bandgaps (>3.0), while the cupric perovskites would only form

2D structure due to the small effective ionic size. These elements have not shown evidence for effective solar cell applications either.

Bismuth is another potential substitute element of lead, which located next to lead on the periodic table. Computational predictions and experimental studies suggested that bismuth perovskites have less defect states, long carrier lifetime and proper defect tolerance ability [73-75]. It is also proved that bismuth is much less toxic comparing to the lead element [76]. Many studies on bismuth perovskites have been carried out in recent years, pushing the PCE of the bismuth perovskite from < 0.1 to over 3% [77].

On the other hand, many important problems of the pure bismuth perovskites have been revealed. Pure halide bismuth perovskite would crystalize into a 2D hexagonal layered phase, causing the perovskite film to have much more intrinsic defects [78]. Another issue is that bismuth perovskites tend to have large and indirect bandgaps (~ 2.0 eV), which is definitely not suitable for perovskite solar cells [79].

In order to counter the problems of the intrinsic defects, employing new fabrication techniques can be a viable way. It is reported that by employing vapour assisted solution p (VASP) method, which was used to modify lead perovskites, the crystal size of the bismuth perovskites can be reduced, and the leakage and V_{OC} loss can be mitigated [77]. Modifying the composition of the bismuth perovskites can also work. By introducing another metal cation to the bismuth perovskite and form a double perovskite, it is possible to gain 3D crystal structure. We will discuss this in details in next section. It is also reported that by modifying the composition of the bismuth perovskites, their bandgaps and absorption abilities can be enhanced [80]. Considering the stability and non-toxicity of the bismuth perovskites, it is of great value to study these modification methods in depth.

1.4 Lead-free double perovskites

1.4.1 Structure and properties of the double perovskites

Another way of utilizing lead-free materials is to introducing one more cation to the B site and form a double perovskite. Double perovskite (DP) first entered the scene as oxide multiferroics $AB_2B'O_6$ when researchers explored for new magnetic materials [81]. Most of the B and B' site

cations were transition metals, and most A site cations were alkaline or alkaline-earth metals. Being an all-inorganic compound, oxide DP displayed structural stability at a wide temperature range and magnetoresistance effect at ambient conditions [82].

Halide DPs drew attention recently as researchers scanning for new lead-free perovskites. By replacing the lead element in an APbX_3 halide perovskite by a pair of other metal cations, the product can assume the formula of $\text{A}_2\text{BB}'\text{X}_6$. Fig.6 shows the lattice unit of an ideal double perovskite, where the B and B' site cations would take up the central position of the lattice alternatively, and this ordered distribution would maintain throughout the whole structure of a halide DP. It is to be noticed that although in an ideal situation, B and B' would each take up 50% of the B sites, it is not a mandatory ratio for the double perovskite to form. In addition, halide DPs would also have halogen vacancies at A sites, as oxide DPs have oxygen vacancies. In this thesis when we talk about double perovskites, we refer to the halide double perovskites.

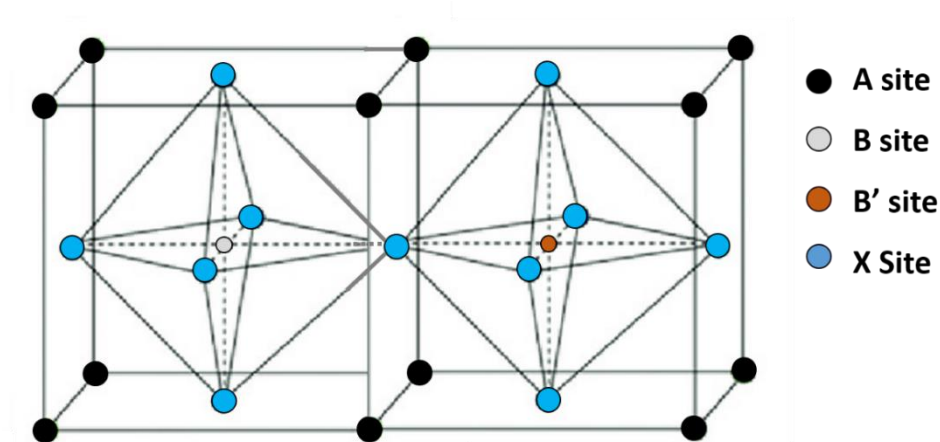


Fig.6 Typical lattice unit of a double perovskite.

1.4.2 Development of the lead-free halide double perovskites.

To date, the most discussed double perovskite combination is the Ag and Bi elements for the B sites. Xiao et al. have conducted a complex and detailed computational analysis on the thermodynamic stability, electronic structure and defect properties of the $\text{Cs}_2\text{AgBiBr}_6$ compound. They pointed out that the $\text{Cs}_2\text{AgBiBr}_6$ is less stable than the $\text{CH}_3\text{NH}_3\text{PbBr}_3$ material owing to the weak coupling between Bi 6s and Br 6p orbitals [83].

In addition, it is revealed that the $\text{Cs}_2\text{AgBiX}_6$ has a corner-shared octahedral framework, which is similar to that of the Pb-perovskite. This material exhibited excellent long PL decay time indicating long carrier lifetime. On the other hand, the calculations and experimental data showed that $\text{Cs}_2\text{AgBiX}_6$ has a large indirect bandgap of over 2 eV [84-88]

Apart from Ag/Bi double perovskites, many other B site cations were also studied. Volonakis et al. reported $\text{Cs}_2\text{InAgCl}_6$ double perovskite in 2017 [89]. First-principle calculations predicted that the $\text{Cs}_2\text{InAgCl}_6$ has a direct bandgap, which is an advantage for photovoltaic applications. However, the bandgap of this material is still very large (approaching 3 eV).

DPs with organic cations at A site were also studied. $\text{MA}_2\text{KBiCl}_6$ exhibited large bandgap of 3.04 eV despite its similar crystal structure as the Pb-based perovskites [90]. Cheng et al. also reported that a 2D hexagonal $\text{MA}_2\text{AgBiI}_6$ crystal possesses wide bandgap of 1.96 eV [91].

DPs listed above and reported elsewhere generally showed high stability that can reduce environmental impact. Consisting mostly non-toxic elements, the halide DPs indicated great potential for environment friendly solar devices.

The major disadvantage of the reported double perovskites is that their bandgaps are all large for use in single-junction solar cells. Hence, designing a low bandgap double perovskite halide is in great need where the new double perovskite should have a proper bandgap with wide absorption range across the solar spectra, and it should maintain the advantages of the double perovskites such as stable and non-toxic.

1.5 Single crystals

Single crystal (SC), also known as monocrystalline solid, can be described as a solid who has orderly three-dimensional continuous crystal lattice throughout the entire particle. The lack of defects can provide unique mechanical strength, optical properties and electrical characteristics

[92]. The most well-known SC material related to the photovoltaic devices is the silicon SC solar cells. SCs are also applied to other optoelectronic fields such as lasers [93] and photodetectors [94].

1.5.1 Single crystals and perovskite solar cells

The majority of the perovskite solar cells reported are based on polycrystalline films. Polycrystalline films generally suffer from higher trap density and higher grain boundaries [95]. Obviously, these traps and grain boundaries attributed to a great portion of the instability of the perovskite solar cells that hindered the commercial scale application of the perovskite solar cells.

On the other hand, SC demonstrated many superior advantages compared to the polycrystalline films. Attributing to their higher crystallinity, fewer defects, absence of grain boundaries and superior stability [96-99], single crystals are potential for fabricating high performance solar cells. This is proved with silicon solar cells, where SC silicon solar cell yields over 26% PCE and polycrystalline silicon solar cell yields 22% [100]. If we can fabricate perovskite solar cells with single crystal wafer/film, then the breakthrough of the PCE can be expected.

1.5.2 Development of the perovskite single crystals

In order to obtain well-defined perovskite SCs, a variety of solution-based approaches were developed, including the hot solution cooling growth [101], the anti-solvent vapor-assisted crystallization [102], the top-seeded growth [95], the inverse temperature crystallization [103-104], and the solvent acidolysis crystallization [105].

Although hybrid lead perovskite SCs and inorganic lead perovskite SCs both reached over 10 mm in scale, only a few reported successful device fabrication with these materials. One important reason is that the mechanical strength of the perovskite SCs are low and it is hard to obtain wafer or film from bulk macro SC. On the other hand, micro SCs suggested successful application to the solar cell devices [106-107]. The same methodology can be introduced to the lead-free perovskite material preparation, and it may be able to solve the problem that the lead-free perovskites can only yield low quality polycrystalline film.

1.6 Challenges and Research topics

As discussed above, the halide perovskite solar cells have become the most promising 3rd generation solar cells. However, three major challenges still lie in the way towards commercial application of the perovskite solar cells. First, the stability of the perovskite material needs to be improved in order to achieve long-term stable output. Second, the toxic waste and pollution generated by the degradation of the perovskite material need constrain and management. Third, the scale-up performance of the perovskite solar cell needs to be enhanced in order to fulfil the requirement of the industrial scale fabrication and real life scenario utilization.

Inspecting these challenges, we can conclude that the perovskite material itself played the key part on the performance of the solar cells. In order to promote the further development of perovskite solar cells, new materials were developed in this thesis to assess the shortcoming of the lead halide perovskites. First, mixed chalcogenide-halide bismuth perovskite was explored for lead-free perovskite solar cells. Second, bismuth double perovskite was prepared by hydrothermal process to assess the large bandgap and poor morphology problems of the bismuth perovskites. Third, the micro single crystals of the bismuth double perovskite was investigated to further inspect the optimized growth condition of the bismuth double perovskite.

References

- [1]. Palz W. Power for the World: The Emergence of Electricity from the Sun. Belgium: Pan Stanford Publishing. 2010.
- [2]. Chapin D, Fuller C, Pearson G. A New Silicon P-N Junction Photocell for Converting Solar Radiation into Electrical Power. *J. Appl. Phys.* 1954;**25**, 676-677.
- [3]. Energy Initiative Massachusetts Institute of Technology. The Future of Solar Energy- an interdisciplinary MIT study. 2015.
- [4]. Kazmerski L. Best research cell efficiencies. National Renewable Energy Laboratory. 2010.
- [5]. Green M, Emery K, Hishikawa Y, Warta W, Dunlop E. Solar Cell Efficiency Tables (Version 45). *Prog. Photovolt: Res. Appl.* 2015;**23**, 1-9.
- [6]. Green M. Crystalline and Thin-Film Silicon Solar Cells: State of the Art and Future Potential. *Sol Energy*. 2003;74, 181-192.
- [7]. Kamat P. Evolution of Perovskite Photovoltaics and Decrease in Energy Payback Time. *J Phys Chem Lett.* 2013;4, 3733-3734.
- [8]. Reichelstein S, Yorston M. The Prospects for Cost Competitive Solar PV Power. *Energy Policy*. 2013;55, 117-127.
- [9]. García-Valverde R, Cherni J, Urbina A. Life Cycle Analysis of Organic Photovoltaic Technologies. *Progress Photovolt: Res Appl*, 2010;18, 535-558.
- [10]. Cucchiella F, D'Adamo I, Gastaldi M, Koh S. Renewable Energy Options for Buildings: Performance Evaluations of Integrated Photovoltaic Systems. *Energy Build.* 2012;55, 208-217.
- [11]. Taguchi M, Yano A, Tohoda S, Matsuyama K, Nakamura Y, Nishiwaki T, et al. 24.7% Record Efficiency HIT Solar Cell on Thin Silicon Wafer. *Photovolt, IEEE J Of.* 2014;4, 96-99.
- [12]. U.S. Energy Information Administration. International Energy Outlook 2016. Chapter 5: Electricity.
- [13]. Cao C, Jiang W, Wang B, et al. Inhalable Microorganisms in Beijing's PM2.5 and PM10 Pollutants during a Severe Smog Event. *Environ. Sci. Technol.* 2014;**48** (3), 1499-1507.
- [14]. Sark W, Muizebelt P, Cace J, Vries A, Rijk P. Price Development of Photovoltaic Modules, Inverters, and Systems in the Netherlands in 2012. *Renew. Energy*. 2014;71, 18-22.
- [15]. PV Insights. PVinsights: Solar Photovoltaic (Polysilicon wafer cell and panel) Prices and Research Reports. 2014. URL: <http://www.pvinsights.com/>
- [16]. Louwen A, Sark W, Schropp R, Faaij A. A Cost Roadmap for Silicon Heterojunction Solar Cells. *Sol Energ Mat Sol Cells*. 2016;147, 295-314.
- [17]. Qariny W, Hossain MI, Hossain MK, et al. Efficient Amorphous Silicon Solar Cells: Characterization, Optimization, and Optical Loss Analysis. *Results Phys.* 2017;7, 4278-4293.
- [18]. Shah A, Torres P, Tscharnner R, Wyrsh N, Keppner H. Photovoltaic Technology: The Case for Thin-Film Solar Cells. *Science*. 1999;285(5428), 692-698.

- [19]. Green M, Hishikawa Y, Dunlop E, Levi D, Hohl-Ebinger J, Ho-Baillie A. Solar Cell Efficiency Tables (version 52). *Prog Photovolt Res Appl*. 2018;26:427–436.
- [20]. Lee T, Ebong A. A Review of Thin Film Solar Cell Technologies and Challenges. *Renew Sust Energ Rev*. 2017;70, 1286-1297.
- [21]. O'Regan B, Grätzel M. A Low-Cost, High-Efficiency Solar Cell Based on Dye-Sensitized Colloidal TiO₂ Films. *Nature*. 1991;353(6346), 737–740.
- [22]. Perez-Tomas A, Mingorance A, Reyna Y, Lira-Cantu M. The Future of Semiconductor Oxides in Next Generation Solar Cells. Singapore: Elsevier; 2017 published.
- [23]. Thogiti S, Park J, Thi T, et al. High performance Dye-sensitized Solar Cells through Graded Electron Transport in Band-Engineering W-TiO₂ Cascade Layer. *Sustainable Chem Eng*. 2018.
- [24]. Bhardwaj S, Pal A, Chatterjee K, et al. Fabrication of efficient dye-sensitized solar cells with photoanode containing TiO₂–Au and TiO₂–Ag plasmonic nanocomposites. *J Mater Sci: Mater Electron*. 2018.
- [25]. Yan J, Saunders B. Third-Generation Solar Cells: A Review and Comparison of Polymer:fullerene, Hybrid Polymer and Perovskite Solar Cells. *RSC Adv*. 2014;4, 43286-43314.
- [26]. NREL. Best Research-Cell Efficiencies. NREL. 2018. URL: <https://www.nrel.gov/pv/assets/pdfs/pv-efficiencies-07-17-2018.pdf>
- [27]. Wenk HR, Bulakh A. Minerals: Their Constitution and Origin. New York, NY: Cambridge University Press. 2004.
- [28]. Kim H, Im S, Park N. Organolead Halide Perovskite: New Horizons in Solar Cell Research. *J Phys Chem C*. 2014;118, 5615-5625.
- [29]. Goldschmidt VM. Die Gesetze der Krystallochemie. *Naturwissenschaften*. 1926 May;14(21):477-485.
- [30]. Swarnkar A, Ravi VK, Nag A. Beyond Colloidal Cesium Lead Halide Perovskite Nanocrystals: Analogous Metal Halide and Doping. *ACS Energy Lett*. 2017;2(5):1089-1098.
- [31]. Kojima A, Teshima K, Shirai Y, Miyasaka T. Organometal halide perovskites as visible-light sensitizers for photovoltaic cells. *J Am Chem Soc*. 2009 May 6;131(17):6050-6051.
- [32]. Yang Y, You J, Lei M, inventors. The Regents of the University of California (Oakland, CA, US), assignee. Efficient and Stable Perovskite Solar Cells with All Solution Processed Metal Oxide Transporting Layers. United States Patent 0033983. 2018-02-01.
- [33]. Li C, Lu X, Ding W, et al. Formability of ABX₃ (X = F, Cl, Br, I) halide perovskites. *Acta Crystallogr B*. 2008 Nov 14;64(6):702-707.
- [34]. Ruddlesden SN, Popper P. The Compound Sr₃Ti₂O₇ and Its Structure. *Acta Crystallogr*. 1958 Jan;11(1):54-55.
- [35]. Tellier J, Boullay P, Manier M, Mercurio D. A comparative study of the Aurivillius phase ferroelectrics CaBi₄Ti₄O₁₅ and BaBi₄Ti₄O₁₅. *J Solid State Chem*. 2004 Mar 8;177(6):1829-1837.

- [36]. Benedek NA. Origin of Ferroelectricity in a Family of Polar Oxides: The Dion-Jacobson Phases. *Inorg Chem*, 2014 Mar 28;53(7):3769-3777.
- [37]. Eperon GE, Stranks SD, Menelaou C, Johnston MB, Herz LM, Snaith HJ. Formamidinium Lead Trihalide: A Broadly Tunable Perovskite for Efficient Planar Heterojunction Solar Cells. *Energy Environ Sci*. 2014 Jan 06;7(3):982-988.
- [38]. Zhang Z, Wang M, Ren L, Jin K. Tunability of Band Gap and Photoluminescence in CH₃NH₃PbI₃ Films by Anodized Aluminum Oxide Templates. *Sci Rep*. 2017 May 15;7:1918.
- [39]. Kovalenko MV. Protesescu L. Bodnarchuk MI. Properties and potential optoelectronic applications of lead halide perovskite nanocrystals. *Science*. 2017 Nov 10;358(6364):745-750.
- [40]. Saidaminov MI. Abdelhady AL. Maculan G. Bakr OM. Retrograde Solubility of Formamidinium and Methylammonium Lead Halide Perovskites Enabling Rapid Single Crystal Growth. *Chem Commun*. 2015 Oct 20;51(100):17658-17661.
- [41]. Fang HH. Adjokatse S. Wei H. Yang J. Blake GR. Huang J. Even J. Loi MA. Ultrahigh Sensitivity of Methylammonium Lead Tribromide Perovskite Single Crystals to Environmental Gases. *Sci Adv*. 2016 Jul 27;2(7):1600534.
- [42]. Almadori Y. Moerman D. Martinez JL. Leclerc P. Grevin B. Multimodal Noncontact Atomic Force Microscopy and Kelvin Probe Force Microscopy Investigations of Organolead Tribromide Perovskite Single Crystals. *Beilstein J Nanotechnol*. 2018 Jun 07;9:1695-1704.
- [43]. Pascual J. Kosta I. Ngo TT. Chuvillan A. Cabanero G. Grande HJ. et al. Electron Transport Layer-Free Solar Cells Based on Perovskite–Fullerene Blend Films with Enhanced Performance and Stability. *ChemSusChem*. 2016 Sep 22;9(18):2679-2685.
- [44]. Wagner L. Chacko S. Mathiazhagan G. Mastroianni S. Hinsch A. High Photovoltage of 1 V on a Steady-State Certified Hole Transport Layer-Free Perovskite Solar Cell by a Molten-Salt Approach. *ACS Energy Lett*. 2018 Mar 16;3(5):1122–1127.
- [45]. Liu M. Johnston MB. Snaith HJ. Efficient Planar Heterojunction Perovskite Solar Cells by Vapor Deposition. *Nature*. 2013 Sep 19;501:395-398.
- [46]. Lee MM. Teuscher J. Miyasaka T. Murakami TN. Snaith HJ, Efficient Hybrid Solar Cells Based on Meso-Superstructured Organometal Halide Perovskites. *Science*. 2012 Nov 02;338(6):643-647.
- [47]. Dong Q. Shi Y. Wang K. Li Y. Wang S. Zhang H. et al. Insight into perovskite solar cells based on SnO₂ compact electron-selective layer. *J Phys Chem C*. 2015 Apr 15;119(19):10212-10217.
- [48]. Nair PK. Nair MTS. Garcia VM. Arenas OL. Pena Y. Castillo A. et al. Semiconductor Thin Films by Chemical Bath Deposition for Solar Energy Related Applications. *Sol Energ Mat Sol Cells*. 1998 Apr 30;52(3): 313-344.

- [49]. Hariskos D. Powalla M. Chevaldonnet N. Lincot D. Schindler A. Dimmler B. Chemical Bath Deposition of CdS Buffer Layer: Prospects of Increasing Materials Yield and Reducing Waste. *Thin Solid Film*. 2001 May 29;387(1):179-181.
- [50]. Ossila. Spin Coating: A Guide to Theory and Techniques [Internet]. Ossila UK. 2017 [cited 01 Sep 2018]. Available from: <https://www.ossila.com/pages/spin-coating/>
- [51]. Chen H. Ye F. Tang W. He J. Yin M. Wang Y. et al. A Solvent- and Vacuum-Free Route to Large-Area Perovskite Films for Efficient Solar Modules. *Nature*. 2017 Oct 5; 550(7674):92-95.
- [52]. Hwang K, Jung YS, Heo YJ, Scholes FH, Watkins SE, Subbiah J, et al. Toward Large Scale Roll-to-Roll Production of Fully Printed Perovskite Solar Cells. *Adv Mater*. 2015 Feb 18;27(7):1241-7.
- [53]. Gidlow DA. Lead Toxicity. *Occupational Medicine*. 2004 Mar 01;54(2):76–81.
- [54]. Hailegnaw B. Kirmayer S. Edri E. Hodes G. Cahen D. Rain on Methylammonium Lead Iodide Based Perovskites: Possible Environmental Effects of Perovskite Solar Cells. *J Phys Chem Lett*. 2015 Apr 07;6(9):1543-1547.
- [55]. Pathak SK. Abate A. Ruckdeschel P. Roose B. Gozdel KC Vaynzof Y. et al. Performance and Stability Enhancement of Dye-Sensitized and Perovskite Solar Cells by Al Doping of TiO₂. *Adv Funct Mater*. 2014 Jul 22;24(38):6046–6055.
- [56]. Pathak SK. Abate A. Leijtens T. Hollman DJ. Teuscher J, Pazos L. et al, Towards Long-Term Photostability of Solid-State Dye Sensitized Solar Cells. *Adv Energy Mater*. 2014 Jun 3;4(8):1301667.
- [57]. Stoumpos CC. Malliakas CD. Kanatzidis MG. Semiconducting Tin and Lead Iodide Perovskites with Organic Cations: Phase Transitions, High Mobilities, and Near-Infrared Photoluminescent Properties. *Inorg Chem*. 2013 Jul 08;52(15):9019–9038.
- [58]. Ogomi Y, Morita A. Tsukamoto S. Saitho T. Fujikawa N, Shen Q. et al. CH₃NH₃Sn_xPb_(1-x)I₃ Perovskite Solar Cells Covering up to 1060 nm. *J Phys Chem Lett*. 2014 Mar 3;5(6):1004–1011.
- [59]. Noel N. Stranks S. Abate A. Wehrenfennig C. Guarnera S. Haghighirad A. et al. Lead-Free Organic–Inorganic Tin Halide Perovskites for Photovoltaic Applications. *Energy Environ Sci*. 2014 May 01;7:3061-3068.
- [60]. Lee S. Kang DW. Highly Efficient and Stable Sn-Rich Perovskite Solar Cells by Introducing Bromine. 2017 Jun 26;9(27):22432-22439.
- [61]. Shao S. Liu J. Portale G. Fang HH. Blake GR. ten Brink GH. et al. Highly Reproducible Sn-Based Hybrid Perovskite Solar Cells with 9% Efficiency. *Adv Energy Mater*. 2018 Feb 5;8(4):1702019.
- [62]. Liao Y. Liu H. Zhou W. Yang D. Shang Y. Shi Z. et al. Highly Oriented Low-Dimensional Tin Halide Perovskites with Enhanced Stability and Photovoltaic Performance. *J Am Chem Soc*. 2017 Apr 24;139(19):6693-6699.

- [63]. Babayigit A. Thanh DD. Ethirajan A. Manca J. Muller M. Boyen HG. Conings B. Assessing the Toxicity of Pb- and Sn-Based Perovskite Solar Cells in Model Organism *Danio Rerio*. *Sci Rep*. 2016 Jan 13;6:18721.
- [64]. Yamada K. Isobe K. Tsuyama E Okuda T. Furukawa Y. Successive Phase Transitions and High Ionic Conductivity of Trichlorogermanate (II) Salts as Studied by ^{35}Cl NQR and Powder X-Ray Diffraction. *Z Naturforsch A*. 2014 Jun 02;49:258–266.
- [65]. Clark SJ. Donaldson JD. Harvey JA. Evidence for the Direct Population of Solid-State Bands by Non-Bonding Electron Pairs in Compounds of the Type $\text{CsM}^{\text{II}}\text{X}_3$ ($\text{M}^{\text{II}} = \text{Ge, Sn, Pb}$; $\text{X} = \text{Cl, Br, I}$). *J Mater Chem*. 1995;5(11):1813-1818.
- [66]. Fuh HR. Liu YP, Chen SH. Wang YK. Electronic Structures of Compensated Magnetism in Double Perovskites $\text{A}_2\text{CrRu}(\text{Os})\text{O}_6$ ($\text{A} = \text{Si, Ge, Sn, and Pb}$) from *ab initio* Calculations. *J Alloys Compd*. 2013 Jan 15;547:126–131.
- [67]. Taib MFM. Yaakob MK. Badrudin FW. Rasiman MSA. Kudin TIT. Hassan OH. Yahya MZA. First-Principles Comparative Study of the Electronic and Optical Properties of Tetragonal (P4mm) ATiO_3 ($\text{A} = \text{Pb, Sn, Ge}$). *Integrated Ferroelectrics*. 2014;155(1):23–32.
- [68]. Sun PP. Li QS. Yang LN. Li ZS. Theoretical Insights into a Potential Lead-Free Hybrid Perovskite: Substituting Pb^{2+} with Ge^{2+} *Nanoscale*. 2016 Jan 21.8(3):1503-1512.
- [69]. Krishnamoorthy T. Ding H. Yan C. Leong WL. Baikie T. Zhang ZY. et al. Lead-free germanium iodide perovskite materials for photovoltaic applications. *J Mater Chem A*. 2015 Dec 21;3(47):23829-23832.
- [70]. Bai XG. Shi YT. Wang K. Dong QS. Xing YJ. Zhang H. et al. *Acta Phys-Chim Sin*. 2015;31(2):285-290.
- [71]. Jacobsson TJ. Pazoki M. Hagfeldt A. Edvinsson T. J. Goldschmidt's Rules and Strontium Replacement in Lead Halogen Perovskite Solar Cells: Theory and Preliminary Experiments on $\text{CH}_3\text{NH}_3\text{SrI}_3$. *J Phys Chem C*. 2015 Oct 26;119(46):25673–25683
- [72]. Cui XP. Jiang KJ. Huang JH. Zhang QQ. Su MJ. Yang LM et al. Cupric Bromide Hybrid Perovskite Heterojunction Solar Cells. *Synthetic Metals*. 2015;209:247–250.
- [73]. Zhou H. Chen Q. Li G. Luo S. Song T. Duan H. et al. Interface engineering of highly efficient perovskite solar cells. *Science*. 2014 Aug 01;345(6196):542-546.
- [74]. Johansson MB. Zhu H. Johansson EMJ. Extended Photo-Conversion Spectrum in Low-Toxic Bismuth Halide Perovskite Solar Cells, *J Phys Chem Lett*. 2016;7(17):3467-3471.
- [75]. Hoye RLZ. Brandt RE. Osherov A. Stevanovic V. Stranks SD. Wilson MWB. et al. Methylammonium Bismuth Iodide as a Lead-Free, Stable Hybrid Organic–Inorganic Solar Absorber. *Chem Eur J*. 2016 Feb 18;22(8):2605-2610.
- [76]. Hebig J, Kuhn I, Flohre J, Kirchartz, T. Optoelectronic Properties of $(\text{CH}_3\text{NH}_3)_3\text{Sb}_2\text{I}_9$ Thin Films for Photovoltaic Applications. *ACS Energy Lett*. 2016 Jun 21;1(1):309-314.
- [77]. Jain SM. Phuyal D. Davies ML. Li M. Philippe B. Castro CD. et al. An Effective Approach of Vapor Assisted Morphological Tailoring for Reducing Metal Defect Sites in Lead-Free,

- (CH₃NH₃)₃Bi₂I₉ Bismuth-Based Perovskite Solar Cells for Improved Performance and Long-Term Stability. *Nano Energy*. 2018 Jul;49:614-624.
- [78]. Eckhardt K, Bon V, Getzschmann J, Grothe J, Wisser FM, Kaskel S. Crystallographic Insights into (CH₃NH₃)₃(Bi₂I₉): A New Lead-Free Hybrid Organic–Inorganic Material as a Potential Absorber for Photovoltaics. *Chem Commun*. 2016 Jan 19;52:3058-3060.
- [79]. Murugan V. Ohta T. Iikubo S. Kapil G. Ripolles TS. Ogomi Y. Ma T. Pandey SS. Shen Q. Toyoda T. Yoshino T. Minemoto T. Hayase S. Facile Synthesis and Characterization of Sulfur Doped Low Bandgap Bismuth Based Perovskites by Soluble Precursor Route. *Chem Mater*. 2016;28(18):6436-6440.
- [80]. Lehner AJ. Fabiani DH. Evans HA. Hebert CA. Smock SR. Hu J. Crystal and Electronic Structures of Complex Bismuth Iodides A₃Bi₂I₉ (A = K, Rb, Cs) Related to Perovskite: Aiding the Rational Design of Photovoltaics. *Chem Mater*. 2015 Oct 4;27(20):7137–7148.
- [81]. Kobayashi KI. Kimura T. Sawada H. Terakura K. Tokura Y. Room-Temperature Magnetoresistance in an Oxide Material with an Ordered Double-Perovskite Structure. *Nature*. 1998 Oct 15;395:677-680.
- [82]. Sarma DD. Sampathkumaran EV. Ray S. Nagarajan R. Majumdar S. Kumar A. et al. Magnetoresistance in Ordered and Disordered Double Perovskite Oxide, Sr₂FeMoO₆. *Solid State Commun*. 2000 Apr 09;144(9):465-468.
- [83]. Xiao Z. Meng M. Wang J. Yan Y. Thermodynamic Stability and Defect Chemistry of Bismuth-Based Lead-Free Double Perovskites. *ChemSusChem*. 2016 Sep 22;9(18):2628 – 2633.
- [84]. Volonakis G. Filip M. Haghighirad A. Sakai N. Wenger B. Snaith H. et al. Lead-Free Halide Double Perovskites via Heterovalent Substitution of Noble Metals. *J Phys Chem Lett*. 2016 Mar 16;7(7):1254-1259.
- [85]. Wei F. Deng Z. Sun S. Zhang F. Evans D. Kieslich G. et al. Synthesis and Properties of a Lead-Free Hybrid Double Perovskite: (CH₃NH₃)₂AgBiBr₆. *Chem Mater*. 2017, Jan 06;29(3):1089–1094.
- [86]. Filip M. Hillman S. Haghighirad A. Snaith H. Giustino F. Band Gaps of the Lead-Free Halide Double Perovskites Cs₂BiAgCl₆ and Cs₂BiAgBr₆ from Theory and Experiment. *J Phys Chem Lett*. 2016 Jun 20;7(13):2579–2585.
- [87]. Slavney A. Hu T. Lindenberg A. Karunadasa H. A Bismuth-Halide Double Perovskite with Long Carrier Recombination Lifetime for Photovoltaic Applications. *J Am Chem Soc*. 2016 Feb 07;138(7):2138–2141.
- [88]. McClure E. Ball M. Windl W. Woodward P. et al. Cs₂AgBiX₆ (X = Br, Cl): New Visible Light Absorbing, Lead-Free Halide Perovskite Semiconductors. *Chem Mater*. 2016 Feb. 10;28(5):1348–1354.
- [89]. Volonakis G. Haghighirad A. Milot R. Sio W. Filip M. Wenger B. et al. Cs₂InAgCl₆: A New Lead-Free Halide Double Perovskite with Direct Band Gap. *J Phys Chem Lett*. 2017 Jan 30;8(4):772-778.

- [90]. Wei F. Deng Z. Sun S. Xie F. Kieslich G. Evans D. et al. The Synthesis, Structure and Electronic Properties of a Lead-Free Hybrid Inorganic–Organic Double Perovskite (MA)₂KBiCl₆ (MA = methylammonium). *Mater Horiz.* 2016 Apr 15;3: 328-332.
- [91]. Cheng P. Wu T. Li Y. Jiang L. Deng W. Han K. et al. Combining Theory and Experiment in the Design of a Lead-Free ((CH₃NH₃)₂AgBiI₆) Double Perovskite. *New J Chem.* 2017 Aug 08;41:9598-9601.
- [92]. Shimura F. Single-Crystal Silicon: Growth and Properties. In: Kasap S., Capper P. (eds) Springer Handbook of Electronic and Photonic Materials. Springer, Boston, MA. 2006.
- [93]. Park HG. Kim SH. Kwon SH. Ju YG. Yang JK Baek JH. et al. Electrically Driven Single-Cell Photonic Crystal Laser. *Science.* 2004 Sep 03;305(5689):1444-1447.
- [94]. Carrano JC. Li T. Grudowski PA. Eiting CJ. Dupuis RD. Campbell JC. Comprehensive Characterization of Metal–Semiconductor–Metal Ultraviolet Photodetectors Fabricated on Single-Crystal GaN. *J Appl Phys.* 1998 Oct 13;83(11):6148.
- [95]. Dong Q. Fang Y. Shao Y. Mulligan P. Qiu J. Cao L. Huang J. Electron-Hole Diffusion Lengths > 175 μm in Solution-Grown CH₃NH₃PbI₃ Single Crystals. *Science.* 2015 Feb 27;347(6225):967-970.
- [96]. Lian Z. Yan Q. Lv Q. Wang Y. Liu L. Zhang L. et al. High-Performance Planar-Type Photodetector on (100) Facet of MAPbI₃ Single Crystal. *Sci Rep.* 2015 Nov 13;5:16563.
- [97]. Peng W. Wang L. Murali B. Ho KT. Bera A. Cho N. et al. Solution-Grown Monocrystalline Hybrid Perovskite Films for Hole-Transporter-Free Solar Cells. *Adv Mater.* 2016 May 04;28(17):3383-3390.
- [98]. Rao HS. Li WG. Chen BX. Kuang DB. Su CY. In Situ Growth of 120 cm² CH₃NH₃PbBr₃ Perovskite Crystal Film on FTO Glass for Narrowband-Photodetectors. *Adv Mater.* 2017 Apr 25;29(16):1602639.
- [99]. Rao HS. Chen BX. Wang XD. Kuang DB. Su CY. A Micron-Scale Laminar MAPbBr₃ Single Crystal for an Efficient and Stable Perovskite Solar Cell. *Chem Commun.* 2017 May 07;53(37): 5163-5166.
- [100]. Green M. Hishikawa Y. Dunlop E. Levi D. Hohl-Ebinger J. Ho-Baillie A. Solar Cell Efficiency Tables (version 52). *Prog Photovolt Res Appl.* 2018;26:427–436.
- [101]. Mitzi DB. Synthesis, Structure, and Properties of Organic-Inorganic Perovskites and Related Materials. *Prog Inorg Chem.* 2007 Mar 09;48:1-121.
- [102]. Shi D. Adinolfi V. Comin R. Yuan M. Alarousu E. Buin A. et al. Low trap-state density and long carrier diffusion in organolead trihalide perovskite single crystals. *Science.* 2015 Jan 30;347(6221):519-522.
- [103]. Saidaminov MI. Abdelhady AL. Murali B. Alarousu E. Burlakov VM. Peng W. et al. High-Quality Bulk Hybrid Perovskite Single Crystals within Minutes by Inverse Temperature Crystallization. *Nat Commun.* 2015 Jul 06;6:7586.

- [104]. Zhang T. Yang M. Benson EE. Li Z. van de Lagemaat J. Luther JM. et al. A Facile Solvothermal Growth of Single Crystal Mixed Halide Perovskite $\text{CH}_3\text{NH}_3\text{Pb}(\text{Br}_{1-x}\text{Cl}_x)_3$. *Chem Commun.* 2015 May 07;51(37):7820-7823.
- [105]. Kulbak M. Cahen D. Hodes G. How Important Is the Organic Part of Lead Halide Perovskite Photovoltaic Cells? Efficient CsPbBr_3 Cells. *J Phys Chem Lett.* 2015 Jun 10;6(13):2452-2456.
- [106]. Wu J. Ye F. Yang W. Xu Z. Luo D. Su R. et al. Perovskite Single-Crystal Microarrays for Efficient Photovoltaic Devices. *Chem Mater.* 2018 Jul 11;30(14):4590-4596.
- [107]. Chen Z. Dong Q. Liu Y. Bao C. Fnag Y. Lin Y. et al. Thin Single Crystal Perovskite Solar Cells to Harvest below-Bandgap Light Absorption. *Nat Commun.* 2017 Dec 01;8:1890.

Chapter 2. Experimental section of the general methods and characterization techniques

In this thesis multiple synthesizing methods of the target materials, fabricating routines of the photovoltaic devices and characterization techniques were involved. As listed below, the related materials, instruments and methodologies were introduced.

2.1 Raw materials and apparatus

2.1.1 Raw materials

Listed below is a table of the engaged chemical reagents in this thesis. It should be pointed out that all the chemical reagents were purchased directly from the suppliers without further purifications.

Table 1. Chemical reagents employed in this thesis

	Reagent	Purity	Company
1	Tetrabutyl titanate	AR	Sigma-Aldrich
2	Meso-TiO ₂ paste	18NRD paste	Great Cell Solar (Dyesol) LTD.
3	FTO glass	glass	Opvtech
4	Ethanol	Super Dehydrated	Wako Pure Chemical Industries
5	Li-TFSI	99.99%	Macklin Co., LTD.
6	Spiro-MeOTAD	99.7%	Macklin Co., LTD.
7	Chlorobenzene	99.9%	Sigma-Aldrich
8	N, N-dimethylformamide	99.9%	Sigma-Aldrich

9	Dimethyl sulfoxide	99.9%	Sigma-Aldrich
10	PbI ₂	98%	Tokyo Chemical Industry Co., LTD.
11	CH ₃ NH ₃ I	99%	Great Cell Solar (Dyesol) LTD.
12	4-tert-butylpyridine	AR	Sigma-Aldrich
13	PEDOT:PSS	99%	Sigma-Aldrich
14	Ag	99.999%	Alfa Aesar
15	2-Propanol	Super Dehydrated	Wako Pure Chemical Industries
16	BiI ₃	99.999%	Sigma-Aldrich
17	CsI	99.999%	Sigma-Aldrich
18	NaI	99.999%	Sigma-Aldrich
19	acetone	99%	Wako Pure Chemical Industries
20	Acetonitrile	Super Dehydrated	Wako Pure Chemical Industries
21	Hydroiodic Acid	9M	Sigma-Aldrich
25	Titanium (IV) Tetrabutoxide monomer	95.0%	Wako Pure Chemical Industries
26	2,2'-Iminodiethanol	98.0%	Wako Pure Chemical Industries

2.1.2 Apparatus

Listed below is a table of the apparatus and testing instruments employed in this thesis. In the following sections all the testing devices refers to this table if not specified.

Table 2. Laboratory apparatus employed in this thesis

	Apparatus	MODEL	Company
1	Electronic Balance	XFR-205DR	Shinko Denshi Co., Ltd.
2	Muffle Furnace	FO300	Yamato Scientific Co., Ltd., Japan
3	Oven	SDN/W-27	Sansyo Co., Ltd., Japan
4	Spin coater	SC-150	Oshigane Co., Ltd., Japan
5	Hot plate	C-MAG HS7	IKA Co., Ltd., Germany
6	Vacuum oven	SVD-30	Sansyo Co., Ltd., Japan
7	ASU cleaner	ASU-6	As one Co., Ltd., Japan
8	Tabletop centrifuge	EX0800-A000	Kubota Co., Ltd., Japan
9	Glove box	Super(1220/75 0/900)	MIKROUNA Co., Ltd., China
10	Ohmmeter	FULL-TECH FT-101	FULL-TECH Co., Ltd., Japan
11	Digital meter	Keithley 2400	Teltronix, INC. Co., Ltd., USA
12	Solar simulator	CEP-2000	Bunkou Keiki Co., Ltd., Japan
13	Standard solar cell	BS-520BK	Bunkou Keiki Co., Ltd., Japan
14	Standard solar cell	BS-500BK	Bunkoukeiki Co., Ltd., Japan
15	Energy dispersive X-ray spectrometry	Genesis XM2	EDAX Co., Ltd., Japan

16	X-ray diffractometer	Rigaku	Rigaku Co., Ltd, Japan
17	Scanning electron microscope	JCM-6000	JEOL Co., Ltd, Japan
18	UV-visible spectrometer	V-670	JASSCO Co. Ltd., USA
19	ionization energy measuring device	KV205-HK	Bunkoukeiki Co., Ltd, Japan
20	X-ray photoelectron spectroscopy	AXIS-HS	KRATOS Co., Ltd., Japan
21	Tube Furnace	ARF-30KC	ASAHI RIKA Co., Ltd., Japan
22	Field emission- scanning electron microscope	S5200	Hitachi Co., Ltd., Japan

2.1.3 General methods of the hydrothermal synthesis.

Hydrothermal method is an effective way to synthesis materials that requires certain temperature and vapor pressure threshold [1]. This method can be dated back to 1840s. In most cases, a hydrothermal process can be defined as a method of synthesizing crystals at higher temperature and pressure, which has temperature and/or pressure dependent solubility, from an aqueous solution. The process is usually carried out in a Teflon-lined container, which is placed in a stainless steel pressure vessel called an autoclave to maintain the pressure. The system would be kept in an oven to maintain the temperature. Generally, the autoclave system would be heated to a target temperature and kept in steady state for a designed time, before undergoing a controlled cooling process. The product would be obtained during either the heating step or the cooling step. The advantages of the hydrothermal process include enabling the synthesis of the materials that are not obtainable without certain vapor pressure environment, enabling the synthesis of certain materials that are not stable near the melting point that is not suitable for solid state co-melting, and enabling the growth of fine-quality crystals while maintaining control over the composition.

On the other hand, disadvantages of the method include the need of expensive autoclaves, especially in industrial scale process, and the synthesis process cannot be observed or adjusted during the experiments. It is also to point out that synthesizing process with a solvent that is not aqueous would be referred as a solvo-thermal process, which can be demanded by certain specified experiments, but the overall concept is the same.

In our specified experiments, a hydrothermal process was carried out in a 6M hydroiodic acid (aq.) solution. The system was processed under a relatively mild temperature of 120°C. The steps can be illustrated in the flowchart below.

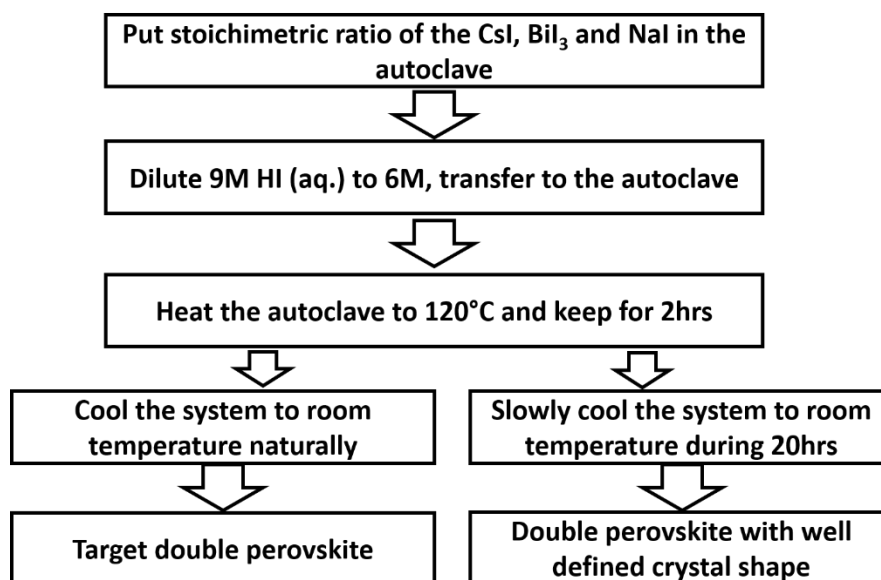


Fig. 1 Flowchart showing the hydrothermal process.

2.1.4 The preparation of the compact TiO₂ layer and the mesoporous TiO₂ layer precursor

The compact TiO₂ layer and the mesoporous TiO₂ layer are important electron transport materials for the perovskite solar cells. Solar cell devices discussed in this thesis employed such bi-layers as the electron transport materials. Below is the general process for preparing the compact TiO₂ and the mesoporous TiO₂ precursors.

The compact TiO₂ precursor was prepared via a sol-gel method [2]. With magnetic stirring, 68 mL of the titanium (IV) tetrabutoxide, and 16.5 mL of the 2,2'-iminodiethanol and 210 mL of

the super dehydrated ethanol were mixed for 1 hr. This solution was labeled as the Solution A. Then, 100 mL of the super dehydrate ethanol was diluted by 3.6 mL of the D.I. water and labeled as the Solution B. Under strong (> 1000 rpm) magnetic stirring, slowly add the Solution B into the Solution A, obtaining a clear white colloidal solution. The as-prepared solution was then stationed in a refrigerator ($8\text{ }^{\circ}\text{C}$) for 24 hr. before ready for use. The as-prepared compact TiO_2 layer precursor should be stored in the refrigerator in order to preserve its composition.

The mesoporous TiO_2 layer precursor was prepared from the TiO_2 paste purchased from the GreatCell Solar Ltd., without further purification. To be specific, the paste was transferred to a clean white plastic bottle and super dehydrate ethanol was added to the paste with a mass ratio of 1:3.5. Then ZrO_2 milling beads were loaded to the bottle. The plastic bottle with the mixture and the beads was transferred to a plastic ball-milling container, and milled for 4 hr. at 40 Hz. A homogenous suspension was obtained and ready for use. The as-prepared precursor should be kept in a sealed bottle and avoid direct sunlight radiation. Though it is not necessary, to store the precursor in the refrigerator is recommended, so that the precursor can maintain a steady state. The as-prepared precursor can be valid for at least 3 months before expire.

2.2 Characterization methods

2.2.1 X-ray diffraction crystallography (XRD)

The X-ray diffraction (XRD) crystallography is a non-destructive analytical technique that can obtain information on the unit cell dimension. During the XRD test, an incident X-ray beam is diffracted by the crystal lattice thus generating a collection of diffracted beams into different specific directions. Based on the Bragg's law, these diffracted beams can be described as followed:

$$2d \sin \theta = n\lambda \quad (2-1)$$

Where d is the spacing between the crystal planes, θ is the incident angle, n is an integer, and λ is the wavelength of the beam. The intensities and angles of these diffracted beams reveal the electron density map of the target sample, from which the in-depth information of the target

including the mean atom positions, the chemical bond details and lattice disorder, etc. By employing the XRD crystallography, researchers can identify the phases and analyze the molecular structures of crystalline samples.

The XRD patterns for the sample powders were obtained with an X-ray diffractometer (PANalytical X'Pert spectrometer) with Cu K α irradiation ($\lambda = 1.54056 \text{ \AA}$). The sample was prepared by depositing the powder to a clean and dry glass testing substrate before loading to the X-ray diffractometer. The XRD patterns were recorded by X'Pert highscore. The scan range is from 5° to 80° , and the scan rate is $5^\circ/\text{min}$.

2.2.2 Field emission scanning electron microscopy (FE-SEM)

Field emission scanning electron microscopy (FE-SEM) is a type of electron microscopy technique that produces images of samples by scanning the surfaces with a focused beam of electrons. The electron beam interacts with atoms of different depth, generating various signals providing topographical and compositional information. The FE-SEM can reach a magnification up to 300,000 times, with the virtually unlimited depth of field. Comparing to ordinary scanning electron microscopy (SEM), FE-SEM yield images with higher resolution and less distortion.

The FE-SEM images for the samples were taken by JEOL JSM-6701F, with a working voltage of 5 -10 kV and a working current of 15 μA . The sample powder was deposited to the conductive adhesive tape attached to the sample holder, carefully dusted with an air-duster, and then loaded to the vacuum chamber for observation.

2.2.3 X-ray photoelectron spectroscopy (XPS)

X-ray photoelectron spectroscopy (XPS) is a surface sensitive spectroscopic technique that can provide not only qualitative analysis but also quantitative analysis revealing various information of the target material including the elemental composition, empirical formula, chemical state, electronic state, etc. XPS equips a beam of X-ray to irradiate the target material, and record the number and the kinetic energy of the electrons escaping the surface of the target material. Since the energy of an X-ray with a particular wavelength, the kinetic energy of an emitted electron can be measured, the electron binding energy of each of the emitted electrons can be determined with the equation below:

$$E_{binding} = E_{photon} - (E_{kinetic} + \Phi) \quad (2-2)$$

Where $E_{binding}$ stands for the binding energy of a specific emitted electron, E_{photon} stands for the energy of the indicating X-ray photon, $E_{kinetic}$ stands for the kinetic energy of the electron measured, and Φ stands for the work function dependent on the spectrometer and the material. It is to be noted that XPS can provide high detective limit up to the parts per thousand range.

Since XPS would only detect the surface of the target material in a range of around 10 nm, it usually required the testing specimen to be processed in order to be fully expose. In this thesis, since the samples were in the form of powder, further grounding treatment was not necessary.

2.2.4 Ultraviolet photoelectron spectroscopy (UPS)

Ultraviolet photoelectron spectroscopy (UPS) is a characteristic method to detect the energy level distribution of a certain semiconductor material. By measuring and profiling the kinetic energy spectra of the photoelectrons emitted from the material, this method can easily illustrate the work function and the molecular orbital energies in the valence region. The overall principles of the UPS is quite similar to that of the XPS, difference being that in the UPS test, ionizing radiation of several tens of eV is employed, comparing to the ~1keV employed by the XPS. In the laboratory set up of the UPS, a gas discharge lamp is typically used to generate ultraviolet photons. Common gas used by the discharge lamp and their related properties are listed below.

Table 3. Properties of the gas used for the discharge lamp

Gas	Emission Line	Energy (eV)	Wavelength (nm)
H	Lyman α	10.20	121.57
He	1 α	21.22	58.43
Ne	1 α	16.85	73.62
Ar	1	11.62	106.70

Due to the lower incident photon energy, the emitting electrons would possess much lower kinetic energy, thus having a much shorter inelastic mean free path. Comparing to the XPS, UPS would have a much shallower information depth of on 2-2nm, but exhibit greater sensitivity.

As shown in the Fig.2 below, we can obtain the cutoff and onset energy of the kinetic energy profile of the emitting electrons, and follow the equations to determine the energy of the maximum valence band. Combine this piece of data with the bandgap data, one can sketch the band position chart of a potential light absorbing semiconductor, in order to find its matching electron transport material (ETM) and hole transport material (HTM).

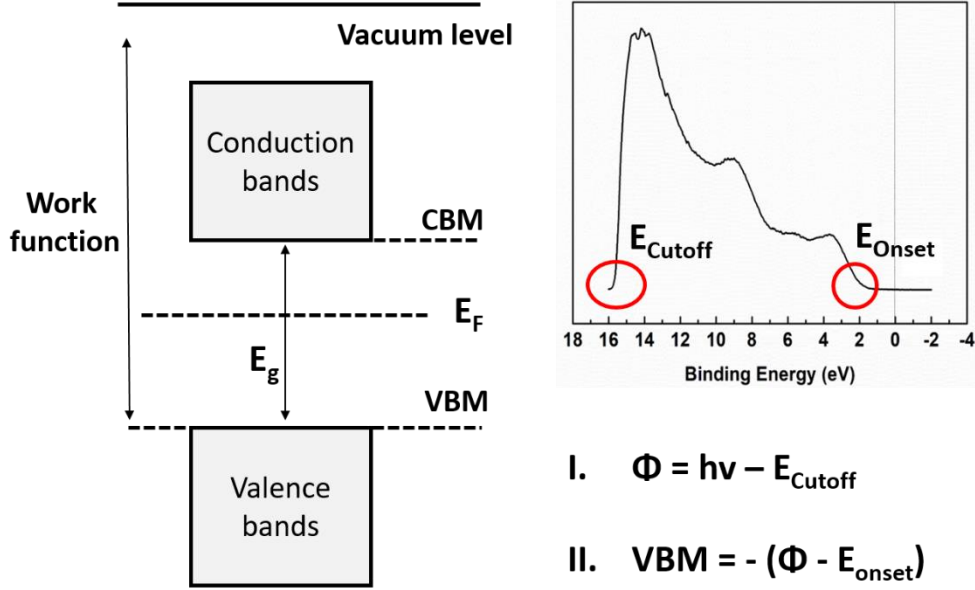


Fig. 2 Band position sketch and a typical UPS profile of a semiconductor. Equations show the steps for obtaining the VBM of the semiconductor.

2.2.5 Energy-dispersive X-ray spectroscopy (EDX)

EDX is a widely used analytical method for elemental composition detection of a sample. In most EDX test cases, a beam of charged particles (electrons, X-ray, etc.) were directed to the sample to excite its ground state electrons. The emission signals were captured to display as an emission spectrum, revealing the elemental composition and their relative abundance of the target sample.

EDX test was also used to examine the distribution of each element in the sample to determine the chemical state of the target material. With the elemental mapping images, we can

decide whether the target element or compound locate at the expected position, or to determine whether the sample is in a homogenous state.

EXD test can help researchers to reveal the relative abundance of each element in a sample. However, its accuracy is not as decisive as other test methods. The accuracy of the EDX test can be affected by many factors. The density, amount and the composition difference of the sample are all able to affect the fraction of the emission that passes through to the detector. In some cases, even the roughness of the sample surface can significantly hinder the emission signal. It is better we use caution when employing EDX as the quantitative analysis technique.

2.2.6 Ultraviolet-visible spectroscopy (UV-Vis)

The ultraviolet-vis spectroscopy is a routinely used quantitative measurement while evaluating the absorbance or transmittance of a certain material. By illuminating the sample in the form of solution or powder with a light beam whose wavelength sweeps in the ultraviolet and visible sections of the light spectrum, a profile of the absorbance with respect to the light wavelength can be obtained. Define absorbance (A) and transmittance (T) as followed:

$$T = I_t/I_0 \quad (2-3)$$

$$A = -\log_{10} T \quad (2-4)$$

Where I_t stands for the light transmitted by the sample and the I_0 stands for the light received by the sample. Based on the Beer-Lambert's Law [4]:

$$A = \sum_{i=1}^N \varepsilon_i \int_0^L c_i(z) dz \quad (2-5)$$

Where A stands for the absorbance of the testing sample, ε stands for the absorption coefficient, c stands for the concentration of the component i, and L stands for the path length of the incident light. Of course, in most testing cases, there will only be one solute in the solution, and the testing vessel is of uniform shape, thus the equation can be reduced as:

$$A = \varepsilon c L = \log_{10} \left(I_t/I_0 \right) \quad (2-6)$$

In the case of the photovoltaic material research, typically, we would want to evaluate the light absorbing ability of the material directly from the absorbance profile, and we would want to evaluate the bandgap of the material by constructing a Tauc plot [3]. Following the equation below, one can directly obtain the optical bandgap of a light absorber.

$$\epsilon h\nu = A(h\nu - E_g)^n \quad (2-7)$$

Where ϵ stands for the absorption coefficient, $h\nu$ stands for the incident photon energy and E_g stands for the bandgap of the sample. When measuring a material with a direct bandgap, $n = 2$, while measuring a material with an indirect bandgap, $n = 1/2$.

2.2.7 Photovoltaic performance measurement

The photovoltaic performance of the solar cells is mainly evaluated by the I - V curves measured by the solar simulator. In the I - V curves measurement of solar cells we focus on these parameters: the open circuit voltage (V_{oc}), the short circuit current (J_{sc}), the fill factor (FF), and the power conversion efficiency (PCE). I_{max} and V_{max} represent the current and the voltage at maximum output, respectively. The PCE and the FF can be defined as the followed:

$$PCE = (J_{sc} \times V_{oc} \times FF) / P \quad (2-8)$$

$$FF = (J_{max} \times V_{max}) / (J_{sc} \times V_{oc}) \quad (2-9)$$

Where P stands for the power of the incident light. In order to unify the testing results, a 100 mW/cm² incident light emitting from an Xeon light (named AM1.5G) is typically employed as the testing light source. In a general scenario, a sweeping voltage bias will be applied to the photovoltaic device in the range of -0.1V – 1V at a speed of 0.01V/s. A typical I - V profile obtained by this testing process is shown in Fig. 3.

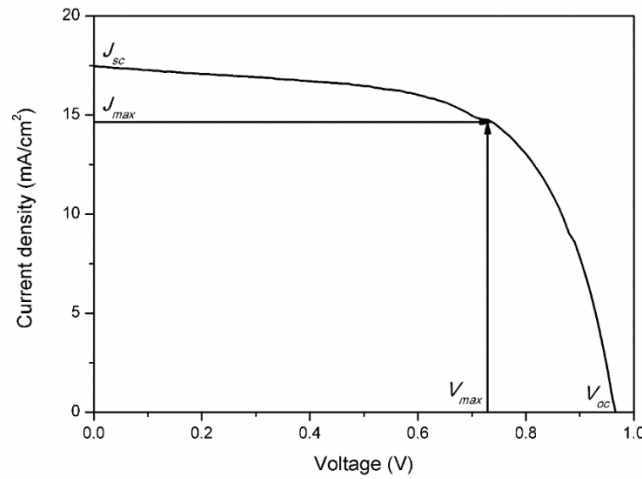


Fig.3 Sketch illustration of a typical I - V curve of solar cell

References

- [1] K. Byrappa K, Yoshimura M, Handbook of Hydrothermal Technology, New York, William Andrew Publishing, LLC., 2002.
- [2] Zhou H, Shi Y, Dong Q, Zhang H, Xing Y, Wang K, Du Y, and Ma T, Hole-conductor-free, metal-electrode-free $\text{TiO}_2/\text{CH}_3\text{NH}_3\text{PbI}_3$ heterojunction solar cells based on a low-temperature carbon electrode. J. Phys. Chem. Lett. 2014, **5**, 3241–3246.
- [3] Grigorovici T, Vancu A, Optical properties and electronic structure of amorphous germanium, Phys. Stat. Sol. B 1966, **15**, 627-637.
- [4] Houghton, J.T. The Physics of Atmospheres 2nd ed. 2002, Chapter 2.

Chapter 3. Development of a Mixed Halide-chalcogenide Bismuth-based Perovskite MABiI_2S with Small Bandgap and Wide Absorption Range

3.1 Introduction

Recently the lead-based halide perovskites have experienced a rapid development. The power conversion efficiency (PCE) of the lead halide-based perovskite solar cells has surprisingly increased to 23.3% [1]. No doubt that the lead-based halide perovskites are unique light absorbers, presenting amazing wide absorption range [2], long carrier diffusion length [3], high quantum conversion ratio [4], small direct bandgap, and good defect tolerance ability [5]. However, the lead-based perovskites also encountered major disadvantages such as the instability of the light absorber in humid environment and the toxicity of the Pb^{2+} generated by the irreversible decomposition. [6-7]. These disadvantages impeded the perovskite solar cell from progressing towards industrial fabrication and commercial deposition.

In order to overcome the disadvantages of the lead-based perovskites, a valid idea is to partially or fully replace the lead element with environmental friendly elements, such as tin, bismuth, germanium, copper, and alkaline-earth metals (Ba, Sr, Ca). However, not all the attempts were successful: Sn^{2+} and Cu^{2+} were proved similarly unstable and toxic compared to Pb^{2+} , while Ge^{2+} and the alkaline-earth metals form perovskites with large bandgaps that are not suitable for solar cells [8-12].

Among these substitute elements, bismuth is highly preferable owing to its low trap state densities, long carrier lifetime and proper defect tolerance ability [13-15] as predicted from computational scanning and experimental studies. More importantly, bismuth is much less toxic than lead [16]. Many studies on bismuth perovskites have been carried out, achieving exiting progression. However, major problems of the bismuth perovskites have been revealed as well. Bismuth halide perovskite would crystalize into a 2D hexagonal layered phase, which promotes intrinsic defect sites [17]. Another issue is that bismuth

perovskites tend to have large and indirect bandgap near 2.0 eV, which is not very suitable for perovskite solar cells [18].

While on the other hand, bismuth chalcogenides, such as Bi_2S_3 and Bi_2Se_3 , were reported to have smaller bandgap than that of the bismuth halide perovskites, and these materials are also stable and non-toxic [19-21]. It is reasonable to assume that the incorporation of the chalcogenide anions to the halide bismuth perovskites could reduce their bandgaps without affecting its optoelectronic properties. Another potential advantage of incorporating of the chalcogen anions is that the Bi-chalcogen bond is more covalent than the Bi-halogen bond, which resulted in higher overall covalence magnitude of the compound, thus brought forth to higher stability [22]. Evidently, computational predictions indicated that the mixed chalcogen-halogen perovskite existed in a steady form [23], which merited the photovoltaic development.

In this section, we successfully synthesized a highly crystallinity MABiI_2S (MBIS) lead-free mixed chalcogen-halogen perovskite via a two-step solid-state reaction process. We provided an in-depth analysis to elucidate the composition of MBIS powder via various methods. The MBIS possesses small bandgap with large absorption range. Based on these fine properties, we further explored the photovoltaic performances of the MBIS solar devices. We have successfully solved the non-fine quality of MBIS cannot form a film on TiO_2 substrates with an in-situ solid-state growth method. Although the devices achieved low PCE at this stage, several enhancement methods were carried out and further optimization routes were suggested.

3.2 Experimental section

3.2.1 Synthesis of the MBIS perovskite powder sample

In order to synthesize the target bismuth perovskite, we carried out a simple two-step solid-state reaction. To be specific, 0.5 mol bismuth sulfide (99%, Sigma-Aldrich) and 0.5 mol bismuth iodide (99.999% trace metal basis, Sigma-Aldrich) were put in an aluminum oxide mortar and grounded carefully, until the grounded mixture filtered through a 320-mesh stainless steel sieve. The as-prepared fine powder was transferred to an aluminum-foil-wrapped glass petri dish, and

then another stainless steel petri dish was covered on top of it. This system was transferred to the glovebox and annealed at 180 °C for 1 hr. After cooled to the room temperature, the as-synthesized intermediate product was collected and put to another aluminum oxide mortar and ground with 1.5 mol of MAI (98%, Wako). This mixture is also carefully grounded until it can filtered through the 320-mesh sieve. The as-prepared fine powder was put to another aluminum-foil-wrapped petri dish, and transferred to the glovebox. After annealed at 150 °C for 30 min and upon cooled, the product was collected in a transparent plastic sample vessel for further characterization. The synthesis procedure is described as shown in Fig.1.

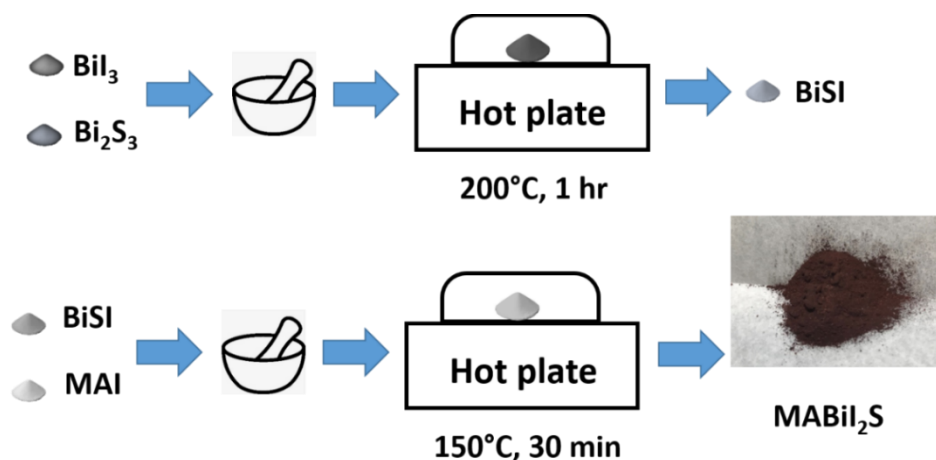


Fig.1 The solid-state synthesis procedure of the MBiS perovskite

It is notable that a slightly excess amount of Bi_2S_3 was used during the solid-state reaction to compensate the loss of small amount of sulfur.

3.2.2 Physical and optical characterization of the as-prepared MBiS perovskite

In order to elucidate the physical properties of the as-prepared MBiS perovskite, XRD (Rigaku XRD-DSC-XII) pattern was recorded; scanning from 5 ° to 80 ° (5 °/min) to determine the components of these products. The morphology of MBiS perovskite was recorded through SEM (JSM-6701). While, XPS (KRATOS AXIS-NOVA) and EDX (Hitachi S-3400N) tests were carried out to further confirm the composition of the product.

In order to evaluate the optical properties of the as-prepared MBIS perovskite, UV-Vis spectroscopy (Shimadzu UV-2550) test was carried out in order to obtain the absorption property of the sample and to calculate the optical bandgap.

3.2.3 Solar cell device fabrication and testing

Since the Bi_2S_3 is not soluble in DMF, DMSO, and GBL) facile spin-coating therefore is not the best coating technique to fabricate a conventional top-down structured solar cell device. To address this issue, a thin layer of Bi_2S_3 was first coated on top of the mesoporous TiO_2 scaffold layer via a chemical bath deposition (CBD) method, followed by performed an in-situ solid-state synthesis process to obtain from MBIS perovskite film on the substrate. Detailed fabrication procedures are described below.

To prepare the TiO_2 substrate, 70 μL TiO_2 compact layer precursor, as described in chapter two was spin coated on a clean FTO glass substrate (ultrasonic cleaned sequentially in detergent, D.I. water, acetone, IPA, and ethanol, each step for 15 min) at 3000 rpm for 30 s. The film was then sintered at 550 $^\circ\text{C}$ to form the TiO_2 compact ETL. 70 μL of the mesoporous TiO_2 precursor (described in chapter two) was then spin coated on the substrate at 5000 rpm for 30 s, and sintered at 450 $^\circ\text{C}$ to ensure the formation of mesoporous TiO_2 scaffold layer. After cooled to room temperature, the substrates were ready for use.

The experimental detail of synthesizing Bi_2S_3 through CBD is disclosed as follows: 0.02 mol of the $\text{Bi}(\text{NO}_3)_3$ and 0.02 mol of the $\text{Na}_2\text{S}_2\text{O}_3$ were dissolved in 25 mL D.I. water, respectively. The $\text{Bi}(\text{NO}_3)_3$ solution was first transferred to a flat-bottomed container, then 25 mL 0.2M EDTA solution in D.I water was added to the system. After magnetically stirred for 10 min, the $\text{Na}_2\text{S}_2\text{O}_3$ solution was added to the system. The solution turned pale yellow and certain amount of precipitates appeared at the bottom of the container. The PH of the solution was adjusted with NaOH solution until achieved PH=2. The substrates were dipped into the solution vertically, ensuring that the FTO electrode section was protected from the CBD solution. The CBD process lasted over 8 hrs at room temperature, and fine Bi_2S_3 films were obtained after the surface of the substrate was rinsed multiple times with acetone to remove any residue.

For solar cell fabrication, 80 μL 0.2 M BiI_3 solution was spin coated on the Bi_2S_3 coated substrates at 2000 rpm for 60 s. The obtained film was annealed at 180 $^\circ\text{C}$ for 5 min and then cooled to the room temperature. This deposition cycle was repeated for 15 times until a smooth

black film was formed. Then the substrate was annealed at 180 °C for 1 hr to allow the formation of BiIS intermediate film. Then the film was washed with DMF to remove the excessive amount of the BiI₃. After washed by acetone and dried in Ar gas environment, MAI powder was spread on the hotplate and the substrates were laid surrounding the MAI powder, and covered by a large petri dish to conduct vapor assistance annealing at 150 °C for 30 min. After cooled to room temperature, Spiro-OMeTAD or PCPDTBT was spin coated on the substrate as the hole transport material (HTM) at 2000 rpm for 1min. PEDOT:PSS (1 wt% D.I. water solution, diluted with methanol, V/V = 1/3) was applied on top of the HMT before 80 nm gold electrode was thermally deposited. The whole preparation and fabrication process is illustrated in Fig.2.

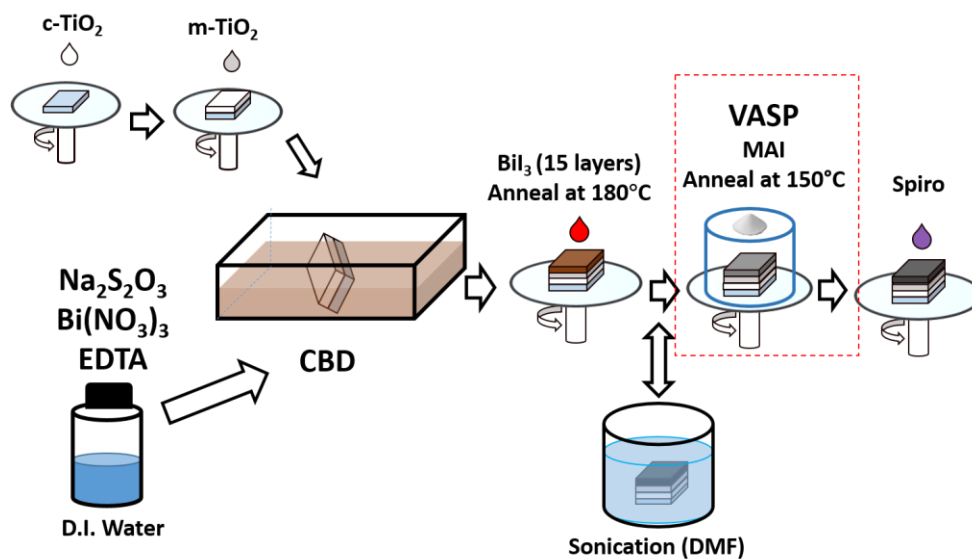


Fig.2 Sketch for the device fabrication process

The XRD pattern was taken for each fabrication step to ensure the composition of the film. The I-V curve of the solar cell devices was recorded via (Keithley 2450 SourceMeter) under 1 Sun AM 1.5G reference spectrum.

3.3 Results and discussion

3.3.1 Tolerance factor assessment

Since the MBIS perovskite is a new material without any presentation of previous report, we herein start our discussion with the calculation of the Gold-Schmidt tolerance factor (t) and the octahedral factor (μ) [24].

$$t = (r_A + r_X) / \sqrt{2}(r_B + r_X) \quad (3-1)$$

$$\mu = r_B / r_X \quad (3-2)$$

where r_A , r_B , and r_X stand for the ionic radii of the A site, B site and X site of an ABX_3 perovskite material, respectively. Corresponding ionic radii of all the ions are listed below

Table. 1 The ionic radii of the MABiI₂S perovskite [25]

	MA	Bi	S	I
Ionic radii	1.800	1.030	1.840	2.200
Coord.		VI	VI	VI

Theoretically, a halide perovskite recorded t and μ in the range of 0.81 to 1.11 and 0.44 to 0.90, respectively [26]. While experimentally and in accordance to the equations (1) and (2), the calculated t and μ recorded a value of 0.853 and 0.495, respectively, which is in great agreement with the literature.

In our case, $t < 0.9$ implies the MBIS perovskite would possibly prefer an orthorhombic or rhombohedral lattice instead of a cubic lattice. While the calculated μ indicates that the MBIS perovskite is hypothesized to be in 3D crystal structure.

3.3.2 SEM images of the as-prepared MBIS sample.

Fig. 1 shows the final product of the solid-state synthesized MBIS, which is a dark brown powder, while the intermediate product is a BiIS black powder. The chemical processes are described below.

After the first step solid-state synthesis, a distinct phase of BiIS was formed.



After the second step of the solid-state annealing, we can see that the characteristic peaks of the BiIS disappeared, while the target phase of MBIS appeared.



Fig 3. shows the SEM images of the MBIS perovskite, in which the MBIS perovskite grew in a fine 3D nanoparticles of ca. 50 nm.

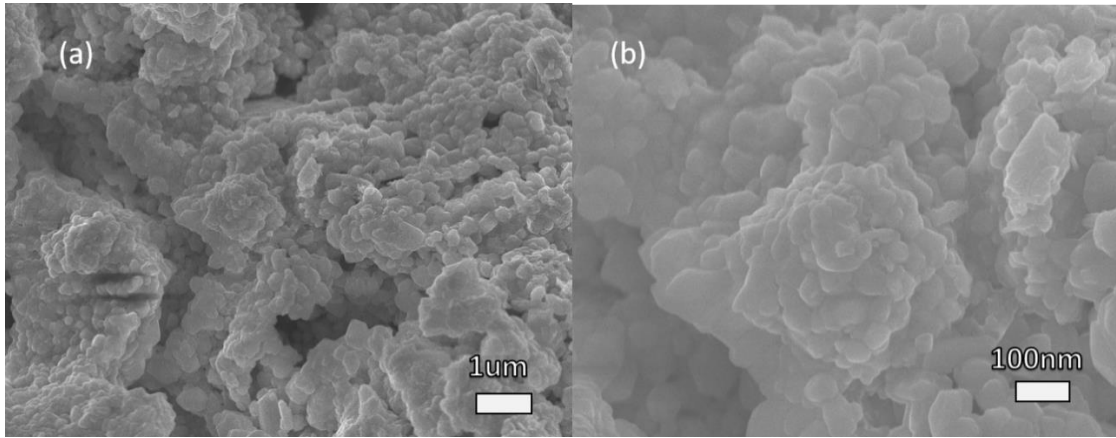


Fig. 3 SEM images of the MABiI₂S sample. (a) Image for the overall view of the powder sample. (b) Close look of the nanoparticles.

3.3.3 XRD analysis of the as-prepared sample

The composition of the as-prepared powder sample was determined through XRD. As MBIS is a newly synthesized material, there has no standard PDF card for the MBIS perovskite. We thus compared the XRD pattern of our sample to a simulation result of MASbI₂S [27]. Owing to the Sb and Bi elements are of the same family, the XRD pattern is predicted to be similar, with only a minute shift of certain peaks was observed from the XRD pattern. As shown in Fig. 4, all main peaks of the MBIS perovskite is consistent with the simulated pattern. Comparing the XRD patterns of our synthesized-MBIS against the reference MASbI₂S pattern [27], the XRD peaks located at 21.1 °, 25.0 °, 26.1 °, 30.5 °, 31.0 °, 34.2 °, 35.1 °, 36.9 °, and 37.8 ° were shifted to

higher 2θ value by about 0.8° due to the replacement of larger Bi atom over the Sb. It is notable that the crystal plane distance is inversely proportional to the diffraction angle, in which peak shifting takes place when a smaller Sb atom is replaced by a larger bismuth atom. However, minute trace of impurity phase, Bi_2S_3 is also found to be presence (marked as red stars) within the perovskite material owing to incomplete conversion of the Bi_2S_3 during the solid-state reaction.

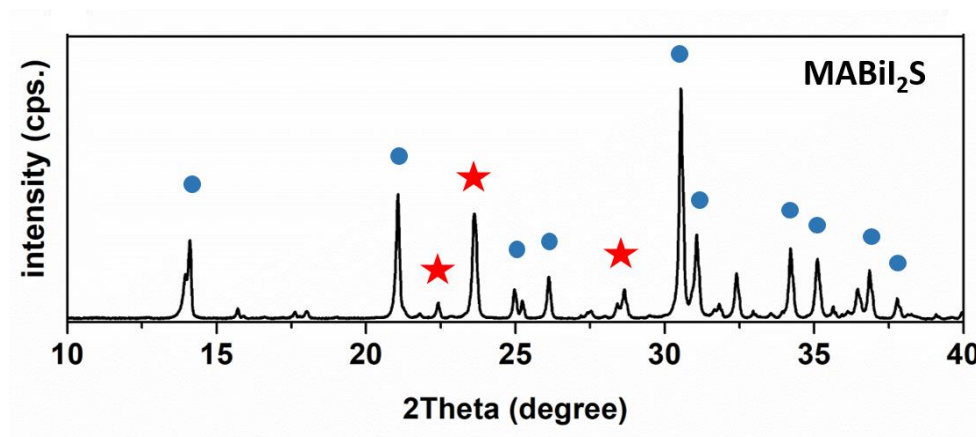


Fig. 4 XRD pattern of the MBiS perovskite, where the main phase is marked by the blue dots, while peaks of an impurity, Bi_2S_3 , is marked by the red stars.

3.3.4 EDX profile and the elemental mapping

To further confirm the composition of our sample, EDX detecting and elemental mapping were performed, as shown in Fig. 5. The presence of all expected elements are revealed from the EDX spectrum (Fig. 5 (a)), where strong bismuth and iodine signals are observed, indicative of the higher proportion of bismuth and iodine over the other elements. From the elemental atomic percentage yielded from the EDX pattern, we can determine that the atomic ratio of the bismuth, sulfur and iodine elements are approximately 1:1:5. This ratio implies sulfur loss during the solid-state reaction process. Our observation is also agrees with this conclusion, where a small amount of yellow solid, which was proven to be sulfur, was collected from the lid of the solid-state reaction container. However, we should aware that the EDX elemental ratio is only a qualitative estimation, thus it is still necessary to determine the actual formula of our material with additional precise means.

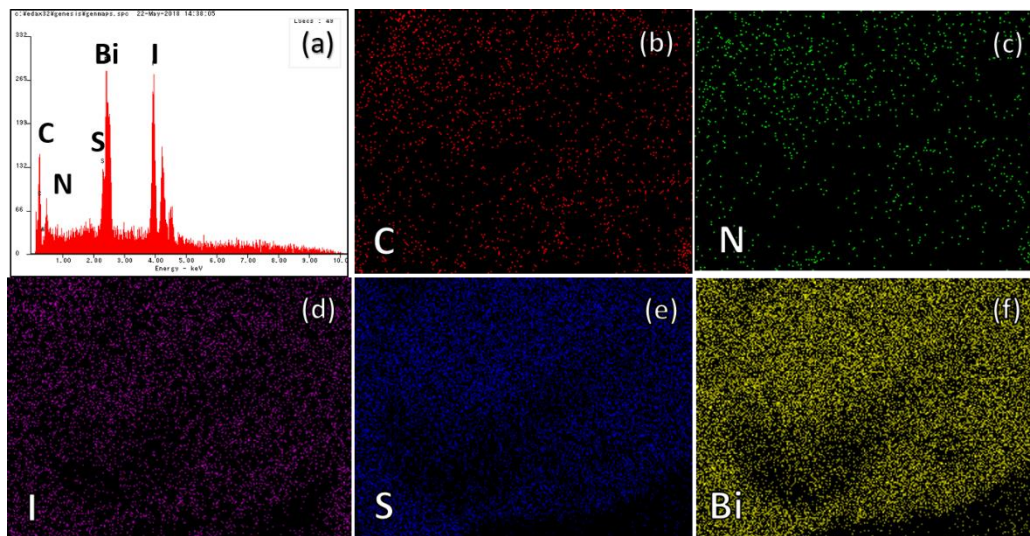


Fig. 5 (a) The EDX pattern and (b)-(f) the elemental mapping images of the MBIS perovskite. Each element is marked on the corresponding mapping image.

Fig. 5 (b)-(f) show the elemental mapping images of the as-prepared MBIS sample and the corresponding elements were marked on their mapping images. It is observable that all the elements are distributed evenly in the mapping area, indicating that the sample was in a homogenous state. We inferred that since the sulfur element does not aggregate and it follows the distribution pattern of other elements, the amount of Bi_2S_3 impurities presence in this sample is insignificant.

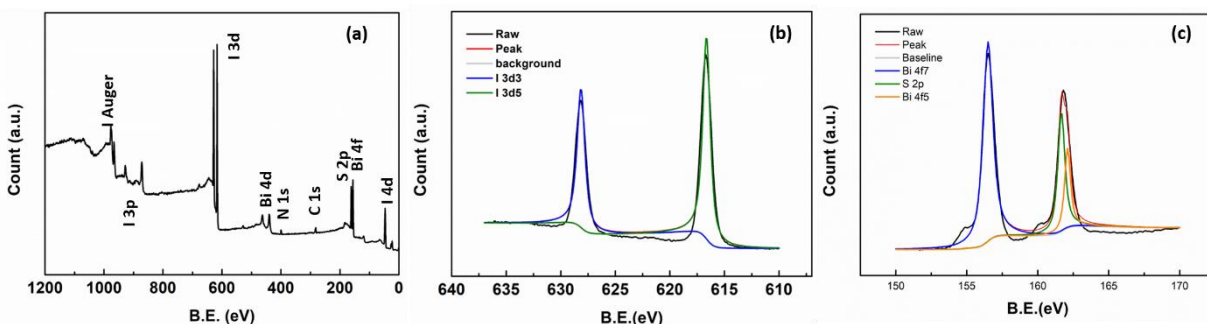


Fig. 6 (a) The full range survey XPS spectrum of the MBIS perovskite and (b) narrow scan of Bi 4f orbital and S 2p orbital, and (c) I 3d orbital. All the peaks and the corresponding orbital for the component elements were marked out.

3.3.5 XPS analysis

The chemical states of each element in the MBIS perovskite are elucidated through the XPS profile. As shown in Fig.6, the wide scan of the as-prepared MBIS perovskite has thus proven the presence of all the expected elements of the MBIS perovskite and all the dominant binding orbitals of each element were revealed. By identifying the dominating orbitals from the spectrum and inspect the narrow scan of Bi, S and I, we are able to decide the valence of each element, where Bi is 3^+ , S is 2^- and I is 1^- . The narrow scan of the I 3d spectrum in Fig.6 (b) exhibited two distinct I 3d $_{3/2}$ and I 3d $_{5/2}$ deconvoluted peaks, which were located at 617.0 eV and 629.0 eV. The narrow scan of the Bi 4f spectrum in Fig.6 (c) exhibited two deconvoluted peaks as well, which were Bi 4f $_{5/2}$ and Bi 4f $_{7/2}$ peaks situated at 156.5 eV and 161.5 eV. While Fig.6 (c) depicted the S 2p peak located at 163.5 eV, which is attributed to the metal-sulfur bond of 2^- valence. The peak of 0 valent sulfur element did not appear, suggesting that no residue sulfur is remained after the entire solid-state reaction process. This also supported our conclusion that the sulfur has been incorporated into the bismuth perovskite and the MBIS is successfully synthesized.

3.3.6 UV-vis absorption spectrum and the Tauc' plot

In order to evaluate the light absorption ability of the MBIS, we recorded its UV-Vis spectra. Fig.7 (a) shows the UV-Vis absorption spectrum of the MBIS powder sample. From this figure, we can see that the MBIS perovskite started to show optical absorption from 350 nm, and has a strong absorption intensity in the range of 350 – 700 nm. Its absorption edge extended to 750 nm while still maintain a half of the maximum absorption intensity. We can conclude that the MBIS perovskite shows very promising light absorbing potential, showing high absorption and large absorbing range in the visible light range that is comparable to the Pb-based perovskites. It is worth noting that the MBIS perovskite showed proper absorbing ability in the infrared region of the solar spectrum, extending its absorption range up to over 1000 nm. The special absorption range would not only be beneficial to the single-junction solar cell application, but also be beneficial to the multi-junction device application.

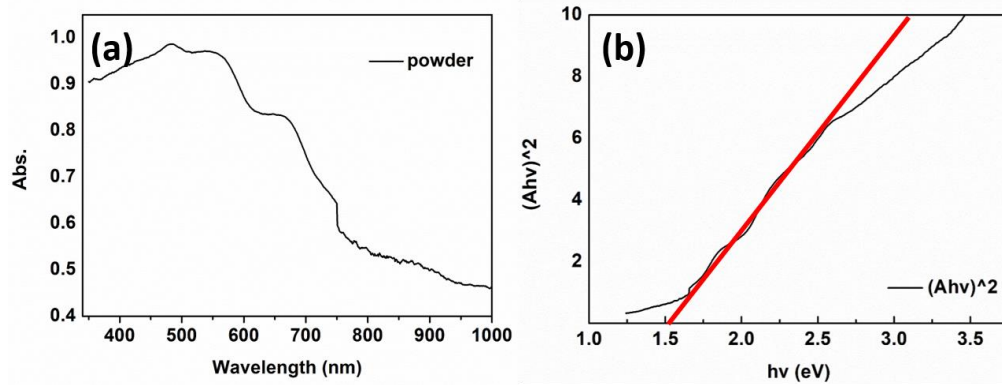


Fig. 8 (a) UV-Vis powder absorption spectrum of the MBIS perovskite showing an absorption range reaching 1000 nm. (b) The Tauc' plot derived from the UV-Vis absorption spectrum of the MBIS.

From the UV-Vis absorption spectrum, we can constructed the Tauc' plot following the relation below, and estimated the bandgap of the MBIS perovskite.

$$\epsilon h\nu = A(h\nu - E_g)^n \quad (2-5)$$

where ϵ stands for the absorption coefficient, $h\nu$ stands for the incident photon energy and E_g stands for the bandgap of the sample. When measuring a material with a direct bandgap, $n = 2$, while measuring a material with an indirect bandgap, $n = 1/2$.

If we consider the indirect bandgap situation and let $n = 1/2$, the corresponding Tauc's plot yields no valid bandgap; thus we assumed the MBIS has a direct bandgap. Fig.7 (b) shows the Tauc' plot of the MBIS perovskite derived from the UV-Vis absorption spectrum. By extrapolation, an optical bandgap of $E_g = 1.52$ eV was obtained, which is close to the MAPbI₃; thus implies MBIS is a very promising perovskite material for the photovoltaic devices. Judging by the optical properties above, we can confidently apply this new perovskite material for solar cell application.

3.3.7 Device fabrication and characterization

In order to assess the potential of the MBIS perovskite towards photovoltaic application, solar cell devices were fabricated. Considering our as-prepared powder sample contained certain amount of Bi₂S₃ impurity and this impurity is not soluble in typical organic solvent used in

perovskite solar cell fabrication, one viable idea is to simply dissolve the sample in aprotic polar solvent, and remove the impurity with filtering. If the thin film can be properly formed, then the device can be assembled with simple step-by-step spin coating.

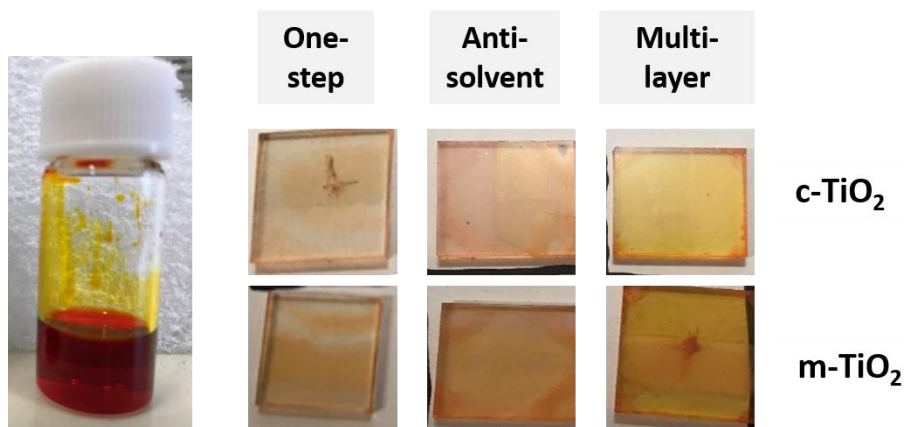


Fig.8 The filtered solution of MBIS in DMF and the films of MBSI on c-TiO₂ and m-TiO₂ substrate. The substrate and spin-coating method used by each film are marked out.

Four solutions of the MBIS perovskite dissolved in Ethanol, IPA, Chlorobenzene and DMF were prepared. When dissolved in solvents with low polarity, the solutions showed significant lamination phenomenon. It is also worth noting that ethanol and IPA would damage the solute, forming unknown solid with green color, which is most possibly organic bismuth compound [28]. It is obvious that we should choose DMF as the solvent. After filtering, the DMF solution appeared to be a clear dark red solution as shown in Fig.8 (a). Films fabricated on FTO substrate with and without mesoporous scaffold layer were shown in Fig.8 (b). These films are thin and highly transparent, which are obviously not suitable for perovskite solar cells. We have tried to increase the concentration of the precursor solution, to slow down the spin coating speed, or to fabricate multi-layered films, aiming at achieving thicker MBIS film. However, neither of these routes could fulfil our goal. As expected, the cells fabricated with these highly transparent films yielded no PCE. Apparently, the spin-casting method became not valid here.

In order to solve the film formation problem, we introduced an in-situ growth process combining a CBD deposition of the Bi₂S₃ nanoparticles [29] and a sequential spin coating of the

BiI_3 film, and eventually an MAI vapor assisted in-situ solid-state annealing growth to get the target MBIS perovskite film, as illustrated in the Fig.2 and described in the experimental section. Through this process, dark brown MBIS films can be fabricated and the top-down structure perovskite solar cells can be assembled.

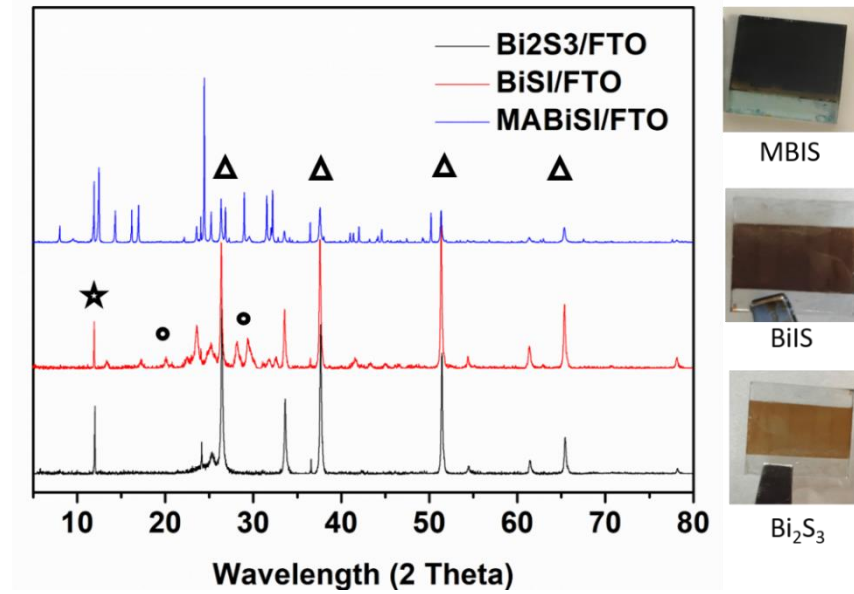


Fig.9 Layer by layer XRD pattern of the in-situ growth films for the MBIS devices. In the figure, each film was labeled. The black star represent the characterization peak of the Bi_2S_3 , the black dots represent the BiI_3 , and the triangles represent the peaks of the FTO substrate. Meanwhile the photos right side showed the actual image of each layer, as marked out.

To verify the composition of the in-situ growth film, layer-by-layer XRD patterns were recorded in Fig 9. We observed that the initial CBD film showed a fine pattern of Bi_2S_3 nanoparticles. It is also noticed that in both steps the Bi_2S_3 characteristic peaks showed strong intensity. This is due to the special texture of the testing film that would exposed the Bi_2S_3 film at the region where reaction did not take place. However, it also indicated that beneath the BiI_3 and MBIS films, the residual Bi_2S_3 nanoparticles existed. Bi_2S_3 was reported to possess a narrow bandgap and its bandgap can be significantly affected by the morphology and particle size [30]. However, it was also demonstrated that the Bi_2S_3 can display high conductivity [31]. In our devices, it is very plausible that these nanoparticles can be potential defect sites that cause leakage.

To test the performance of the MBIS perovskite solar cells, we assemble the devices whose structure can be described as [FTO/c-TiO₂/m-TiO₂/MBIS/PCPDTBT/Au]. Initially the as-prepared devices show low PCE of 0.03%. Surely, we should enhance the device. Starting from the top layer of the device, we found that the gold electrode was not as compact as we expected. It is reasonable to predict that the surface of the MBIS would not be as smooth as that of the lead-based perovskite, thus a surface treatment agent should be introduced. By applying PEDOT:PSS as the surface treatment agent, we observed that the gold electrode became smoother and much more compact, as shown by the inset photos of the devices with and without the PEDOT:PSS treatment. The J_{SC} of the device increased significantly, from 0.40 mA.cm⁻² to 1.03 mA.cm⁻². Another method we employed is to apply dynamic spin coating with the BiI₃ layers, which further enhanced the quality of the MBIS layer and increased the J_{SC} to over 2.0 mA.cm⁻², with an increased FF from 0.25 to 0.30.

Another issue is the HTM. The PCPDTBT was chosen due to it can form fine-quality film on rougher surfaces. However, the device utilizing the PCPDTBT only yield $V_{OC} = 0.1$ V. From Figure 7 (b) we can see that the band mismatch of the PCPDTBT is much more severe than the Spiro-OMeTAD, resulting in significant V_{OC} loss.

On the other hand, the Spiro-OMeTAD form poor film on top of the MBIS. Also, the water-based surface passivation agent PEDOT:PSS will damage the Spiro-OMeTAD, reducing its hole extraction ability. Applying the Spiro-OMeTAD as the HTM would resulting in a significant increase of V_{OC} from 0.1 V to 0.22 V, but the J_{SC} was simultaneously decreased from 2.2 mA.cm⁻² to 1.96mA.cm⁻². Table 2 below summarized the champion performances of the devices before and after enhancements.

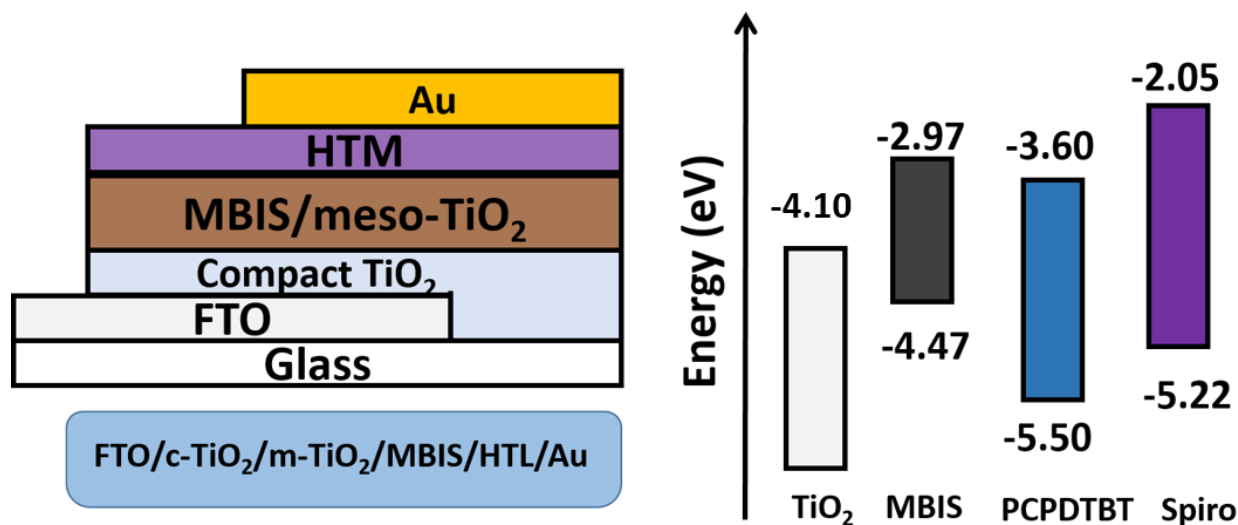


Fig.7 (a) Sketch of the devices structure and (b) The band positions of the device.

Table. 2 Device performance before and after enhancements.

	PCE	VOC	JSC	FF
Before	0.13	0.22	1.96	0.30
After	0.01	0.10	0.43	0.25

Another interesting phenomenon to point out is that when we intentionally fabricate the device based a damaged mesoporous TiO₂ scaffold (showed in Fig.12), the reduction of the I-V performance is surprisingly small. As listed in the table below, the defected cell displayed small reduction of each parameter compared to the well-fabricated control cell. This indicated that the MBIS perovskite possesses high defect tolerance ability, which can be extremely important considering the real-life scenario of the perovskite solar cell applications. Here silver electrode was used simply for saving the gold, since the quality of the electrode would not affect the conclusion.

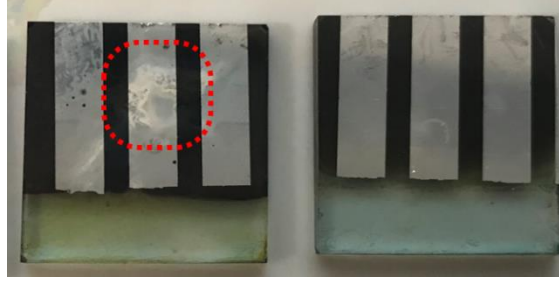


Fig.12 Cell fabricated with damaged m-TiO₂ layer (left) and fine m-TiO₂ layer (right). The red circle marked a area with significant damage due to the collapse of the scaffold.

Table 2. The I-V performances comparison between a chosen damaged cell and a normal cell

	V _{OC}	J _{SC}	FF	PCE
Defected cell	0.04	1.97	0.28	0.02
Control cell	0.05	2.41	0.29	0.03

It was also noticed that the mesoporous TiO₂ film with CBD Bi₂S₃ layer on top was damaged much faster than a plane m-TiO₂ film, even when stored in the glovebox, which indicates that the CBD process would be harmful to the m-TiO₂ scaffold, since the CBD process were carried out in water-based system and normally at acidic environment. The damage to the TiO₂ scaffold can also be an important reason that the V_{OC} loss is large. Alternative CBD method that can deposit Bi₂S₃ film without the help of m-TiO₂ layer or without water/acid could greatly enhance the device performance.

3.4 Conclusions

In summary, we have successfully synthesized a mixed chalcogen-halogen lead-free perovskite MBIS via a simple two-step solid-state synthesis. Based on the UV-Vis absorption, we determined that the MBIS perovskite has a bandgap of 1.52 eV, and it possesses a wide absorption range that extends to over 1000 nm. The unique properties of this material meet the criterion for the photovoltaic application. By employing an in-situ growth technique, we have successfully solved the film quality issue of the MBIS where the treated MBIS device showed PCE enhancement over the untreated device due to the poor perovskite film formation on the TiO₂

substrate. Several enhancement route were suggested and the PCE of the device were increased from 0.06% to 0.13%. In addition, this material displayed high defect tolerance ability. The special properties of the MBIS perovskite show that it can be a viable light absorber with refined device fabrication techniques.

References

- [1]. Yang Y, You J, Lei M, inventors. The Regents of the University of California (Oakland, CA, US), assignee. Efficient and Stable Perovskite Solar Cells with All Solution Processed Metal Oxide Transporting Layers. United States Patent 0033983. 2018-02-01.
- [2]. Lee M. Teuscher J. Miyasaka T. Murakami T. Snaith H. Efficient Hybrid Solar Cells Based on Meso-Superstructured Organometal Halide Perovskites. *Science*. 2012 Nov 02;338(6107):643-647.
- [3]. Dong Q. Fang Y. Shao Y. Mulligan P. Qiu J. Cao L. et al. Electron-Hole Diffusion Lengths > 175 μm in Solution-Grown $\text{CH}_3\text{NH}_3\text{PbI}_3$ Single Crystals. *Science*. 2105 Feb 27;347(6225):967-970.
- [4]. Yang B. Dyck O. Poplawsky J. Keum J. Puretzky A. Das S. et al. Perovskite Solar Cells with Near 100% Internal Quantum Efficiency Based on Large Single Crystalline Grains and Vertical Bulk Heterojunctions. *J Am Chem Soc*. 2015 Jul 9;137(29):9210–9213.
- [5]. Brandt R. Stevanovic V. Ginlev D. Buonassisi T. Identifying Defect-Tolerant Semiconductors with High Minority Carrier Lifetimes: Beyond Hybrid Lead Halide Perovskites. *MRS Commun*. 2015;5:265–275.
- [6]. Berhe T. Su W. Chen C. Pan C. Cheng J. Chen H. et al. Organometal Halide Perovskite Solar Cells: Degradation and Stability. *Energy Environ Sci*. 2015 Oct 20;9:323-356.
- [7]. Feng J. Xiao B. Effective Masses and Electronic and Optical Properties of Nontoxic MASnX_3 (X = Cl, Br, and I) Perovskite Structures as Solar Cell Absorber: A Theoretical Study Using HSE06. *J Phys Chem C*. 2014 Aug 6;118(34):19655-19660.
- [8]. Noel N. Stranks S. Abate A. Wehrenfennig C. Guarnera S. Haghighirad A. et al. Lead-Free Organic–Inorganic Tin Halide Perovskites for Photovoltaic Applications. *Energy Environ Sci*. 2014 May 01;7:3061-3068.
- [9]. Park B. Philippe B. Zhang X. Rensmo H. Boschloo G. Johansson E. Bismuth Based Hybrid Perovskites $\text{A}_3\text{Bi}_2\text{I}_9$ (A: Methylammonium or Cesium) for Solar Cell Application. *Adv Mater*. 2015 Sep 29;27(43):6806-6813.
- [10]. Krishnamoorthy T. Ding H. Yan C. Leong W. Baikie T. Zhang Z. et al. Lead-Free Germanium Iodide Perovskite Materials for Photovoltaic Applications. *J Mater Chem A*. 2015 Oct 16;3:23829-23832.
- [11]. Cui X. Jiang K. Huang J. Zhang Q. Su M. Yang L. et al. Cupric Bromide Hybrid Perovskite Heterojunction Solar Cells. *Synthetic Metals*. 2015;209:247-250.
- [12]. Pazoki M. Jacobsson T. Hagfeldt A. Boschloo G. Edvinsson T. Effect of Metal Cation Replacement on the Electronic Structure of Metalorganic Halide Perovskites: Replacement of Lead with Alkaline-Earth Metals. *Physical Review B*. 2016 Apr 07;93:144105.

- [13]. Zhou H. Chen Q. Li G. Luo S. Song T. Duan H. et al. Interface engineering of highly efficient perovskite solar cells. *Science*. 2014 Aug 01;345(6196):542-546.
- [14]. Johansson MB. Zhu H. Johansson EMJ. Extended Photo-Conversion Spectrum in Low-Toxic Bismuth Halide Perovskite Solar Cells, *J Phys Chem Lett*. 2016;7(17):3467-3471.
- [15]. Hoyer RLZ. Brandt RE. Osherov A. Stevanovic V. Stranks SD. Wilson MWB. et al. Methylammonium Bismuth Iodide as a Lead-Free, Stable Hybrid Organic-Inorganic Solar Absorber. *Chem Eur J*. 2016 Feb 18;22(8):2605-2610.
- [16]. Hebig J, Kuhn I, Flohre J, Kirchartz, T. Optoelectronic Properties of $(\text{CH}_3\text{NH}_3)_3\text{Sb}_2\text{I}_9$ Thin Films for Photovoltaic Applications. *ACS Energy Lett*. 2016 Jun 21;1(1):309-314.
- [17]. Eckhardt K, Bon V, Getzschmann J, Grothe J, Wisser FM, Kaskel S. Crystallographic insights into $(\text{CH}_3\text{NH}_3)_3(\text{Bi}_2\text{I}_9)$: a new lead-free hybrid organic-inorganic material as a potential absorber for photovoltaics. *Chem Commun*. 2016 Jan 19;52:3058-3060.
- [18]. Murugan V. Ohta T. Iikubo S. Kapil G. Ripolles TS. Ogomi Y. Ma T. Pandey SS. Shen Q. Toyoda T. Yoshino T. Minemoto T. Hayase S. Facile Synthesis and Characterization of Sulfur Doped Low Bandgap Bismuth Based Perovskites by Soluble Precursor Route. *Chem Mater*. 2016;28(18):6436-6440.
- [19]. Chang JA, Rhee JH, Im SH, Lee YH, Kim HJ, Seok SI, et al. High-performance nanostructured inorganic-organic heterojunction solar cells. *Nano Lett*. 2010 Jul 14;10(7):2609-12.
- [20]. Choi YC, Lee DU, Noh JH, Kim EK, Seok SI. Highly Improved Sb_2S_3 Sensitized-Inorganic-Organic Heterojunction Solar Cells and Quantification of Traps by Deep-Level Transient Spectroscopy. *Adv Funct Mater*. 2014 Mar 03;24(23):3587-3592.
- [21]. Martinez L, Bernechea M, Garcia deArquer FP, Konstantatos G. Near IR-Sensitive, Non-toxic, Polymer/Nanocrystal Solar Cells Employing Bi_2S_3 as the Electron Acceptor. *Adv Ener Mater*. 2011 Sep 19;1(6):1029-1035.
- [22]. Hong F, Saparov B, Meng W, Xiao Z, Mitzi DB, Yang Y. Viability of Lead-Free Perovskites with Mixed Chalcogen and Halogen Anions for Photovoltaic Applications. *J Phys Chem C*. 2016, Mar 9;120(12):6435-6441.
- [23]. Goldschmidt V. M. Die Gesetze der Krystallochemie. *Naturwissenschaften*. 1926. 14:477.
- [24]. Shannon R, Revised Effective Ionic Radii and Systematic Studies of Interatomic Distances in Halides and Chalcogenides. *Acta Cryst*. 1976, A32:751-767.
- [25]. Li C, Lu X, Ding W, et al. Formability of ABX_3 ($\text{X} = \text{F}, \text{Cl}, \text{Br}, \text{I}$) halide perovskites. *Acta Crystallogr B*. 2008 Nov 14;64(6):702-707.
- [26]. Nie R, Mehta A, Park B, Kwon HW, Im J, Seok SI. Mixed Sulfur and Iodide-Based Lead-Free Perovskite Solar Cells. *J Am Chem Soc*. 2018 Jan 4;140(3):872-875.
- [27]. Ng C. Lim H. Hayase S. Zainal Z. Shafie S. Huang N. Effects of Temperature on Electrochemical Properties of Bismuth Oxide/Manganese Oxide Pseudocapacitor. *Ind Eng Chem Res*. 2018 Jan 23;57(6):2146-2154.
- [28]. Dessy R, Kitching W. Organometallic Electrochemistry. III. Organometallic Anions - Derived from Group V Elements. *J Am Chem Soc*. 1966 Feb;88(3):467-470.

- [29]. Moreno-Garcia H, Nair MTS, Nair PK. Chemically Deposited Lead Sulfide and Bismuth Sulfide Thin Films and Bi₂S₃/PbS Solar Cells. *Thin Solid Films*. 2011. 519(7):2287-2295.
- [30]. Bernechea M, Cao Y, Konstantatos G. Size and Bandgap Tunability in Bi₂S₃ Colloidal Nanocrystals and Its Effect in Solution Processed Solar Cells. *J Mater Chem A*. 2015 Aug 31;3:20642-20648.
- [31]. Liufu SC, Chen LD, Yao Q, Wang CF. Bismuth Sulfide Thin Films with Low Resistivity on Self-Assembled Monolayers. *J Phys Chem B*. 2006 Nov 3;110(47):24054-24061.

Chapter 4. Design of a Novel and Highly Stable Lead-Free Double Perovskite $\text{Cs}_2\text{NaBiI}_6$ for Photovoltaic Application

4.1 Introduction

In the previous chapter, we have discussed that the bismuth-based perovskites can be one promising substitute of the lead-based perovskites, owing to its advantages of lower intrinsic trap densities, lesser defect states, long carrier lifetime, and its defect-tolerate properties merit the progression of lead-free photovoltaic [1]. However, the bismuth-based perovskites have their own shortcomings. Generally, bismuth perovskite without modification would have large bandgap, which would impede its absorbing ability, cause a direct reduce of the photocurrent. On the other hand, the crystal shape structure of the bismuth-based perovskite would usually be of 2D hexagonal morphology, thus the film of the bismuth-based perovskite would naturally have more intrinsic defect sites that will act as the recombination centre [2].

As an alternative pathway to assess the disadvantage of the lead-based perovskites, engineering double perovskite material by replacing the divalent Pb^{2+} ions with a monovalent B^+ and a trivalent B^{3+} ions, in the form of $\text{A}_2\text{B}^+\text{B}^{3+}\text{X}_6$ (also denoted as an “elpasolite”) double perovskite structure is a fine way towards synthesizing a stable and environmental benign perovskite [3]. To date, the most discussed double perovskite combination is the Ag and Bi elements for the B sites. Xiao et al. have conducted a complex and detailed computational analysis on the thermodynamic stability, electronic structure and defect properties of the $\text{Cs}_2\text{AgBiBr}_6$ compound. They pointed out that the $\text{Cs}_2\text{AgBiBr}_6$ is less stable than the $\text{CH}_3\text{NH}_3\text{PbBr}_3$ material owing to the coupling between Bi 6s and Br 6p orbitals in $\text{Cs}_2\text{AgBiBr}_6$ is weak [4]. In addition, it is revealed that the $\text{Cs}_2\text{AgBiX}_6$ has a corner-shared octahedral framework, which is similar to that of the Pb-perovskite. Although this material exhibited excellent long PL decay time (indicates long carrier lifetime), the calculations and experimental data showed that $\text{Cs}_2\text{AgBiX}_6$ has a large

indirect bandgap of over 2 eV [5-9]. Cheng et al. also reported that a 2D hexagonal $\text{MA}_2\text{AgBiI}_6$ crystal possesses wide bandgap of 1.96 eV, which disfavours its application in photovoltaic devices [10]. Apart from Ag/Bi double perovskites, many other B site cations were also studied. Volonakis et al. reported a $\text{Cs}_2\text{InAgCl}_6$ double perovskite in 2017 [11]. First-principle calculations predicted that the $\text{Cs}_2\text{InAgCl}_6$ has a direct bandgap, which is an advantage for photovoltaic applications. Nevertheless, the bandgap of this material is still very large (approaching 3 eV). Another double perovskite $\text{MA}_2\text{KBiCl}_6$ also exhibited large bandgap of 3.04 eV despite its similar crystal structure as the Pb-based perovskites [11-12]. Notably, double perovskite materials listed above and reported elsewhere generally showed high stability that can reduce environmental impact.

The major disadvantage of the reported double perovskites is that their bandgaps are all large for use in single-junction solar cells. Hence, designation of a low bandgap double perovskite halide is in great need where the new double perovskite should have a proper bandgap with wide absorption range across the solar spectra, and it should maintain the advantages of the double perovskites such as stable and non-toxic.

We here present our work on successful synthesis of a high crystallinity, stable, and novel $\text{Cs}_2\text{NaBiI}_6$ (CNBI) lead-free double perovskite via one-step facile hydrothermal process. The CNBI double perovskite exhibited tolerance and octahedral factors of 0.849 and 0.466, respectively (Supplementary Information). In this manuscript, we provided an in-depth study on the CNBI crystal growth process under the influence of various acid concentrations and its plausible crystal growing mechanism. Our synthesized CNBI double perovskite possesses bandgap of 1.66 eV, excellent stability, and good light absorption performances, which fulfilling the criterion for photovoltaic application. Worth to be mentioned, the CNBI double perovskite material is first to be synthesized and materialized for lab-scale solar cell application with an efficiency of 0.42%, which is comparable to other lead-free perovskite solar cells.

4.2 Experimental section

4.2.1 Synthesis of the target compound

In order to synthesize the CNBI double perovskite, we carried out a simple one-step hydrothermal process. To be specific, 9M hydroiodic acid (47 wt% in water, stored in refrigerator, Sigma-Aldrich) was diluted to 6M, then caesium iodide (99.999% trace metals basis, Sigma-Aldrich), sodium iodide (99.999% trace metals basis, Sigma-Aldrich) and bismuth iodide (99.999% trace metals basis, Sigma-Aldrich) were dissolved in 12mL of this 6M hydroiodic acid with a stoichiometric molar ratio to form an orange dispersion. After 10 min of magnetic stirring, the magnetic stirrer was removed and the solution was transferred to a Teflon-lined autoclave for further processing.

To carry out the hydrothermal process, the autoclave was loaded to the stainless steel container and put in an oven to heat at 120°C for 2 hrs, and then slowly cooled to room temperature in 12 hrs to obtain sand-like, dark cerise crystals of the CNBI perovskite. The as-synthesized crystals were washed with D.I. water and centrifuged for multiple times until the supernatant is colourless, then dried in a vacuum chamber to obtain the final product. The product was collected and transferred to a transparent plastic sample vessel for further characterization. The overall synthesis process can be expressed by the flowchart below.

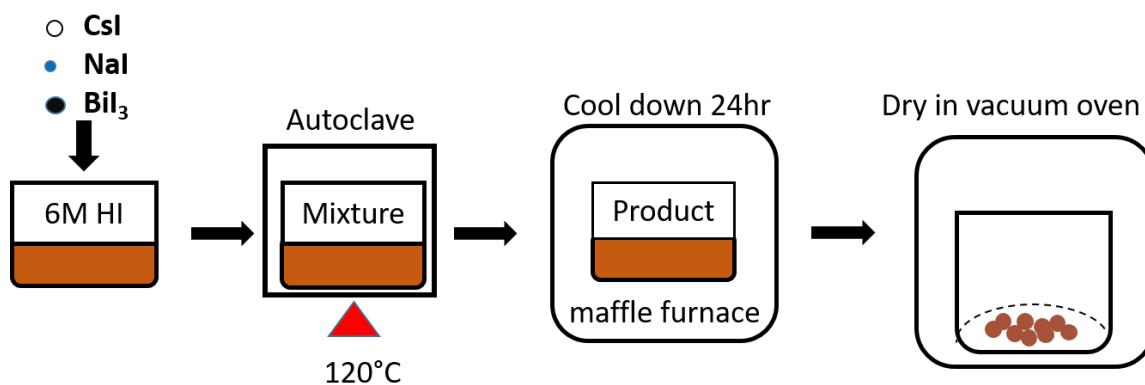


Fig. 1 The hydrothermal synthesis process of the CNBI perovskite sample.

4.2.2 Characterization of the CNBI

In order to elucidate the physical properties of the as-prepared CNBI double perovskite, XRD (Rigaku XRD-DSC-XII) test was carried out in the range of 5° to 80° ($5^{\circ}/\text{min}$) to determine the components of the product. We also took FE-SEM (Hitachi F-5200) images to observe its crystal morphology for a better understanding of its microstructure. XPS (ThermoFisher ESCALAB™ 250Xi) test was also carried out to further confirm the composition of the sample.

In order to evaluate the optical properties of the as-prepared CNBI perovskite, the UV-vis absorption spectra (Shimadzu UV-2550) were measured in order to observe the absorption property of the sample and to calculate its bandgap. VBM determination test were carried out to find the band positions of the CNBI perovskite so that we can understand its optical properties better, and to find suitable ETM and HTM for solar cell application.

4.2.3 Fabrication and testing of the devices

In order to evaluate the photovoltaic performance of the CNBI, top-down perovskite solar cell devices were fabricated by a one-step spin coating method. It should be pointed out that usually the one-step spin coating method requires no mesoporous TiO_2 layer. However, in our case, the meso-layer-free type would cause significant difficulty for the double perovskite layer to form. Therefore, in our experiment, we prepared our substrate with both compact and mesoporous TiO_2 layers.

Before fabrication process, we cleaned the FTO substrates with sequential supersonic washing with detergent, D.I. water, acetone, iso-propanol and ethanol. The compact TiO_2 film was prepared with 70 μL of the compact TiO_2 layer precursor (described in chapter two) spin coated on the FTO substrate at 3000 rpm for 30 s. This film was sintered at 550°C , and cooled to the room temperature for the mesoporous TiO_2 film deposition. The mesoporous TiO_2 scaffold film was prepared by spin coating 70 μL of the TiO_2 mesoporous layer precursor (as described in chapter two) on the substrates at 5000 rpm for 30 s. This film was then sintered at 450°C and cooled to the room temperature for later use.

To fabricate the CNBI light absorber layer, 2 mole CsI, 1 mole NaI and 1 mole BiI_3 were dissolved in DMF with stoichiometric molar ratio. The solution was magnetically stirred for 2 hr and filtered to form a clear dark cerise solution. Then the as-prepared solution was spin coated to the substrates at 1500 rpm for 20 s obtain the double perovskite layer. Subsequently, the spin-

coated film was quickly transferred to a hotplate for drying and then annealed at 120 °C for 1 hr to fully evaporate the residual solvent. The spiro-OMeTAD was applied onto the double perovskite layer as the HTM by spin coating at 3500 rpm for 20 s. 100 nm gold electrode was deposited on the surface of the devices by thermal deposition as the back electrode. The complete fabrication process is illustrated in the Fig. 2 below.

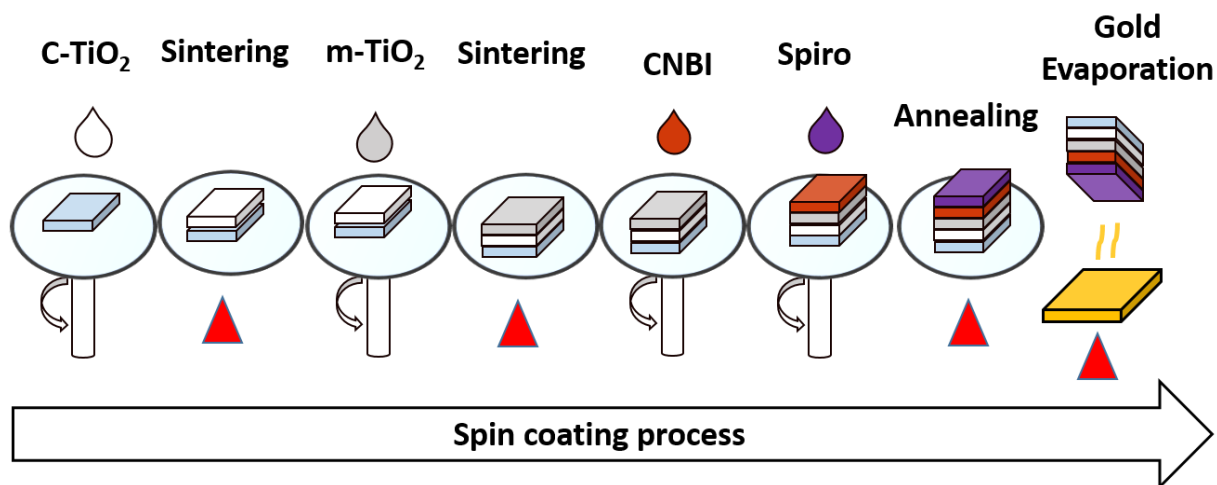


Fig.2 The fabrication process of the top-down perovskite solar cell with CNBI as the absorber.

To assess the performance of the solar cells, I-V curves were recorded (Keithley 2450 SourceMeter) with respect to 1 Sun AM 1.5G reference spectrum to evaluate the performance of the device. The IPCE of a champion cell was recorded using a monochromatic Xenon lamp (Bunkouki CEP-2000SRR). We have also showed the stability of the CNBI solar cells by comparing the I-V performance of a device when it was freshly fabricated and when it was stored for 14 days.

4.3 Results and discussion

4.3.1 Tolerance factor calculation

As we have described in chapter three, the tolerance factor (t) and the octahedral factor (μ) are important parameters to predict whether a perovskite material can have stable 3D structure [13].

$$t = (r_A + r_X)/\sqrt{2}(r_B + r_X) \quad (4-1)$$

$$\mu = r_B/r_X \quad (4-2)$$

In our current study, since a double perovskite has two cations at the B₁ and B₂ sites, it is a reasonable simplification to calculate r_B as the combination of both cations, assuming they both take up 50% atomic abundance.

$$r_B = (r_{B1}/r_{B2})/2 \quad (4-3)$$

The corresponding parameters are listed below in Table.1.

Table. 1 The ionic radii of the CNBI perovskite.

	Cs	Bi	S	I
Ionic radii	1.670	1.030	1.840	2.200
Coord.	VI	VI	VI	VI

Following the equations, we can calculate both factors, as shown in Table.2.

Table 2. Calculated tolerance and octahedral factors of CNBI as compared to MAPbI₃.

Photo-Active Material	Tolerance factor (t)	Octahedral factor (μ)
CNBI	0.849	0.466
MAPbI ₃	0.83	0.54

. The factors obtained show that CNBI has similar tolerance factor as the MAPbI₃, hypothesizing that our synthesized CNBI is in octahedral structure. While the smaller μ of CNBI indicates crystal lattice instability. However, we should notice that the calculated t and μ factors are just predictions, while the actual crystal shape and stability were to be assured through practical experiments.

4.3.2 XRD analysis

In order to determine the composition of the as-prepared powder sample, we have taken XRD patterns for this sample. As a newly synthesized material, no standard PDF card for the CNBI perovskite exists. We compared the XRD pattern of our sample to a similar material, $\text{MA}_2\text{AgBiI}_6$ [21]. By replacing Ag with Na and MA with Cs, we should expect slight shift of the peaks in the XRD pattern, as well as certain new diffraction peaks.

Here, Fig. 3 shows the XRD pattern of the as-prepared CNBI sample, while Fig. 4 shows the reference pattern, which we compared with. It is clear that the two patterns show similar peak distributions. The CNBI double perovskite peaks 2θ values are observed at 12.8° , 24.3° , 25.1° , 25.8° , 27.3° , 29.7° , 32.3° , 42.3° , and 45.9° . Meticulously, the 2θ peaks at 27.3° , 29.7° , 32.3° , 42.3° and 45.9° slightly shifted towards higher 2θ values as compared to the $\text{MA}_2\text{AgBiI}_6$ reference peaks, which is due to the smaller lattice spacing caused by replacing Ag^+ ion (ionic radius 1.02\AA) with Na^+ ion (ionic radius 1.15\AA) [14]. The replacement of Na^+ ion over the Ag^+ ions shifted the XRD peaks towards higher diffraction angle range. Additionally, from the data obtained from XRD analysis, CNBI can assume a hexagonal crystal with symmetric space group of $\text{P63}/\text{mmc}$, as in agreement with the reference material.

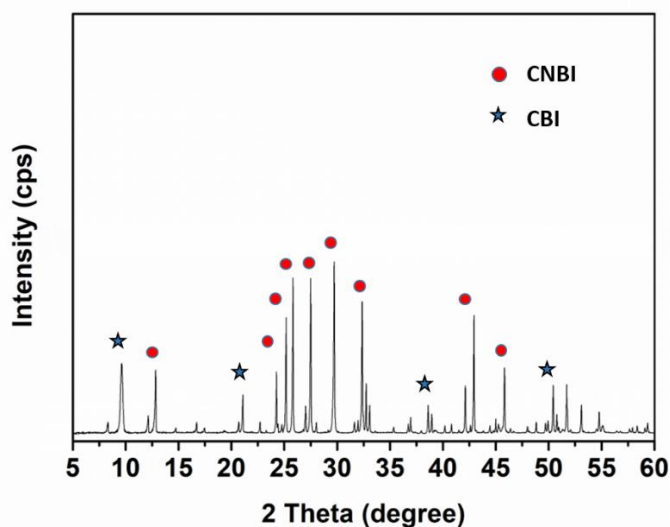


Fig.3 The XRD pattern of the as-prepared CNBI sample. The main phase is the CNBI double perovskite, marked by the red dots; and the secondary phase is the $\text{Cs}_3\text{Bi}_2\text{I}_9$ perovskite marked by the blue stars.

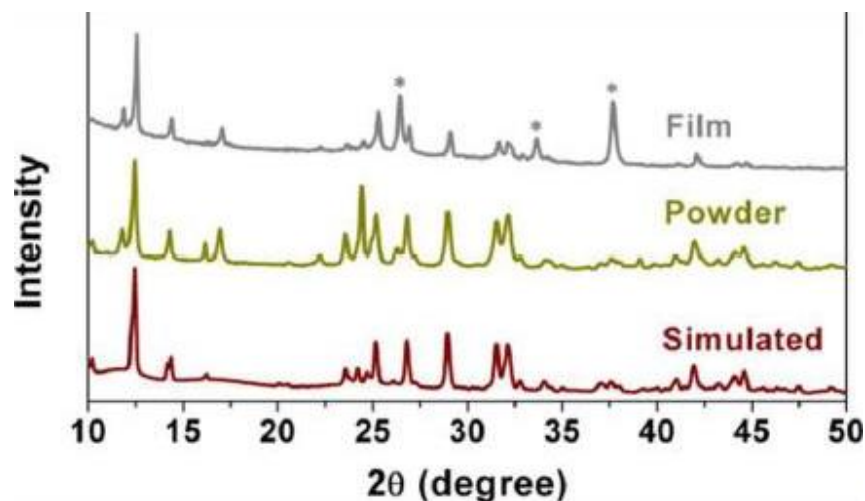


Fig. 4 The reference XRD pattern, $\text{MA}_2\text{AgBiI}_6$.

4.3.3 SEM images of the CNBI and the chemical process

During the synthesis experiments, we found that the hydroiodic acid plays an important role in promoting the formation of the CNBI. SEM images in Fig.5 showed that when synthesized with and without hydroiodic acid, the product shows distinctly different crystal structure. In combination of the XRD conclusions, it is reasonable to assume the 3D crystals in Fig.5 (a) represent the CNBI crystals, and the 2D hexagonal platelets in Fig.5 (b) represent the secondary phase, $\text{Cs}_3\text{Bi}_2\text{I}_9$. It is clear that when the hydroiodic acid was introduced to the synthesis process, the product would be dominant by CNBI, while when the hydroiodic acid is not introduced, the product would be dominant by the side product $\text{Cs}_3\text{Bi}_2\text{I}_9$. This evidence showed that increasing acid concentration would suppress the decomposition and promote the product of the target CNBI compound.

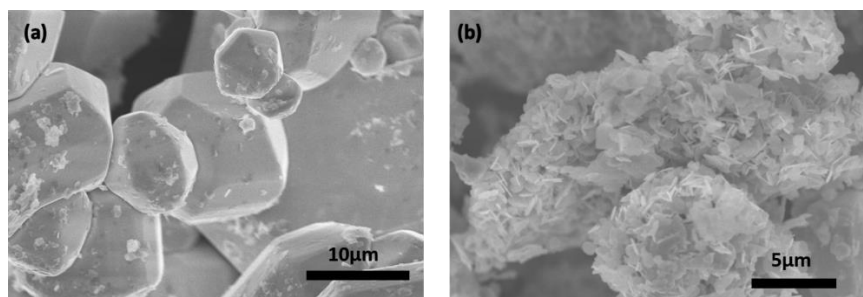
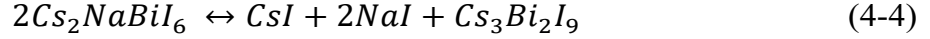


Fig. 5 SEM images of the (a) CNBI crystals when synthesized with hydroiodic acid, and (b) clusters of hexagonal nano-platelets representing $\text{Cs}_3\text{Bi}_2\text{I}_9$.

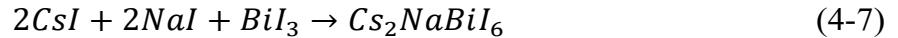
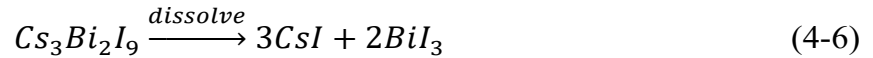
Now that we understand the importance of the hydroiodic acid, we can hypothesize the chemical reaction route during the hydrothermal process. During the hydrothermal procedure, when the temperature drops, CNBI would undergoes a partial decomposition route generating CBI.



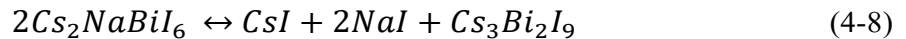
For further clarification, the overall chemical process will be describing as below: Initially, the generation of the CBI is favoured at lower temperature.



As the temperature raises, the CBI is completely dissolved in the acidic solution. At higher temperature, with the assistance of the hydroiodic acid, CNBI is precipitated.



After a certain temperature threshold, the CNBI started to decompose and the decomposition process would continue until it reached an equilibrium state. Assuming that the CNBI was fully decomposed, the produced CsI and NaI would be eliminated during the post treatment process. Here we hypothesized that partial decomposition process would occur instead of a full decomposition. It is reasonable to assume that the decomposition process will cease upon reaching an equilibrium state.



Based on the equation above, according to Le Chatelier's principle, the equilibrium reaction is more likely favouring the formation of CNBI with higher iodide anion concentration, and this agrees with our pervious observation that when the hydroiodic acid was introduced to the system, the formation of CNBI would dominant.

4.3.4 XPS spectra analysis

Fig.6 illustrated the full range XPS survey spectrum of the CNBI. This spectrum explicitly revealed the presence of all CNBI elements (Na, Bi, Cs, and I) with a binding energy in the range

of ~1000 eV to 150 eV. The binding energy of the spectra was adjusted with the carbon reference, which shows the 1s orbital peak at 282.2 eV, giving the charge correction factor $\Delta=2.6$ eV.

Fig.7 shows the narrow ranged scan of each elements of the CNBI. Especially, the Na 1s (Fig.7 (a)) orbital exhibited a significant peak at 1070 eV, which indicates the existence of both ionic sodium and sodium oxide. On the other hand, the Na_{KL1} auger peak located at 497 eV suggests the presence of only ionic sodium. It is known that for the ionic sodium, its 1s orbital and auger peak would always simultaneously appear in the XPS spectra [15]. Herein, the two deconvoluted Na 1s peaks certainly assures the formation of Na¹⁺ ion in the as-prepared sample.

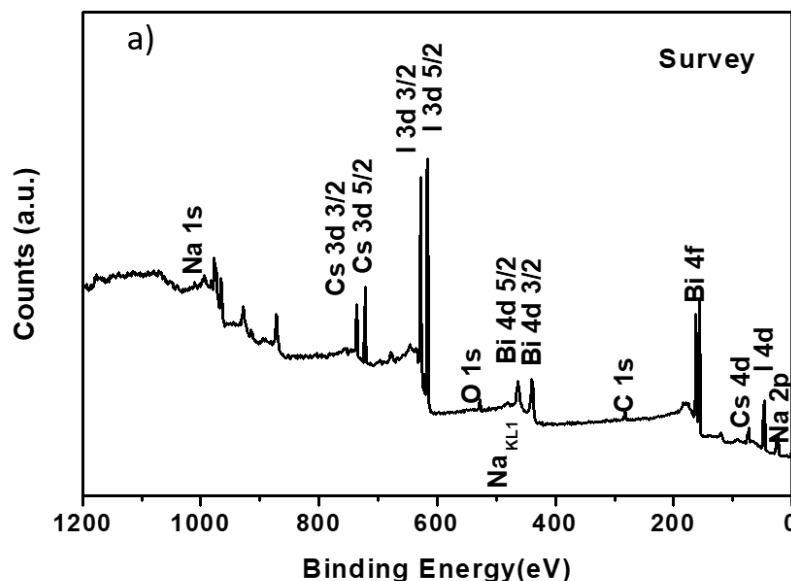


Fig.6 The full range XPS survey spectrum of the CNBI

The narrow scan of the Bi 4f spectrum (Fig.7 (b)) exhibited two deconvoluted peaks, which were Bi 4f_{5/2} and Bi 4f_{7/2} peaks situated at 158 eV and 164 eV. The binding energy difference of ~5.3 eV proved the presence of Bi element in an oxidation state of 3+ [26]. Additionally, Cs 3d (Fig.7 (c)) possesses binding energy of 723 eV (Cs 3d_{3/2}) and 736 eV (Cs 3d_{5/2}), whilst I 3d (Fig.7 (d)) shows two strong deconvoluted peaks at binding energies of 617 eV and 629 eV, representing I 3d_{3/2} and I 3d_{5/2}, respectively. Each of the spectra shows well-separated spin-orbit

peak components with standard binding energy differences. These peaks imply the formation of the Cs, Bi and I ions with the dominant valences of 1^+ , 3^+ and 1^- , respectively, thereby proof the formation of the CNBI perovskite material.

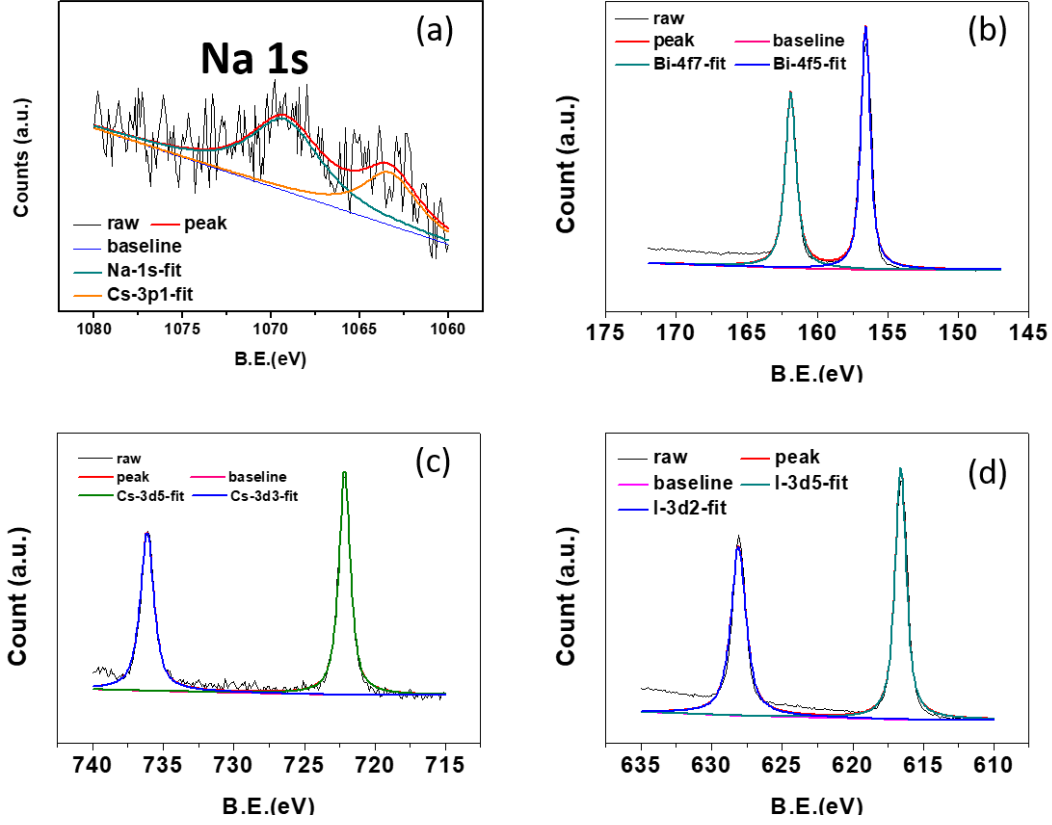


Fig. 7 XPS narrow scan spectra: (b) Na 1s, (c) Bi 4f, (d) Cs 3d, and (e) I 3d

By calculating the integrated peak areas of the XPS spectra, we can roughly estimate the molar ratio of the elements using the equation below:

$$\text{Molar ratio} = \frac{\text{Integrated Peak Area}}{\text{RSF}} \quad (4-9)$$

where RSF stands for the relative sensitivity factor. Based on this equation, the Na : Bi possesses a molar ratio of 1 : 4.9. Corroborating to the decomposition process mentioned above,

we can assume that about 2/3 CNBI decomposed into the CBI during the cooling process. This also indicated that our chemical hypothesis is viable.

4.3.5 UV-vis absorption spectra analysis and the optical bandgap calculation.

To investigate the optical absorbing ability of the CNBI, we carried out UV-vis absorption measurement of the CNBI powder sample. Fig.8 (a) shows the absorption curve of the CNBI powder. The CNBI powder displayed excellent light absorption intensity between 300 nm and 600 nm, showing the absorption edge at 650 nm. On the other hand, it is obvious that the CNBI double perovskite shows stronger absorption below 350 nm, where the lead-based perovskite usually started to show decrease in the absorption [27]. The absorption below 350 nm suggested that CNBI can help harvest extra energy from the ultraviolet region to enhance the photo current conversion.

The Tauc plot of the CNBI is constructed as shown in Fig.8 (b). From it, we estimated the bandgap of the CNBI material to be 1.66 eV. Such narrow bandgap is rare with respect to the double perovskite materials. We can conclude that the CNBI is suitable for photovoltaic devices in accordance to the Shockley-Queisser limit theory [28].

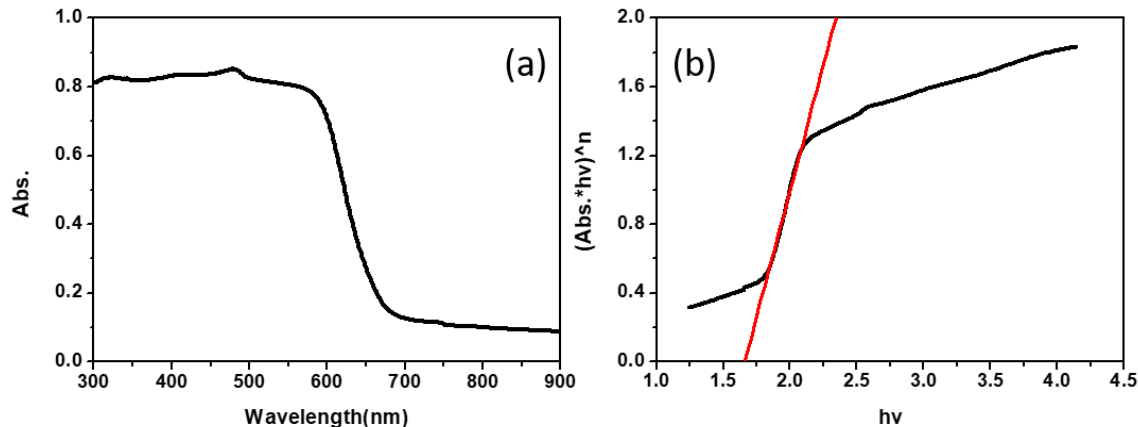


Fig. 8 (a) UV-vis absorption spectrum and the (b) Tauc' plot of the CNBI perovskite.

4.3.6 Stability assessment of the CNBI powder sample.

Obtaining a perovskite material that is highly stable and resistive towards outdoor stringent conditions is primarily important for practical photovoltaic application and commercialization. Prior to solar cell fabrication, we also investigated the stability performance of our synthesized

CNBI double perovskite material under ambient condition. To be specific, we stored the sample in a colourless transparent vessel in ambient air for 5 months. From the XRD profile in Fig.9, we observed that the XRD patterns of both the fresh and non-fresh (after 5 months) CNBI double perovskite are highly similar, showing no occurrence of new peaks and no sign of further degradation. Note that the secondary phase CBI does not hinder the stability of the sample, due to CBI itself is also a relatively stable material. The intensity of the CNBI characteristic peaks does not significantly decrease, implying the sample maintained its good crystallinity. In addition, the width of the CNBI characteristic peaks does not increase; suggesting that the particle size of the as-prepared sample does not undergoes significant change. Overall, we can conclude that the as-prepared sample possesses excellent stability in ambient air showing negligible degradation after 5 months of storage, and is highly resistance towards moisture despite the CNBI sample was stored at high humidity of 70% from March to August.

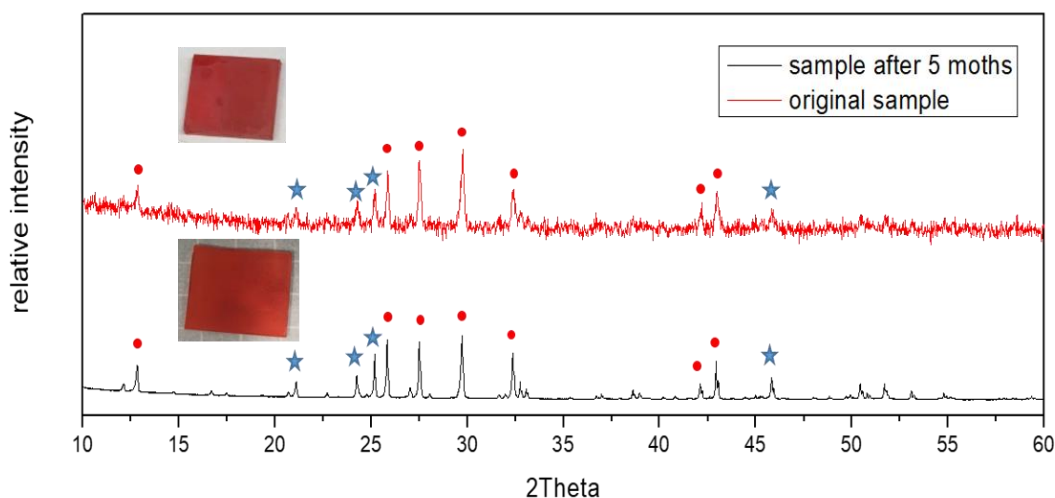


Fig.9 Comparison of the XRD patterns of a same sample when it was freshly prepared (the red one) and when it was stored for 5 months (the black one).

4.3.7 Device fabrication and characterization

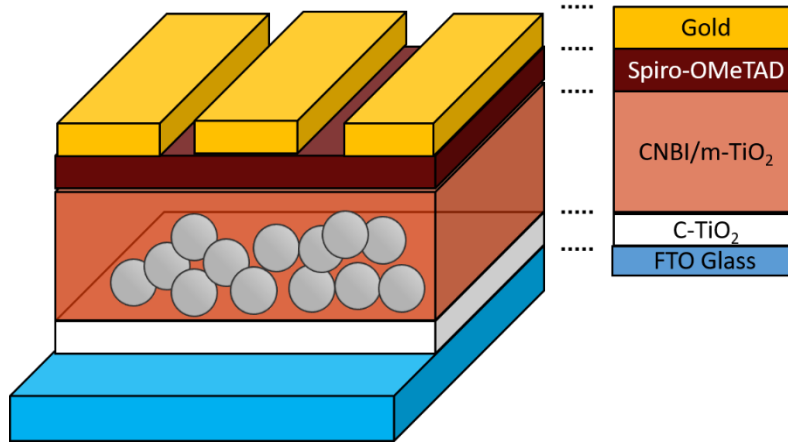


Fig.10 Structure sketch of the perovskite solar cell fabricated with the CNBI.

In order to evaluate the photovoltaic performance of the CNBI, solar cells employing CNBI as the light absorber were fabricated under ambient condition. We have equipped TiO₂ as the ETL and Spiro-OMeTAD as the HTL Fig.10 demonstrated the structure of the device we fabricated. Fig.11 shows the J-V performance of the CNBI double perovskite solar cell showing the champion PCE. Table 3 listed the performance of the CNBI solar cell as well as other lead-free perovskite solar cells. By testing and collecting data of a batch of 30 devices we obtained the V_{OC} of 0.45 ± 0.02 V, FF of 0.40 ± 0.04 , and J_{SC} of 1.80 ± 0.20 mA.cm⁻². Fig.12 shows the histogram of the PCE distribution. We can see the PCEs range from 0.27% - 0.42%. Overall, we can conclude that the CNBI is of high potential in replacing the unstable and toxic lead-based perovskites.

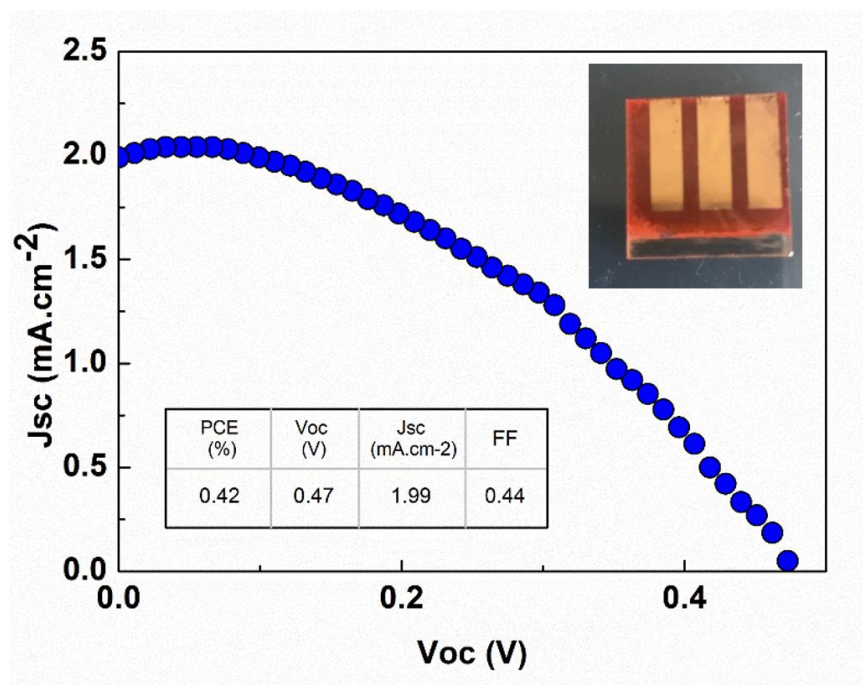


Fig.11 I-V curve of the device that yielded champion PCE. The inserted picture shows the as-fabricated device.

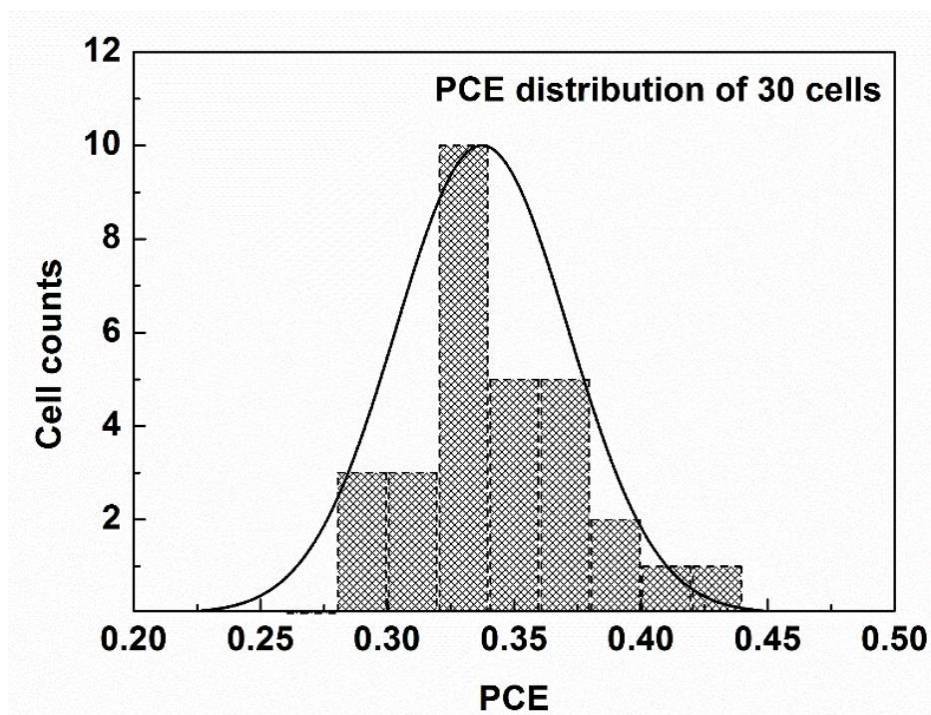


Fig.12 Distribution of a batch of 30 solar cell fabricated with CNBI.

One deficit of the CNBI solar cell is the low J_{sc} . By measuring the IPCE performance of the CNBI solar cell, we found that the quantum efficiency reached about 20% in the range

from 300 nm to 500 nm. Comparing to the UV-vis absorption spectrum, the IPCE at 500 - 600 nm is low. The low integrated current suggested that in this range, the CNBI cannot effectively convert the exetons to the electrons, thus a significant portion of the incident solar energy is lost. This can be considered as one the important reasons that we obtain low J_{sc} from the as-fabricated solar cell devices. We believe by proper surface engineering and passivation, the J-V performance of the CNBI devices can be greatly enhanced.

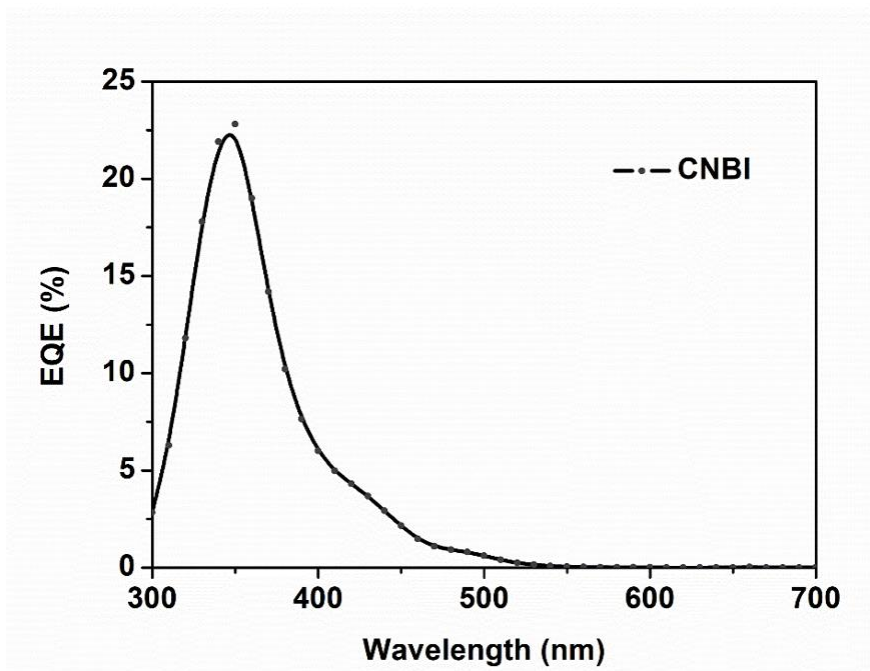


Fig. 13 The IPCE curve of the CNBI solar cell.

Another Issue we concerned is that the stability of the as-fabricated devices. To test the stability of the devices, we fabricated a solar cell device and stored it in ambient air for 14 days. The performances of this cell are presented in the Fig.14. We can see that The V_{oc} remains almost the same, showing that there were no extra recombination centres generated. This also agrees with our conclusion that our material is stable in the ambient air. The PCE of the cells show slightly decrease after storage, mainly due to the decrease of the J_{sc} . The lowering of the J_{sc} represents the damage of the HTM layer and the gold electrode. These performances showed that the CNBI solar cells have good stability against ambient conditions.

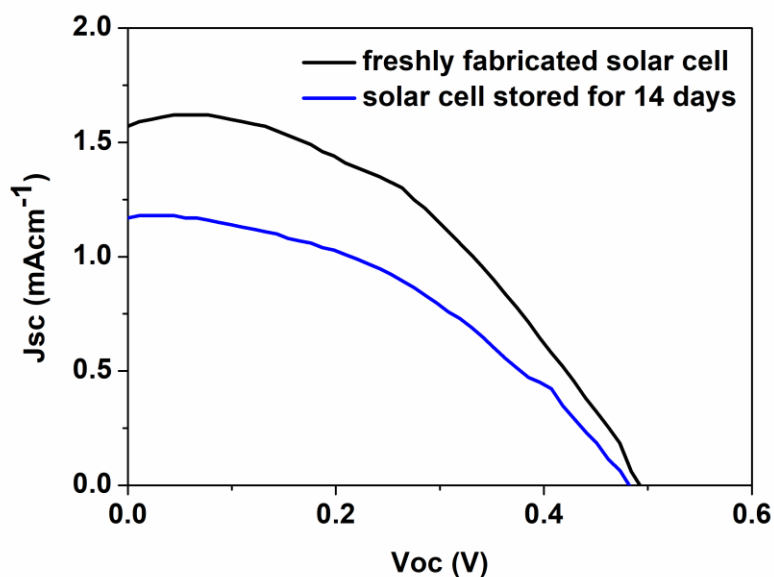


Fig.14 I-V curve comparison of the same cell when it was freshly fabricated (black) and after it was stored for 14 days (blue).

In order to confirm the device structure, we have also studied the band positions of the CNBI and the employed ETL/HTL materials. By testing the VBM position and calculated with the obtained bandgap, as shown in Fig. 15 (a) and (b), we can sketch the band positions of each layer. The CBM of the CNBI is near to that of the ETL, which provides only a weak potential for the electron injection. The VBM of the CNBI is also closer to that of the HTM comparing to the lead perovskites, which is not beneficial for the hole collection. Since CNBI has a lower hole mobility, the weakened hole collecting ability can be amplified in this scenario and is more significant. In combination, these two factors lead to another major reason for a low JSC. Introducing a more effective hole collector is a must should we want to reduce the recombination. In our case, the Spiro-OMeTAD is obviously not a smart choice. If we can select a superior hole transport material that can introduce stronger hole collecting ability, the performance of the device will definitely be enhanced.

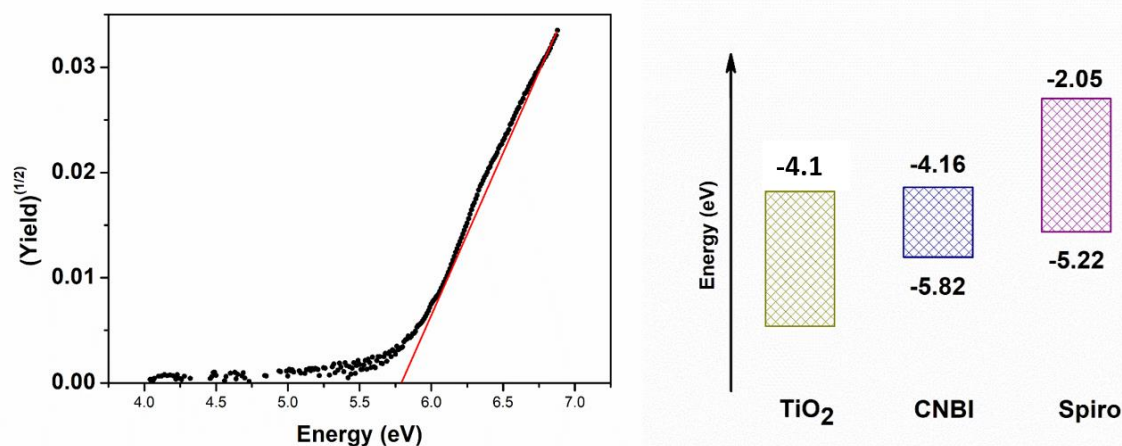


Fig.15 (a) The VBM position test. (b) The band position of the absorber (CNBI), the ETL (TiO_2) and the HTL (Spiro-OMeTAD).

4.3 Conclusions

To sum up, through a facile hydrothermal process, we have successfully synthesized a novel high stability double perovskite CNBI that can be applied as the light absorber. By measuring the UV-vis absorption, we determined that the CNBI has a bandgap of 1.66 eV, and it possesses a wide absorption range. CNBI displayed outstanding stability showing negligible decomposition after a 5-month storage under >70 humidity. The unique properties of this material meet the criteria of the photovoltaic application.

The CNBI double perovskite solar cell exhibited champion PCE of 0.42%. This result is comparable to other lead-free perovskite solar cell works. The devices stayed in ambient condition displayed a very small decrease in the photovoltaic performances, showing the device stability is good. The PCE distribution of the cells is narrow, suggesting that the devices displayed good reproducibility. Although the average PCE of CNBI solar cells so far is low due to the low JSC, we have revealed the main reason of the low JSC, and suggested possible enhancement directions. Future research will focus on improving the quality of the CNBI films with additives or surface passivation skills to fulfil the requirement as a photovoltaic device.

References

- [1]. Zhou H. Chen Q. Li G. Luo S. Song T. Duan H. et al. Interface engineering of highly efficient perovskite solar cells. *Science*. 2014 Aug 01;345(6196):542-546.
- [2]. Leng M. Yang Y. Zeng K. Chen Z. Tan Z. Li S. et al. All-Inorganic Bismuth-Based Perovskite Quantum Dots with Bright Blue Photoluminescence and Excellent Stability. *Adv Funct Mater*. 2017 Nov 27;28(1):1704446.
- [3]. Wu C. Zhang Q. Liu Y. Luo W. Guo X. Huang Z. et al. The Dawn of Lead-Free Perovskite Solar Cell: Highly Stable Double Perovskite Cs₂AgBiBr₆ Film. *Adv Sci*. 2017 Dec 18;5(3):1700759.
- [4]. Xiao Z. Meng M. Wang J. Yan Y. Thermodynamic Stability and Defect Chemistry of Bismuth-Based Lead-Free Double Perovskites. *ChemSusChem*. 2016 Sep 22;9(18):2628 – 2633.
- [5]. Volonakis G. Filip M. Haghighirad A. Sakai N. Wenger B. Snaith H. et al. Lead-Free Halide Double Perovskites via Heterovalent Substitution of Noble Metals. *J Phys Chem Lett*. 2016 Mar 16;7(7):1254-1259.
- [6]. Wei F. Deng Z. Sun S. Zhang F. Evans D. Kieslich G. et al. Synthesis and Properties of a Lead-Free Hybrid Double Perovskite: (CH₃NH₃)₂AgBiBr₆. *Chem Mater*. 2017, Jan 06;29(3):1089–1094.
- [7]. Filip M. Hillman S. Haghighirad A. Snaith H. Giustino F. Band Gaps of the Lead-Free Halide Double Perovskites Cs₂BiAgCl₆ and Cs₂BiAgBr₆ from Theory and Experiment. *J Phys Chem Lett*. 2016 Jun 20;7(13):2579–2585.
- [8]. Slavney A. Hu T. Lindenberg A. Karunadasa H. A Bismuth-Halide Double Perovskite with Long Carrier Recombination Lifetime for Photovoltaic Applications. *J Am Chem Soc*. 2016 Feb 07;138(7):2138–2141.
- [9]. McClure E. Ball M. Windl W. Woodward P. et al. Cs₂AgBiX₆ (X = Br, Cl): New Visible Light Absorbing, Lead-Free Halide Perovskite Semiconductors. *Chem Mater*. 2016 Feb. 10;28(5):1348–1354.
- [10]. Cheng P. Wu T. Li Y. Jiang L. Deng W. Han K. et al. Combining theory and experiment in the design of a lead-free ((CH₃NH₃)₂AgBiI₆) double perovskite. *New J Chem*. 2017 Aug 08;41:9598-9601.
- [11]. Volonakis G. Haghighirad A. Milot R. Sio W. Filip M. Wenger B. et al. Cs₂InAgCl₆: A New Lead-Free Halide Double Perovskite with Direct Band Gap. *J Phys Chem Lett*. 2017 Jan 30;8(4):772-778.
- [12]. Wei F. Deng Z. Sun S. Xie F. Kieslich G. Evans D. et al. The synthesis, structure and electronic properties of a lead-free hybrid inorganic–organic double perovskite (MA)₂KBiCl₆ (MA = methylammonium). *Mater Horiz*. 2016 Apr 15;3: 328-332.
- [13]. Li C, Lu X, Ding W, et al. Formability of ABX₃ (X = F, Cl, Br, I) halide perovskites. *Acta Crystallogr B*. 2008, 64, 702-707.

- [14]. Shannon R. Revised effective ionic radii and systematic studies of interatomic distances in halides and chalcogenides. *Acta Cryst.* 1976; A32:751-767.
- [15]. Lyu M. Yun J. Cai M. Jiao Y. Bernhardt P. Zhang M. et al. *Nano Research.* 2016 Jan 09;9(3):692–702.
- [16]. Ng C. Lim H. Hayase S. Zainal Z. Shafie S. Huang N. Effects of Temperature on Electrochemical Properties of Bismuth Oxide/Manganese Oxide Pseudocapacitor. *Ind Eng Chem Res.* 2018 Jan 23;57(6):2146-2154.
- [17]. Leguy A. Azarhoosh P. Alonso M. Campoy-Quiles M. Weber O. Yao J. et al, Experimental and theoretical optical properties of methylammonium lead halide perovskites. *Nanoscale.* 2016 Oct 05;8:6317-6327.
- [18]. Shockley M. Queisser H. Detailed Balance Limit of Efficiency of p-n Junction Solar Cells. *J Appl Phys.* 1961;32:510-519.

Chapter 5. Preparation and optimization of the micro single crystals of the $\text{Cs}_2\text{NaBiI}_6$ (CNBI) double perovskite

5.1 Introduction

Lead-based perovskite solar cells showed surprising development during the last ten years, reaching a high PCE of 23.3% [1]. As the outstanding properties were studied, disadvantage of instability and toxicity were also revealed [2-3]. So far, the majority of perovskite solar cells are based on polycrystalline films. Polycrystalline films generally suffer from higher trap density and higher grain boundaries [4]. Obviously, these traps and grain boundaries attributed to a great portion of the instability of the perovskite solar cells that hindered the commercial scale application of the perovskite solar cells.

On the other hand, single crystal (SC) demonstrated many superior advantages compared to the polycrystalline films. Attributing to their higher crystallinity, fewer defects, absence of grain boundaries and superior stability [5-8], single crystals are potential for fabricating high performance solar cells. This is proved with silicon solar cells, where SC silicon solar cell yields over 26% PCE and polycrystalline silicon solar cell yields 22% [9]. If we can fabricate perovskite solar cells with single crystal bulk or wafer, then the breakthrough of the PCE can be expected.

In order to obtain well-defined perovskite SCs, a variety of solution-based approaches were developed, including the hot solution cooling growth [10], the anti-solvent vapor-assisted crystallization [11], the top-seeded growth [12], the inverse temperature crystallization [13], and the solvent acidolysis crystallization [14].

Although hybrid lead perovskite SCs and inorganic lead perovskite SCs both reached over 10 mm in scale, only a few reported successful device fabrication with these materials. On important reason is that the mechanical strength of the perovskite SCs are low and it is hard to obtain wafer or film from bulk macro SC. On the other hand, micro SCs suggested successful application to the solar cell devices [15-16]. The same methodology can be introduced to the lead-free perovskite material preparation, and it may be able to solve the problem that the lead-free perovskites can only yield low quality polycrystalline film.

5.2 Experimental section

5.2.1 Crystal growth process of the micro single crystals

The method for growing micro single crystal of the CNBI double perovskite is very similar to that of the synthesis of the CNBI powder sample. To be specific, 9M hydroiodic acid (47 wt% in water, stored in refrigerator, Sigma-Aldrich) was diluted to 6M. Then dissolve 2 mole caesium iodide (99.999% trace metals basis, Sigma-Aldrich), 1 mole sodium iodide (99.999% trace metals basis, Sigma-Aldrich) and 1 mole bismuth iodide (99.999% trace metals basis, Sigma-Aldrich) in 12mL of this 6M hydroiodic acid to form an orange dispersion. After 10 min of magnetic stirring, remove the magnetic stirrer and transfer the solution to a Teflon-lined autoclave for further processing.

To carry out the hydrothermal process, the autoclave was loaded to the stainless steel container and put in an oven to heat at 120°C for 12 hrs, and then slowly cooled to room temperature in 20 hrs to allow the fully growth of the micro SCs. A sand-like, dark cerise crystal of the CNBI perovskite was obtained. This sample was washed multiple times with D.I water and centrifuged until the supernatant is clear and colourless, and then dried in a vacuum chamber to obtain the final product.

In order to investigate the parameters of the micro single crystal growth, multiple experiment sets were carried out with respect to the HI (aq.) concentration, the synthesis temperature, the molar ratio of the reagents, etc. The parameters studied are listed in the Table.1 below.

Table.1 The parameter studied in order to optimize the micro single crystal growth.

Na ⁺ ratio Compared to Bi ³⁺	HI (aq.) Concentration (M)	Reaction temperature (°C)
0	1	110
1	3	120
2	6	130
3	9	

5.2.2 Characterization methods

In order to elucidate the physical properties of the CNBI micro single crystals, XRD (Rigaku XRD-DSC-XII) test was carried out in the range of 5° to 80° ($5^{\circ}/\text{min}$) to determine the components of the product. We also took FE-SEM (Hitachi F-5200) images to observe the growth situation of the micro single crystals.

In order to evaluate the optical properties of the CNBI micro single crystals, the UV-vis absorption spectra (Shimadzu UV-2550) were measured in order to observe the absorption property of the sample and to calculate its bandgap.

5.3 Results and discussion

5.3.1 The optimization of the CNBI micro single crystal growth method.

As we have discussed in previous chapter, the hydroiodic acid is an important parameter affecting the composition of the CNBI. To further elucidate the function of how the hydroiodic acid affects the system, we carried out crystal growth experiments under different hydroiodic acid concentration.

XRD test was performed to determine the crystal structure of CNBI micro SCs synthesized using different acid concentrations (1, 3, 6 and 9 M) as shown in Fig.1. Overall, the XRD patterns of all the synthesized CNBI SCs match well and are reproducible regardless of the acid concentrations employed. It shows that the intensities of the CBI peaks gradually decreased in conjunction with the increase of acid concentration, showing that the decomposition became less significant and the formation of CNBI is more dominating with respect to the increase of the acid concentration. We can say that increasing acid concentration would suppress the decomposition and promote the formation of our target CNBI compound. It is also noticed that the peak at ca. 26° decreased significantly when the acid concentration increased from 1 M to 6 M, then slightly increased when the concentration increased to 9 M. It is quite clear that this peak represents the 2D plate morphology of CBI. The change of this peak showed that at lower acid concentration the by-product CBI is of high ratio, and with the increase of the acid concentration the decomposition of CNBI was suppressed. However at higher concentration the decomposition would again slightly be promoted, most possibly due to the dissolving of the CNBI in residual HI acid after cooled down.

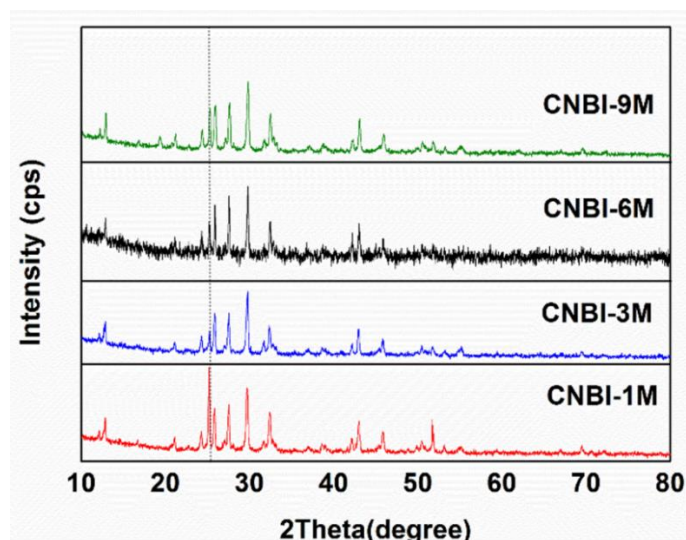


Fig.1 XRD patterns of the CNBI micro SCs prepared at different hydroiodic acid concentrations. Corresponding acid concentrations were marked out. The dash line marks the peak at ca. 26° representing the 2D plate structure.

We have also carried out UV-vis absorption spectroscopy of the micro SCs grown under different hydroiodic acid concentrations to observe their light absorption abilities. Fig.2 shows the optical absorption measurement of the synthesized CNBI at different HI concentrations. It reveals that the CNBI sample obtained using 6 M HI during the synthesis possesses the best light absorbing ability. This could be due to the usage of 6M HI optimizes and induces a conducive condition for the growing of highly crystalline CNBI crystal structure. The CNBI powder exhibited excellent light absorption ranging from 300 nm to 600 nm with an absorption edge at 650 nm. The wide light absorption range of the CNBI material is an important property and is a core criterion for photovoltaic applications. Similar to its powder sample, it is obvious that the CNBI micro SCs also possess stronger absorption below 350 nm where the lead halide perovskite usually started to show decrease in the absorption. This suggested that CNBI micro SCs maintained the superior ability to help harvesting extra energy in the ultraviolet region to enhance the photo current conversion.

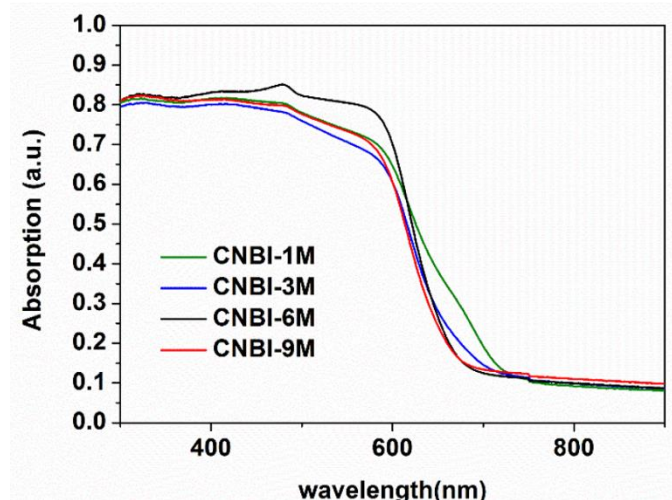


Fig.2 UV-vis absorption curves for the CNBI micro SCs prepared at different hydroiodic acid concentrations. The corresponding acid concentrations are marked out.

To confirm the morphology change of the CNBI micro SCs, we took SEM images of the CNBI micro SCs prepared from different acid concentrations. Evidently, a highly crystallized CNBI micro SC synthesized at high acid concentration condition was observed from Fig.3, indicating that a highly acidic reaction process would favour and promote the crystallization of the CNBI double perovskite, which is in agreement with the optical absorption spectra. The morphology of the CNBI synthesized at 1M acid concentration in Fig.3 (a) presented irregular bulks consisting nanoplatelets. On the contrary, the CNBI grew larger with smoother and cleaner surface coverage as shown in Fig.1(b) when the acid concentration increased to 3 M. As the acid concentration increased to 6 M, we can see well-grown shuttle-like CNBI micro SCs. However, further increasing the HI concentration does not continually improve the growing of the crystal. In contrast, agglomeration of the shuttle-like particles was observed on the surface of CNBI at high HI concentration of 9 M. The trend of the crystal growth agreed with the XRD pattern and the UV-vis absorption spectra. It is obvious that if we want to optimize the yield of the shuttle-like micro SCs of CNBI, we should definitely choose 6 M hydroiodic acid as the hydrothermal solution.

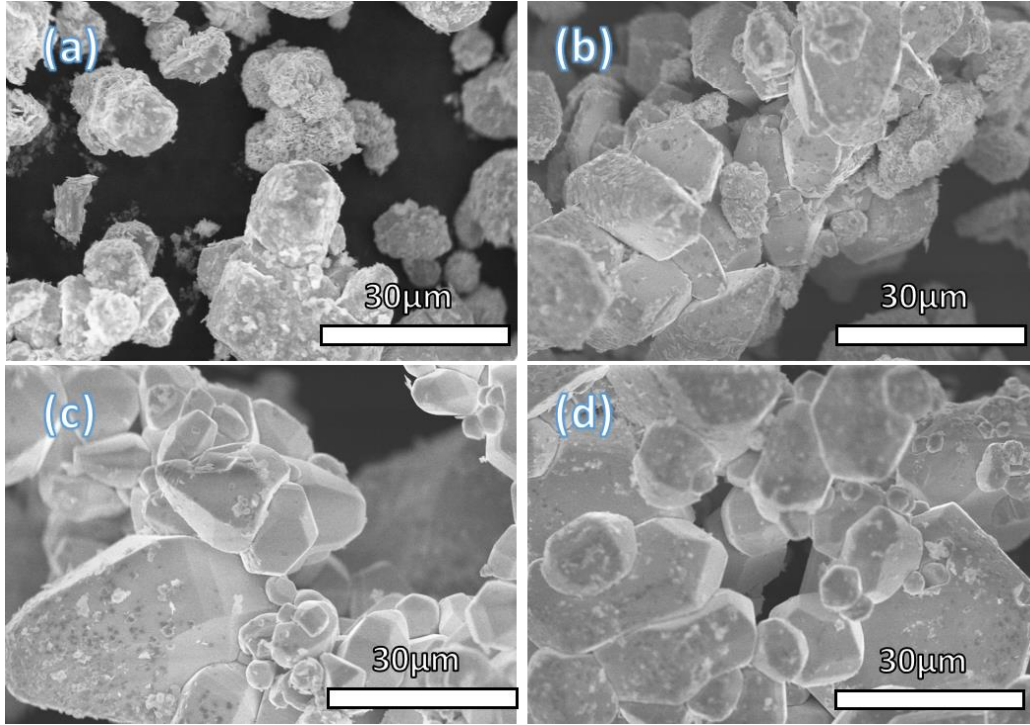


Fig.3 SEM Images of the CNBI micro SCs synthesized under different acid concentration: (a) 1M, (b) 3 M, (c) 6 M, and (d) 9 M.

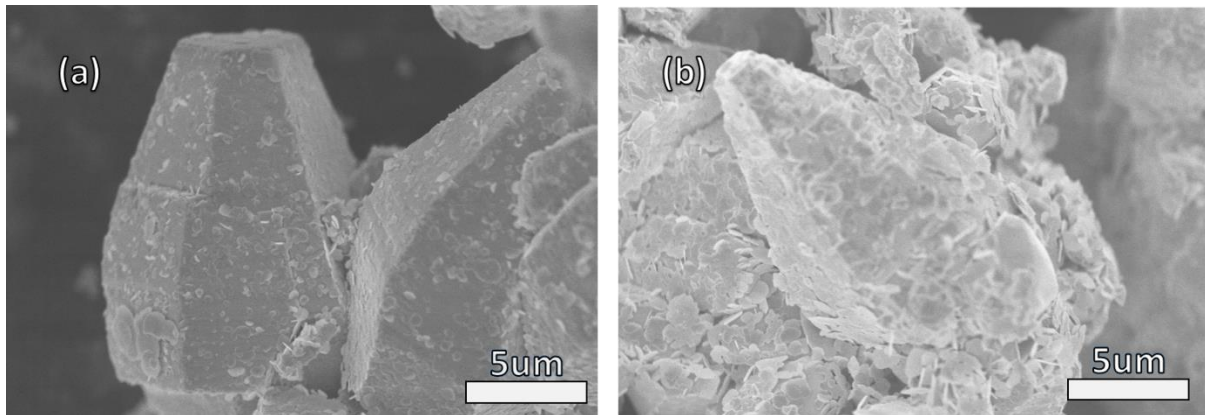


Fig. 4 Micro SCs grown with increased Na ratio: (a) 2 M and (b) 3M. Multiple small platelets can be observed from the images.

Another parameter we inspected is the Na^+ cation as a variable. By adjusting the input of NaI we fabricated CNBI micro SCs at the Na^+ concentration of 1 M, 2 M and 3 M. We can see from the images in Fig.4 that with increased sodium amount, many small platelets were attached to the

surface of the CNBI micro SCs, making the surface of the crystals significantly rougher. Judging by the morphology of these irregular platelets, these should be the 2D crystal phase or the $\text{Cs}_3\text{Bi}_2\text{I}_9$ impurities. It is obvious that with the increase of the sodium amount, the crystallinity of the CNBI micro SCs were reduced. The optimized Na^+ ratio should be no more than 1M.

The synthesis temperature is also a parameter that we studied. By synthesizing CNBI under different hydrothermal temperature, we have prepared a series of sample SCs. The sample synthesized under 120 °C (namely 110 °C) showed strong main phase of $\text{Cs}_3\text{Bi}_2\text{I}_9$, while samples synthesized above 120 °C (namely 130 °C) showed similar XRD pattern to that of the CNBI, with no significant change at the peak distribution and the peak intensity, as shown in Fig. 5. It is obvious that the 120 °C is a temperature threshold that allows the CNBI phase to form. It is reasonable that the synthesis temperature would not significantly affect the micro SC growth, since the SC growth mechanism revealed that the development of the micro SCs are during the slow cooling process.

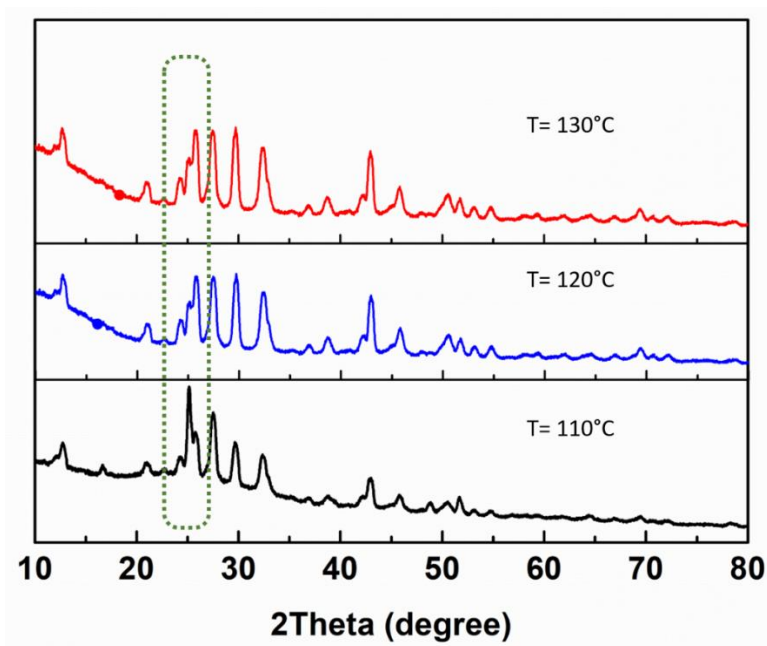


Fig. 5 Micro SCs grown with different hydrothermal process temperature, $T = 110^\circ\text{C}$, 120°C and 130°C . The peak at $\sim 25^\circ$ displayed distinct difference, showing significantly increased CBI phase when $T < 120^\circ\text{C}$.

5.3.2 The growth mechanism of the CNBI micro single crystals

In order to have an overall concept of the crystal growth process of the CNBI micro single crystals, we observed and elucidated the crystal growth mechanism of the CNBI micro single crystals by inspecting the SEM images at different crystal growth times. As demonstrated in Fig.6, SEM images showed the CNBI micro single crystals synthesized under 6M hydroiodic acid condition. It is observable that the fully-grown CNBI micro single crystal can reach the size of several tens of micrometres. The fully-grown large crystals are encouraged by both the acidic solution environment and the high pressure enclosed hydrothermal process.

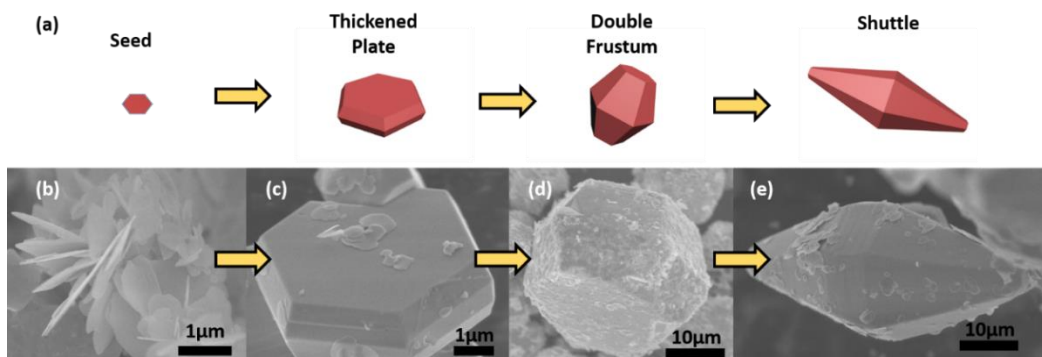


Fig. 6 Scheme of the crystal growth mechanism and corresponding SEM images of the as-prepared CNBI. Here (a) showed the sequentially growth steps of the CNBI crystal, while (b), (c), (d) and (e) are the SEM images of the crystals at different growth steps.

For a colloid solution, it is quite natural for the solution to assume a super saturation condition. If without any disturbance, the super saturation solution can easily maintain its steady state equilibrium. As temperature increases, the magnitude of the super saturation will become higher. If this solution is disturbed under such condition, it will loss the equilibrium and the solute will precipitate. The solution then will consequently dissolve the colloids, “releasing” reagent ions, and continually supply the super-saturation condition. Fuelled by this mechanism, the solute will continually crystallize until the super-saturation is “depleted” and the solution reaches a new equilibrium state [17].

In our case, the increase of the temperature during the hydrothermal process not only disturbed the equilibrium state of the solution, but also caused more colloids to dissolve, and lead to a super-saturation condition. When the super-saturation condition was first reached, the CNBI

crystal seeds would form and started to grow along the (001) plane forming hexagonal platelets, as shown in Fig.6 (a). As the synthesis process continues, as described above, the imbalanced equilibrium will continue to promote the crystallization process. At this stage, the plate would continually grow along the plane while thickening on both sides, generating (Fig.6 (c)) a thickened plate. The size of the plate would increase dramatically. With longer synthesis time, the crystal growth along the (001) plane will be hindered, most likely caused by the adsorption of excessed I- and H⁺ ions on the surface of the crystal, and the crystal will start to preferentially grow in both directions perpendicular to the (001) plane, thus forming a double frustum as shown in Fig.6 (d). The large CNBI crystal continued to grow during this continual super-saturation, subsequently initiating the crystallization process, and eventually formed the fully-grown crystal with the shuttle-like morphology, as shown in Fig.6 (e).

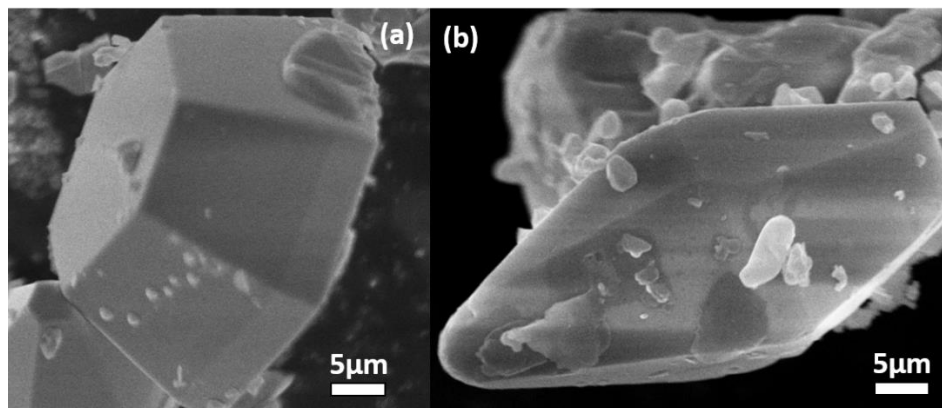


Fig.7 SEM images of the crystals grown in (a) asymmetric double frustum and (b) asymmetric shuttle morphology.

Another interesting finding is that the shuttle-like crystal will not necessarily grow symmetrically with respect to its centre plane. As shown in Fig.7, we can see asymmetric crystals in different stages of the growth process. We believe that the insufficient growing space resulted in the asymmetric growth.

5.4 Conclusions

In summary, we prepared 3D shuttle-like CNBI micro SCs by simple one-step hydrothermal growth method. By investigating multiple reaction parameters including hydroiodic acid concentration, Na^+ cation ratio and hydrothermal synthesizing temperature, we have decided the optimized preparation condition of the CNBI micro SCs. The hydroiodic acid concentration was proved the key factor for preparing the CNBI micro SCs, while the amount of the Na^+ cation can contribute to the crystallization velocity of the CNBI micro SCs. By observing the growth process, we elucidated the growth mechanism of the CNBI micro SC, and the CNBI prepared with the optimized conditions consists high ratio of well-defined shuttle-like micro SCs. Further work on the topic includes the separation of the micro SCs and the application of the micro SCs to the solar cell devices, such as micro SC array solar cells.

References

- [1]. Yang Y, You J, Lei M, inventors. The Regents of the University of California (Oakland, CA, US), assignee. Efficient and Stable Perovskite Solar Cells with All Solution Processed Metal Oxide Transporting Layers. United States Patent 0033983. 2018-02-01.
- [2]. Berhe T. Su W. Chen C. Pan C. Cheng J. Chen H. et al. Organometal Halide Perovskite Solar Cells: Degradation and Stability. *Energy Environ Sci*. 2015 Oct 20;9:323-356.
- [3]. Feng J. Xiao B. Effective Masses and Electronic and Optical Properties of Nontoxic MASnX_3 (X = Cl, Br, and I) Perovskite Structures as Solar Cell Absorber: A Theoretical Study Using HSE06. *J Phys Chem C*. 2014 Aug 6;118(34):19655-19660.
- [4]. Dong Q. Fang Y. Shao Y. Mulligan P. Qiu J. Cao L. Huang J. Electron-Hole Diffusion Lengths $> 175 \mu\text{m}$ in Solution-Grown $\text{CH}_3\text{NH}_3\text{PbI}_3$ Single Crystals. *Science*. 2015 Feb 27;347(6225):967-970.
- [5]. Lian Z. Yan Q. Lv Q. Wang Y. Liu L. Zhang L. et al. High-Performance Planar-Type Photodetector on (100) Facet of MAPbI_3 Single Crystal. *Sci Rep*. 2015 Nov 13;5:16563.
- [6]. Peng W. Wang L. Murali B. Ho KT. Bera A. Cho N. et al. Solution-Grown Monocrystalline Hybrid Perovskite Films for Hole-Transporter-Free Solar Cells. *Adv Mater*. 2016 May 04;28(17):3383-3390.
- [7]. Rao HS. Li WG. Chen BX. Kuang DB. Su CY. In Situ Growth of 120 cm^2 $\text{CH}_3\text{NH}_3\text{PbBr}_3$ Perovskite Crystal Film on FTO Glass for Narrowband-Photodetectors. *Adv Mater*. 2017 Apr 25;29(16):1602639.
- [8]. Rao HS. Chen BX. Wang XD. Kuang DB. Su CY. A Micron-Scale Laminar MAPbBr_3 Single Crystal for an Efficient and Stable Perovskite Solar Cell. *Chem Commun*. 2017 May 07;53(37): 5163-5166.
- [9]. Green M. Hishikawa Y. Dunlop E. Levi D. Hohl-Ebinger J. Ho-Baillie A. Solar Cell Efficiency Tables (version 52). *Prog Photovolt Res Appl*. 2018;26:427–436.
- [10]. Mitzi DB. Synthesis, Structure, and Properties of Organic-Inorganic Perovskites and Related Materials. *Prog Inorg Chem*. 2007 Mar 09;48:1-121.
- [11]. Shi D. Adinolfi V. Comin R. Yuan M. Alarousu E. Buin A. et al. Low trap-state density and long carrier diffusion in organolead trihalide perovskite single crystals. *Science*. 2015 Jan 30;347(6221):519-522.
- [12]. Saidaminov MI. Abdelhady AL. Murali B. Alarousu E. Burlakov VM. Peng W. et al. High-Quality Bulk Hybrid Perovskite Single Crystals within Minutes by Inverse Temperature Crystallization. *Nat Commun*. 2015 Jul 06;6:7586.
- [13]. Zhang T. Yang M. Benson EE. Li Z. van de Lagemaat J. Luther JM. et al. A Facile Solvothermal Growth of Single Crystal Mixed Halide Perovskite $\text{CH}_3\text{NH}_3\text{Pb}(\text{Br}_{1-x}\text{Cl}_x)_3$. *Chem Commun*. 2015 May 07;51(37):7820-7823.

- [14]. Kulbak M. Cahen D. Hodes G. How Important Is the Organic Part of Lead Halide Perovskite Photovoltaic Cells? Efficient CsPbBr₃ Cells. *J Phys Chem Lett*. 2015 Jun 10;6(13):2452-2456.
- [15]. Wu J. Ye F. Yang W. Xu Z. Luo D. Su R. et al. Perovskite Single-Crystal Microarrays for Efficient Photovoltaic Devices. *Chem Mater*. 2018 Jul 11;30(14):4590-4596.
- [16]. Chen Z. Dong Q. Liu Y. Bao C. Fnag Y. Lin Y. et al. Thin Single Crystal Perovskite Solar Cells to Harvest below-Bandgap Light Absorption. *Nat Commun*. 2017 Dec 01;8:1890.
- [17]. Nayak P. Moore D. Wenger B. Nayak S. Haghighirad A. Fineberg A. et al. Mechanism for Rapid Growth of Organic–Inorganic Halide Perovskite Crystals. *Nat Comm*. 2016 Nov 10;7:13303.

6. General conclusions and future prospects

In this thesis, we focused on the development of new lead-free bismuth-based light absorbing materials for perovskite solar cells. We prepared a mixed chalcogen-halogen perovskite and a double perovskite with low bandgap and excellent stability by solid-state synthesis and hydrothermal synthesis method, respectively. With many characterization techniques, we studied the physical and optical properties of these new materials. Furthermore, we employed these new lead-free perovskites as the light absorber for the perovskite solar cells, and evaluated their performances. In addition, based on our designed new material, we have also explored the micro single crystal preparation techniques.

1. In Chapter 3, we successfully synthesized a mixed chalcogen-halogen lead-free perovskite MABiI_2S with two-step solid-state reaction. With multiple testing techniques, we confirmed its composition. By measuring the UV-Vis absorption spectra, we determined that the MABiI_2S perovskite has a bandgap of 1.52 eV, and it possesses a wide absorption range that extend to over 1000 nm. The unique properties of this material meet the criteria of the photovoltaic application. By employing an in-situ growth technique, we solved the difficulty that the spin coating technique cannot produce viable MABiI_2S perovskite film on the TiO_2 substrates. The composition of the in-situ growth film was verified with layer-by-layer XRD pattern analysis. Unfortunately, the device fabricated with the in-situ growth film showed poor I-V performance. However, the material displayed high defect tolerance ability. In addition, several enhancement routes were inspected and the device performance were greatly increased.

2. In Chapter 4, we successfully synthesized a novel high stability double perovskite CNBI through a facile hydrothermal process. By measuring the UV-Vis absorption, we determined that the CNBI has a bandgap of 1.66 eV, and it possesses a wide absorption range. CNBI displayed outstanding stability showing negligible decomposition after a 5-month storage under >70 humidity. The unique properties of this material meet the criteria of the photovoltaic application. The CNBI double perovskite solar cell exhibited champion PCE of 0.42%. This result is comparable to other lead-free perovskite solar cell works. The devices stayed in ambient condition displayed a very small decrease in the photovoltaic performances, showing the device stability is good. The PCE distribution of the cells is narrow, suggesting that the devices displayed good

reproducibility. Although the average PCE of CNBI solar cells so far is low due to the low JSC, we have revealed the main reason of the low JSC, and suggested possible enhancement directions.

3. In Chapter 5, we prepared 3D shuttle-like CNBI micro SCs by simple one-step hydrothermal growth method. By investigating multiple reaction parameters including hydroiodic acid concentration, Na^+ cation ratio and hydrothermal synthesizing temperature, we have decided the optimized preparation condition of the CNBI micro SCs. The hydroiodic acid concentration was proved the key factor for preparing the CNBI micro SCs, while the amount of the Na^+ cation can contribute to the crystallization velocity of the CNBI micro SCs. By observing the growth process, we elucidated the growth mechanism of the CNBI micro SC, and the CNBI prepared with the optimized conditions consists high ratio of well-defined shuttle-like micro SCs. Further work on the topic includes the separation of the micro SCs and the application of the micro SCs to the solar cell devices, such as micro SC array solar cells.

To date, the lead-free perovskites still suffer from several major issues that result in relatively low PCEs, such as larger bandgaps, more intrinsic defects, and weaker carrier mobility compared to that of the lead-based perovskites.

The future prospects of the lead-free bismuth-based perovskite materials might include following aspects: modifying the material composition to obtain small and direct bandgap, refining the film surface to reduce the intrinsic defects, and the exploration towards viable single crystal solar cell/solar cell array devices.

Achievements

Publications

1. **Zhang C**, Gao L, Teo S, Guo Z, Xu Z, Zhao S, Ma T. Designation of a Novel and Highly Stable Lead-Free $\text{Cs}_2\text{NaBiI}_6$ Double Perovskite for Photovoltaic Application. *Sustainable Energy Fuels*. 2, 2419–2428, 2018.
2. **Zhang C**, Gao L, Hayase S, Ma T. Current Advancements in Material Research and Techniques Focusing on Lead-free Perovskite Solar Cells. *Chemistry Letters*. 46(9), 1276-1284. 2017.
3. **Zhang C**, Teo S, Guo Z, Gao L, Kamata Y, Xu Z, Ma T. Development of a Mixed Halide-chalcogenide Bismuth-based Perovskite MABiI_2S with Small Bandgap and Wide Absorption Range. *Chemistry Letters*. DOI: 10.1246/cl.180919.
4. **Zhang C**, Teo S, Gao L, Kamata Y, Ma T. Development of a novel mixed sulfide-iodide lead-free bismuth perovskite, *Proc. SPIE 10724, Physical Chemistry of Semiconductor Materials and Interfaces XVII*. 107240A. 2018.
5. Guo Z, Gao L, **Zhang C**, Xu Z, Ma T. Low-Temperature Processed Non- TiO_2 Electron Selective Layers for Perovskite Solar Cells. *J.Mater.Chem.A*. 6, 4572-4589. 2018.
6. Lan C, Luo J, Zhao S, **Zhang C**, Liu W, Hayase S, Ma T. Effect of lead-free $(\text{CH}_3\text{NH}_3)_3\text{BiI}_9$ perovskite addition on spectrum absorption and enhanced photovoltaic performance of bismuth triiodide solar cells. *J. Alloy. Comm.* 701, 834-840. 2017.
7. Lan C, Zhao S, **Zhang C**, Liu W, Hayase S, Ma T. Concentration gradient controlled growth of large-grain $\text{CH}_3\text{NH}_3\text{PbI}_3$ films and enhanced photovoltaic performance of solar cells in ambient conditions. *CrystEngComm*. 18, 9243-9251. 2016.

Conferences

1. **Chu Zhang**, Zhanglin Guo, Shuai Zhao, Liguao Gao, Tingli Ma. “Design and Synthesis of a New All Inorganic Double Perovskite $\text{Cs}_2\text{NaBiI}_6$ with 3D Shuttle-like Structure”, Japan-China Workshop on “Nanomaterials and their applications in new energy devices”, Fukuoka, Japan, October 2017.

2. **Chu Zhang**, Zhanglin Guo, Shuai Zhao, Liguao Gao, Tingli Ma. “Design and Synthesis of a New All Inorganic Double Perovskite $\text{Cs}_2\text{NaBiI}_6$ with 3D Shuttle-like Structure”, Asia-Pacific Hybrid and Organic Photovoltaics Conference (AP-HOPV 18). Fukuoka Japan, Jan. 28th - 30th. 2018.
3. **Chu Zhang**, Liguao Gao, Tingli Ma. “Pb-free perovskites and their application for solar cells” SPIE Organic Photonics + Electronics, San Diego, USA, Aug 11st – 15th, 2018.
4. Huan Li, **Chu Zhang**, Zhanglin Guo, Tingli Ma, “In-situ growth of feather-like MnO_2 on carbon paper for high performance sodium-ion battery”, 5th International Conference on Nanomechanics and Nanocomposites (ICNN5), Fukuoka, Japan, Aug. 22nd – 25th, 2018.
5. **Chu Zhang**, Siowhwa Teo, Zhanglin Guo, Zhenhua Xu, Tingli Ma. “Designation of a Novel and Highly Stable Lead-Free $\text{Cs}_2\text{NaBiI}_6$ Double Perovskite for Photovoltaic Application” 35th European Photovoltaic Solar Energy (EU PVSEC), Sep 24th - 28th, 2018.

Acknowledgements

Firstly, I would like to express my deepest thanks to my supervisor, Professor Ma, for her instructive advice, constant encouragement and guidance. During my Ph.D. study, Professor Ma has always been able to lead me to the correct direction during my research process, and she always would be the driving force when I fell behind. Without her instruction and help, I will definitely not be able to finish my doctoral program.

I am also greatly indebted to Prof. Shuzi Hayase and Prof. Shyam S. Pandey, who have instructed and helped me a lot in the past three years.

Meanwhile, I would like to thank all the members in Ma lab, Hayase lab and Pandey lab, for they have provided valuable and timely assistant not only on the research but also in my daily life.

At last, I would express my thanks and love to my parents, who have supported my study in Japan without double. Their support has always been the best energy source when I fell in trouble and drawbacks.